2018

Development of a One-Way Coupled Diffraction/Trapped Air Model for Predicting Wave Loading on Bridge Superstructure Under Water Wave Attack

Christian Hillary Matemu
University of North Florida, christianhillary52@gmail.com

DEVELOPMENT OF A ONE-WAY COUPLED DIFFRACTION/TRAPPED AIR MODEL FOR PREDICTING WAVE LOADING ON BRIDGE SUPERSTRUCTURE UNDER WATER WAVE ATTACK

by

Christian Hillary Matemu

A Thesis submitted to the School of Engineering

in partial fulfillment of the requirements for the degree of

Master of Science in Civil Engineering

UNIVERSITY OF NORTH FLORIDA

COLLEGE OF COMPUTING, ENGINEERING, AND CONSTRUCTION

August 2018

The thesis "Development of a One-Way Coupled Diffraction/Trapped Air Model for Predicting Wave Loading on Bridge Superstructure under Water Wave Attack" submitted by Christian Hillary Matemu in partial fulfillment of the requirements for the degree of Master of Science in Civil Engineering has been

Approved by the thesis committee: Date:

_______________________________ ____________________

Raphael Crowley, Ph.D., P.E.
Thesis Advisor and Committee Chairperson

_______________________________ ____________________

Adel ElSafty, Ph.D., P.E.
Committee Member

_______________________________ ____________________

Don Resio, Ph.D.
Committee Member

Accepted for the School of Engineering:

_______________________________ ____________________

Murat Tiryakioglu, Ph.D. CQE
Director of the School of Engineering

Accepted for the College of Computing, Construction, and Engineering

_______________________________ ____________________

Mark A. Tumeo, Ph.D. J.D. P.E.
Dean of the College of Computing, Engineering, and Construction

Accepted for the University:

_______________________________ ____________________

John Kantner, Ph.D. RPA
Dean of the Graduate School

DEDICATION

I dedicate this thesis to my beloved parents Hillary and Rachel

ACKNOWLEDGMENTS

First and foremost, I wish to thank Almighty God for his endless blessings in my life. I am extremely grateful to my thesis advisor and committee chair, Dr. Raphael Crowley. Without his support, guidance, and patience, this thesis work wouldn't be achievable. He introduced me to the topic and I have benefited a lot from his past experience on it, not to mention his superior knowledge on water waves-structure interaction. A special thanks to my committee members, Dr. ElSafty and Dr. Resio who never hesitated to provide insight and guidance throughout this journey.

Secondly, I thank Taylor Engineering Research Institute (TERI), for the financial support which made possible for me to pursue and complete a Master's Degree at the University of North Florida. I'm gratefully for conducive learning environment you have provided me with, and I consider myself fortunate to be one of the coastal group. Special thanks to Ms. Holli Klein for her guidance since I came to the USA. She helped with all processes from registration until now I'm completing my master's degree. I am indebted to the UNF coastal lab members especially Patrick, Dorukhan, and Amanda for their endless supports both in research and social life.

Lastly, a special word of appreciation also goes to my family and friends who have loved, encouraged, and cheered me on along the path. I love you all.

TABLE OF CONTENTS

LIST OF TABLES

LIST OF FIGURES

ABSTRACT

In recent years, a number of researchers have applied various computational methods to study wind wave and tsunami forcing on bridge superstructure problems. Usually, these computational analyses rely upon application of computational fluid dynamic (CFD) codes. While CFD models may provide reasonable results, their disadvantage is that they tend to be computationally expensive. During this study, an alternative computational method was explored in which a previously-developed diffraction model was combined with a previously-developed trapped air model under worst-case wave loading conditions (i.e. when the water surface was at the same elevation as the bottom bridge chord elevation). The governing equations were solved using a finite difference algorithm in MATLAB for the case where the bridge was impacted by a single wave in two dimensions. Resultant inertial and drag water forces were computed by integrating water pressure contacting the bridge superstructure in the horizontal and vertical directions, while resultant trapped air forces (high-frequency oscillatory forces or sometimes called “slamming forces” in the literature) were computed by integrating air pressure along the bottom of the bridge deck in the vertical direction. The trapped air model was also used to compute the buoyancy force on the bridge due to trapped air. Results were compared with data from experiments that were conducted at the University of Florida in 2009. Results were in good agreement when a length-scale coefficient associated with the trapped air model was properly calibrated. The computational time associated with the model was only approximately one hour per bridge configuration, which would appear to be a significant improvement when compared with other computational technique

Chapter 1 INTRODUCTION

1.1. Background

On September 16, 2004, waves and surge from Hurricane Ivan damaged significant portions of the Interstate-10 Escambia Bay Bridge (Figure 1-1) near Pensacola, Florida. During this wave/surge event, many anchor bolts failed due to massive uplift forces created by surge and waves inundating the bridge superstructure. Forty-six eastbound spans and twelve westbound spans were pushed from their substructures, while sixty-six spans suffered misalignment. As a result of this failure, traffic was forced to negotiate a 130-mile detour around Escambia Bay for several months as the bridge was repaired. Repair cost was approximately $30.7 million (Talbot, 2005), while almost $243 million was spent to build a replacement bridge (Jin and Meng, 2011; Meng, 2008). During hurricane Katrina in 2005, 44 highway bridges were damaged – 7 in Mississippi, 33 in Louisiana, and 4 in Alabama. Repair cost associated with these failures was over $1 billion (Padgett et al., 2008). Four of these failures were caused by wave action and storm surge – the Biloxi Bay Bridge in Biloxi (Figure 1-2), MS; the Lake Pontchartrain Causeway Bridge just outside of New Orleans, LA; the Bay St. Louis Bridge in Bay St. Louis, MS; and the Mobile Bay onramp in Mobile, AL. Postmortem analysis of these bridge failures showed that failure mechanisms were similar to the mechanisms that caused the Escambia Bay Bridge collapse in that the waves caused vertical uplift and horizontal forces on the bridge superstructures that exceeded the tie downs' strengths Douglass et al. (2006).

Figure 1-1. I-10 Bridge Escambia Bay spans removed by Hurricane Ivan

Figure 1-2. Photograph of U.S. 90 Bridge over Biloxi Bay showing bridge deck damaged by Hurricane Katrina

Since 2005, the failure mechanisms associated with these bridge collapses have been studied extensively. Several of these studies involved conducting laboratory experiments to measure uplift and vertical forcing during wave action. Examples include McConnell et al. (2004), Douglass et al. (2006), Marin and Sheppard (2009), Marin (2010), Bradner (2009), and Bradner et al. (2011). During the Marin and Sheppard (2009) and Marin (2010) studies, results were used to calibrate coefficients associated with Morison-style (Morison et al., 1950) forcing equations that were adapted from previous work from Kaplan (1992), and Kaplan et al. (1995). However, Jin and Meng (2011) and Meng (2008) criticized the Morison-style approach for computing wave loading on bridges under wave attack because Morison-style analyses do not take fluid-structure interaction effects into account. In other words, because the bridge and the wave are of similar length scales, the bridge will affect the wave kinematics. In addition, as Cuomo et al. (2009) pointed out, during experiments, it is not possible to scale atmospheric pressure. Thus, scaling non-physics-based or quasi-physics-based experimental data would appear to be inaccurate.

Since 2010, a number of researchers have used computational fluid dynamic (CFD) models to study the wave loading on bridge superstructure problem. Examples include Azadbakht (2013), Azadbakht and Yim (2015), Azadbakht and Yim (2016), Bozorgnia et al. (2010), Bozorgnia (2012), Bozorgnia and Lee (2012), Seiffert et al. (2015), Seiffert et al. (2016), Xu and Cai (2014) and Crowley et al. (2018). Holistically, results from all studies (both experimental and computational) were similar in that wave forcing on bridges was shown to be a combination of a quasi-static load and a high-frequency oscillatory load. The quasi-static load is caused by a combination of drag forces, inertial forces, buoyancy forces, and an added mass component. Trapped air between the girders appears to play a role in buoyancy forcing as well because more

trapped air displaces more water. The high-frequency oscillatory load is caused by adiabatic compression of the trapped air and the bridge geometry (Cuomo et al., 2009).

During several of the aforementioned studies, results were used to calibrate non-dimensional parametric design equations. For example, results from Marin and Sheppard (2009) and Marin (2010) studies were used as a design guideline in AASHTO (2008). Results from Douglass et al. (2006) were used to develop Hydraulic Engineering Circular No. 25 (Douglass et al., 2014). Meng (2008) and Jin and Meng (2011) developed their own design guidelines. While these parametric design equations are useful, they have their limitations in that to utilize the parametric equations accurately, a standard geometry is required, and scaling may be an issue because parametric equations are only suitable for structures within a certain range.

For less-generic bridge shapes or bridges outside of the specified parametric range, design options appear to be limited to experimental results or results from CFD. However, developing a practical design from either of these approaches could be challenging or inaccurate. Small-to-medium-scale experiments are expensive to set up; data analysis is time-intensive and scaled models suffer from atmospheric pressure scaling issues discussed in-depth by Cuomo et al. (2009). CFD analysis could be feasibly implemented using common software packages such as Open FOAM (Greenshields, 2015), StarCCM+ (CD-adapco, 2017), or Fluent (Fluent, 2009). But, setting up any of these computational models requires unique expertise, and these models are computationally expensive. Depending on the resolution/accuracy required, the number of available processors, and the type of computer used, CFD computations could take up to a month. It would be beneficial if an alternative physics-based computational model could be developed for computing wave forces on bridges that was relatively computationally inexpensive.

1.2. Goals and Objectives

The Meng (2008) and Jin and Meng (2011) studies presented a strong starting point for the development of such a low-cost computational model. During these studies, the potential flow equations for wave diffraction around a bridge were solved on a simple computational grid using known boundary conditions and a finite difference scheme. Esteban et al. (2015) provided theoretical evidence supporting the Meng (2008) and Jin and Meng (2011) approaches. As discussed by Esteban et al. (2015), when a structure's length dimensions are similar to wave height and wavelength, diffraction tends to govern forcing. However, Meng (2008) and Jin and Meng (2011) only considered the cases where the bridge was initially fully inundated. As a result, it would appear that computation of trapped air effects could be improved. Meanwhile, the Cuomo et al. (2009) provided boundary closure for the situation where the surface boundary is bound by a trapped air surface.

Analysis of experimental data from previous studies indicated that maximum wave uplift forcing occurred when the initial water surface was at the same elevation as the bottom bridge chord. Similarly, forensic hindcasting of Hurricane Ivan appeared to show that the failed spans corresponded to loci where the water elevation was near the bridge bottom chord elevation.

The goal of the study presented here was 1) to combine the Jin and Meng (2011) diffraction model with boundary conditions described by the Cuomo et al. (2009) trapped air model; 2) to use these results to compute forcing on bridges under wave attack during worst-case vertical uplift forcing conditions (i.e. when the water surface was at the same elevation as the bottom bridge chord elevation); and 3) to compare these computational results to data from Marin and Sheppard (2009) and Marin (2010).

Chapter 2 METHODOLOGY

2.1. Experimental Data

Marin and Sheppard (2009) and Marin (2010) described their experimental data extensively. To summarize, their physical model was a two-lane 1:10 scaled representation of the failed Escambia Bay Bridge. Tests were conducted in a 6-ft (1.8 m) wide by 6-ft (1.8 m) tall by 120-ft (36.6 m) long wave channel at the University of Florida (UF) whereby the modeled deck was hung from the top of the wave tank and subjected to wave attack. Load cells were used to measure vertical and horizontal forcing on the structures. Several combinations of wave periods, water depths, and wave heights were used throughout their study. Bridge configurations without overhangs or railings, with overhangs but without railings, and with both overhangs and railings were tested. In an effort to simplify the computational model to some extent, only the cases without overhangs and railings were examined during this study. A schematic of the model bridge is presented in Figure 2-1:

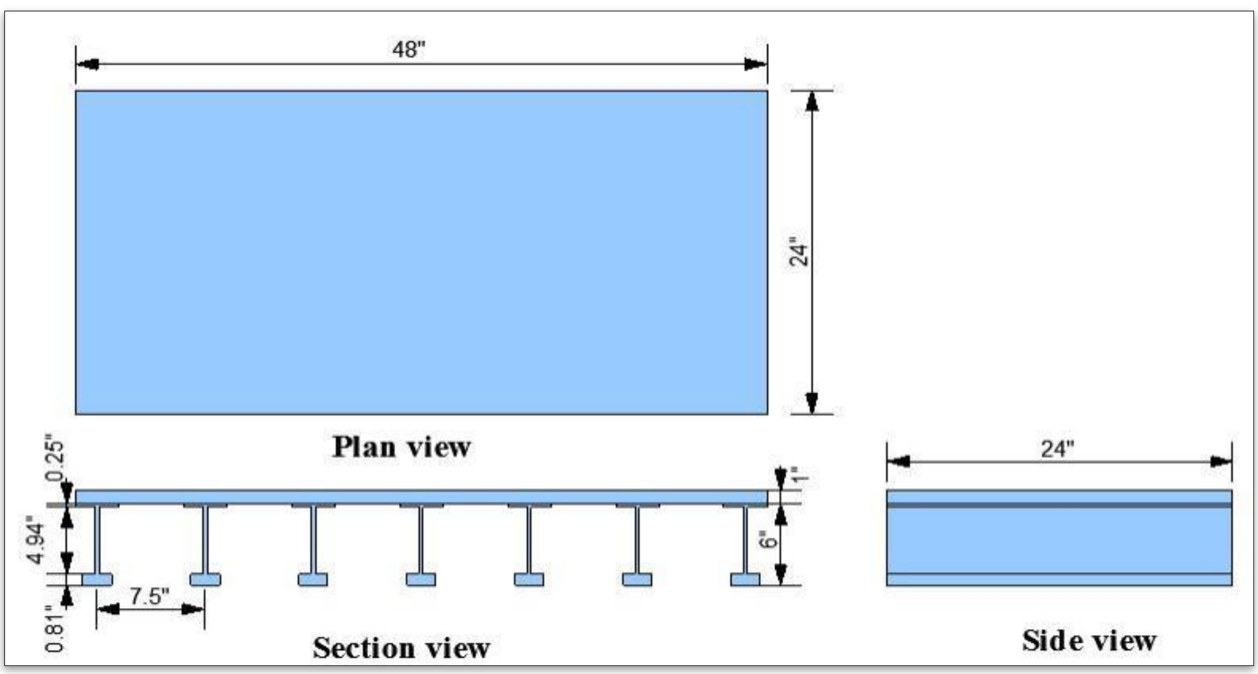

Figure 2-1. Experimental Bridge Schematic

2.2. Description of Numerical Model

2.2.1. Diffraction Model Formulation

Following Meng (2008) and Jin and Meng (2011), a diffraction model was used to describe wave flow around the modeled bridges. Water was assumed to be inviscid and incompressible, while flow was assumed to be irrotational. As such, a linearized complex velocity, φ could be defined as:

$$\varphi(x, z, t) = Re(\Phi(x, \mathrm{z})e^{-i\omega t}) \tag{2-1}$$

Where $Re(\,)$ denotes real part of a complex expression; t is the time; $i = \sqrt{-1}$; ω is the angular velocity; and Φ is the complex spatial potential that must satisfy Laplace's equation everywhere in the modeled fluid domain:

$$\nabla^2\Phi = \frac{\partial^2\Phi}{\partial x^2} + \frac{\partial^2\Phi}{\partial \mathrm{z}^2} = 0 \tag{2-2}$$

The spatial velocity potential was assumed to be comprised of two parts – an incident spatial potential Φ_I and a diffracted spatial potential Φ_D.

2.2.2. Trapped Air Model Formulation

The role of trapped air in hydrodynamic wave forcing on structures has been studied by a number of researchers over the years. Bagnold (1939) investigated the role of compressed air on breakwaters. Mitsuyasu (1966) developed a model based upon Bagnold (1939) that took pressure decay and air release into account. Takahashi et al. (1985) extended this work further by developing a model to describe trapped air on horizontal structures and on the ceiling slabs of wave-dissipating caissons. Cuomo et al. (2009), Araki and Deguchi (2015) and Seiffert et al. (2015) applied similar models to bridges under wave attack. Following Cuomo et al. (2009), consider the definition sketch in Figure 2-2 below:

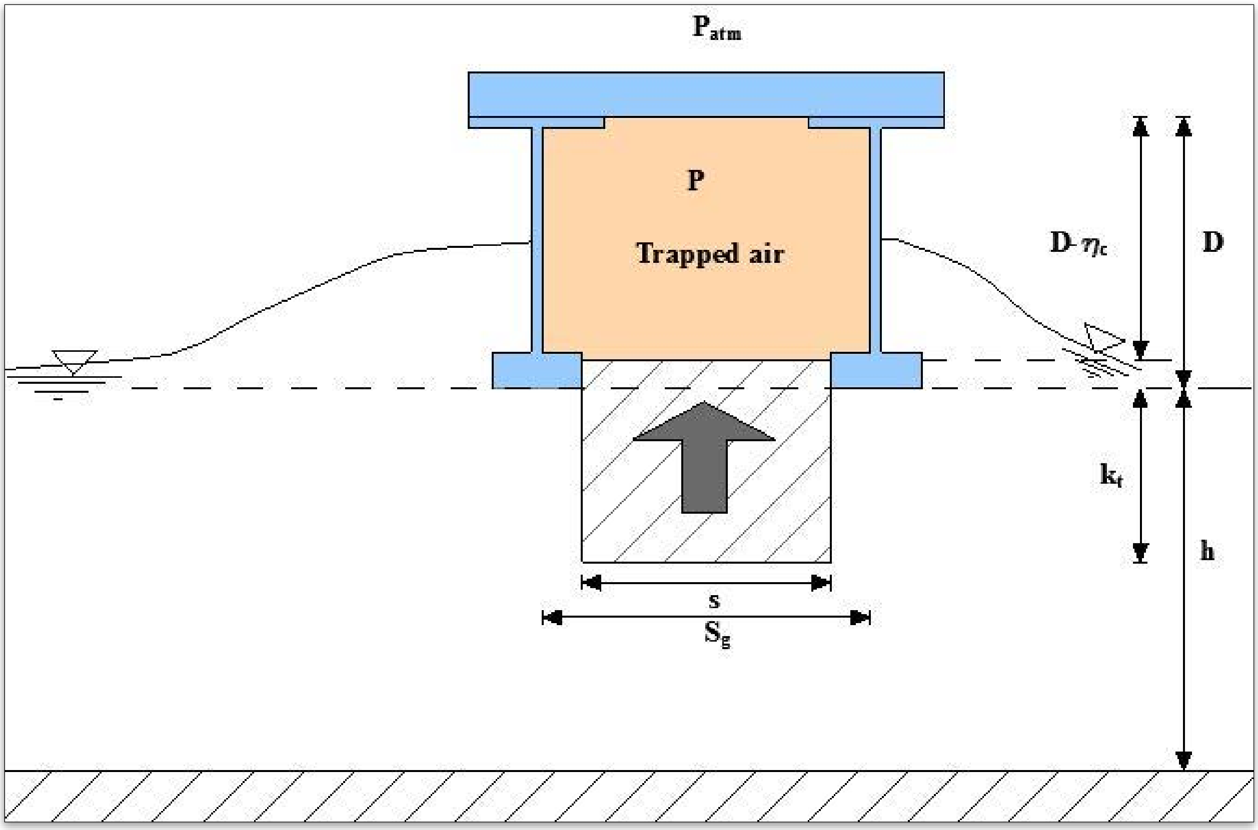

Figure 2-2. Representation of the trapped air terms and considered effective water column

in which p_{atm} is atmospheric pressure; p is the absolute pressure at any time in the trapped air cavity; s_g is the spacing between bridge girders; D is the depth of the girders; b is the width of the structure into the page; h is the water depth; and η_c is the displacement of the water surface within the girder cavity. Newton's second law is often approximated as:

$$\Sigma F = m\frac{d^2z}{dt^2} \tag{2-3}$$

in which ΣF is the sum of all external forces on an object; m is the object's mass; and $\frac{d^2z}{dt^2}$ is the object's acceleration in the z-direction (i.e. the second derivative of the free surface position in the vertical direction). For the case when the bottom bridge chord and water surface are at the same elevation, air is "sealed" between the girders. Let an arbitrary block of water below the sealed girder space be defined by a density, ρ; width, b; length, s; and thickness, k_t. The only external

force acting on this block of water is pressure from the trapped air cavity. Thus, Equation 2-4 may be applied:

$$(p - p_{atm})sb = \rho sbk_t \frac{\partial^2 \eta_c}{dt^2} \tag{2-4}$$

in which η_c is the free surface elevation. Canceling like-terms:

$$p - p_{atm} = \rho k_t \frac{\partial^2 \eta_c}{dt^2} \tag{2-5}$$

Finally, assume air is an ideal gas, and adiabatic expansion equation may be used to couple p with p_{atm}:

$$\frac{p_{atm}}{p} = \left(\frac{D - \eta_c}{D}\right)^{\gamma} \tag{2-6}$$

where γ is the polytropic index for air. Sirovich et al. (1996) indicated that this is usually assumed to be 1.4. At the moment the air cavity is sealed, $D - \eta_c$ must equal to D and $\frac{\partial \eta_c}{dt}$ must be the water surface velocity upward, u_0. Equation 2-5 and Equation 2-6 may be solved simultaneously with these initial conditions if a value of k_t is assumed. The correct value of k_t has been a point of contention in the literature, and over the years, a number of methods for determining this variable have been proposed (Table 2-1).

Table 2-1. Different Values of the effective thickness of water mass

Author	$\boldsymbol{k_t}$ ***value***
(Bagnold, 1939)	Should be determined experimentally
(Takahashi et al., 1985)	$k_t = \frac{\pi s_g}{4}$
(Cuomo et al., 2009)	$k_t = h$
(Araki and Deguchi, 2015; Sawaragi, 1995)	$k_t = \frac{\pi s_g}{8}$

2.2.3. Boundary Conditions to Couple Trapped Air with Diffraction Model

Consider the definition sketch in Figure 2-3 for a wave approaching a bridge in a computational fluid domain:

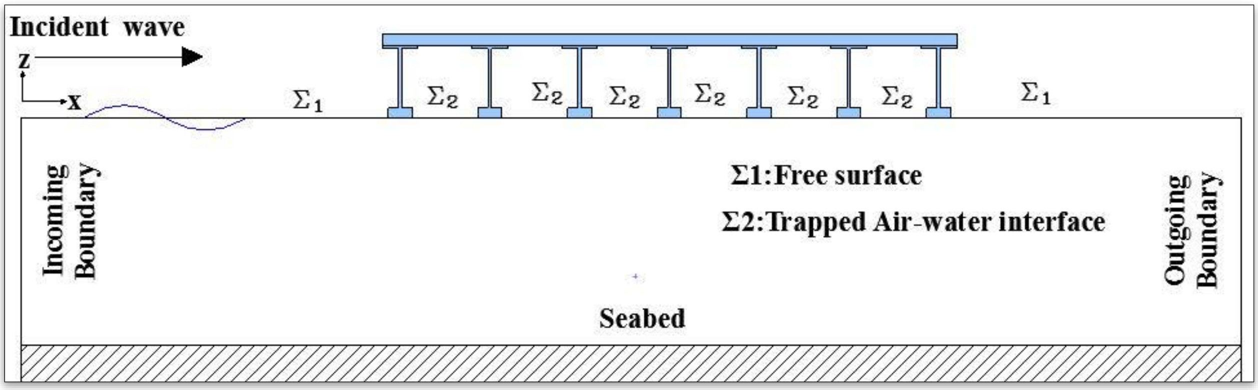

Figure 2-3. Boundary condition definition sketch

Equation 2-2 can be solved everywhere in the fluid domain if boundary conditions are imposed. At the bottom of the fluid domain (i.e. the seabed):

$$\frac{\partial \Phi}{dn} = 0 \tag{2-7}$$

Where *n* is a directional vector normal to the bottom of the domain. According to Panchang et al. (1988), at the incoming boundary, the Sommerfeld condition must be imposed:

$$\frac{\partial \Phi}{\partial x} - ik(\Phi_I - \Phi_R) = 0 \tag{2-8}$$

in which Φ_R is a scattered component given by:

$$\Phi_R = \Phi - \Phi_I \tag{2-9}$$

and *k* is the wave number. Simplifying Equation 2-8 and combining with Equation 2-9:

$$\frac{\partial \Phi}{\partial x} - ik(2\Phi_I - \Phi) = 0 \tag{2-10}$$

and at the outgoing boundary:

$$\frac{\partial \Phi}{\partial x} - ik\Phi = 0 \tag{2-11}$$

On the free surface, three boundary conditions are shown in Figure 2-3. Upstream and downstream from the bridge, the combined kinematic and dynamic free surface boundary conditions may be applied:

$$\frac{\partial\Phi}{\partial z} - \frac{\omega^2\Phi}{g} = 0 \tag{2-12}$$

When the free surface is bound by the structure,

$$\frac{\partial\Phi}{\partial z} = 0 \tag{2-13}$$

When the free surface is bound by a trapped air cavity (i.e. in regions marked Σ_2 in Figure 2-3), air pressure must drive the free surface's flow. Thus, Equation 2-5 and Equation 2-6 can be used in lieu of the usual dynamic free surface boundary condition to solve for η_c as a function of time. Then, η_c may be used to solve for velocity potential via the kinematic free surface boundary condition:

$$\frac{\partial\Phi}{\partial z} = \frac{\partial\eta_c}{\partial t} \tag{2-14}$$

2.2.4. Solving the Coupled Equations

A finite difference algorithm was used to solve the velocity potential everywhere within the fluid regime by discretizing the regime into 0.25-inch by 0.25-inch (6.35-mm by 6.35-mm) intervals in the horizontal and vertical directions. As shown below, results indicate that this resolution was sufficient to match data. Velocity potential was solved at each node using the typical finite difference algorithm for a rectangular mesh (Canale and Chapra, 1991):

$$\Phi_{(i,j)} = \frac{(\Phi_{(i,j+1)}+\Phi_{(i+1,j)}+\Phi_{(i,j-1)}+\Phi_{(i-1,j)})}{4} \tag{2-15}$$

and discretized (via forward-difference) boundary conditions. At the bottom of the fluid domain:

$$\Phi_{(i,N_z)}=\Phi_{(i,N_z-1)} \tag{2-16}$$

At the incoming boundary:

$$\Phi_{(1,j)} = \frac{4ik\Delta x}{2+ik\Delta x}\Phi_{I(1,j)} - \left(\frac{-2+ik\Delta x}{2+ik\Delta x}\right)\Phi_{(2,j)} \tag{2-17}$$

At the outgoing boundary:

$$\Phi_{(N_x,j)} = \left(\frac{2+ik\Delta x}{2-ik\Delta x}\right)\Phi_{(N_x-1,j)} \tag{2-18}$$

Where the structure was bound by the free surface:

$$\Phi_{(i,N_{cz})} = \Phi_{(i,N_{cz-1})} \tag{2-19}$$

On the free surface away from the structure:

$$\Phi_{(i,1)} = \left(\frac{2+\frac{w^2}{g}\Delta z}{2-\frac{w^2}{g}\Delta z}\right)\Phi_{(i,2)} \tag{2-20}$$

And finally when the free surface was bound by a trapped air cavity, the kinematic free surface boundary condition was discretized:

$$\Phi_{i,1} = \Phi(i,2) + \Delta z\left(\frac{\partial\eta_c}{\partial t}\right)_{i,1} \tag{2-21}$$

In these expressions, N_x is the number of nodes in the horizontal direction; N_z is the number of nodes in the z-direction; N_{cz} denotes the structure position; Δx denotes the step-size in the x-direction; and Δz denotes the step-size in the z-direction. At the corner points of the fluid domain and bridge superstructure, velocity potentials were corrected by taking the average of the corresponding horizontal/vertical potential values. These discretized equations were solved using a MATLAB algorithm whereby a coefficient matrix was assembled at each node; its inverse was found using MATLAB's built-in inversion algorithm; and the inverse matrix was multiplied by the corresponding boundary condition matrix to yield velocity potential. A schematic of this algorithm is presented in Figure 2-4:

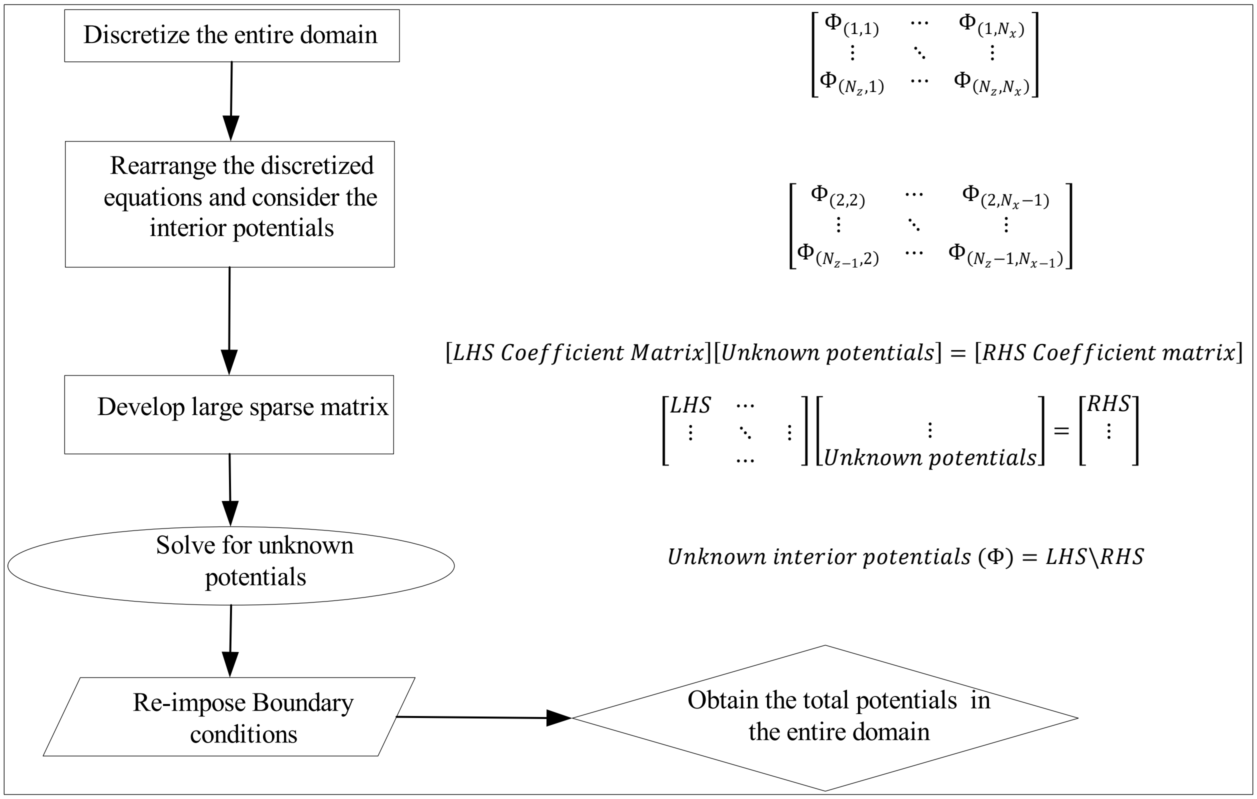

Figure 2-4. Finite Difference Solver Flow Chart

Once velocity potential had been solved, the dynamic free surface boundary condition:

$$\frac{\partial \Phi}{\partial t} + \frac{P_c - P_o}{\rho} + g\eta_c = 0 \tag{2-22}$$

was used to compute pressure and water surface elevation.

2.2.5. Some Subtle Notes about the Algorithm

As stated above, the trapped air model was only used to drive free surface pressure when the girders were sealed. To determine when this occurred, the model was first run for each wave condition combination (i.e. depth, period) without considering trapped air. Thus, the inherent assumption was that the trapped air did not significantly affect the wave celerity. Then, this sealed timing sequence was used to drive the trapped air algorithm described above at each discretized time step. As such, the model was "one-way coupled" in the sense that the trapped air was used to drive the free surface, but feedback from the free surface was not used to drive trapped air at each

time step. Another inherent assumption behind this approach was that the pressure in each trapped air chamber was constant spatially. It should also be noted that results were computed using each of the values for k_t shown in Table 2-1, and these results were compared with data. As stated above, data were used to back-solve for k_t and these values for k_t were plotted against wave/geometrical values to yield a value for k_t based upon data.

2.2.6. Force Computations

Water forces on the structure were computed by integrating the water pressures contacting the bridge superstructure in the horizontal and vertical directions (Dean and Dalrymple, 1999). Trapped air forces were computed by integrating air pressure along the bottom of the bridge deck in the vertical direction. Buoyancy forces caused by water displacement due to the structure and air were computed by multiplying displaced water volume by the water density. A schematic of these force integrations is presented in Figure 2-5:

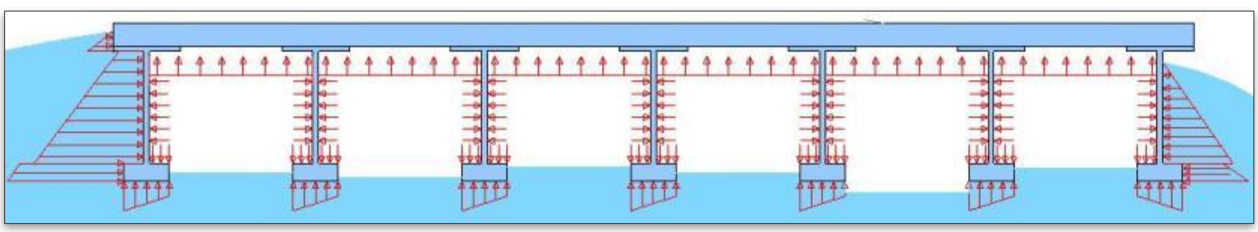

Figure 2-5. Force Integration Schematic

Following Marin and Sheppard (2009) and Marin (2010), total force was divided into two components – a quasi-static component and a high-frequency oscillatory component (called a "slamming force" by Marin and Sheppard (2009) and Marin (2010)). The quasi-static force was defined as the water pressure force plus the buoyancy force while the high-frequency oscillatory force was the force due to the trapped air oscillations. It should be noted that "green water" loading – or loading due to water overtopping the structure was neglected throughout the computations.

2.2.6. Model Evaluation

The forces computed using several effective thickness of water masses (Table 2-1) were compared with experimental data to assess the model predictive performance. Several statistical indicators were selected to evaluate the model's performance. These parameters are the Mean Biased Errors (MBE), Mean Absolute Error (MAE), Mean Absolute Percentage Error (MAPE), Root Mean Squared Error (RMSE), Correlation Coefficient (R), Coefficient of Determination (R^2), Index of Agreement (IA), and Standard Deviation (SD). Equations for each of the variables are presented in Table 2-2. In addition to the above mentioned parameters, a slope of fitted regression line was used to assess the model prediction's capability.

Table 2-2. Parameter Calculation Equations

Parameter	Calculation Equation
Mean Biased Error (MBE)	$MBE = \frac{1}{n}\sum_{i=1}^{n}(M_i - O_i)$
Mean Absolute Error (MAE)	$MAE = \frac{1}{n}\sum_{i=1}^{n}\lvert M_i - O_i\rvert$
Root Mean Squared Error (RMSE)	$RMSE = \sqrt{\frac{1}{n}\sum_{i=1}^{n}(M_i - O_i)^2}$
Correlation Coefficient (R)	$R = \frac{1}{(n-1)}\sum_{i=1}^{N}\left(\left(\frac{O_i - \bar{O}}{\sigma_o}\right) \times \left(\frac{M_i - \bar{M}}{\sigma_m}\right)\right)$
Coefficient of Determination (R^2)	$R^2 = \left(\frac{1}{(n-1)}\sum_{i=1}^{N}\left(\left(\frac{O_i - \bar{O}}{\sigma_o}\right) \times \left(\frac{M_i - \bar{M}}{\sigma_m}\right)\right)\right)^2$
Index of Agreement (IA)	$IA = 1 - \frac{\sum_{i=1}^{n}(M_i - O_i)^2}{\sum_{i=1}^{n}(\lvert M_i - \bar{O}\rvert + \lvert O_i - \bar{O}\rvert)^2}$
Standard Deviation (SD)	$SD = \sqrt{\frac{1}{n}\sum_{i=1}^{n}(X - \bar{X})^2}$
Slope (M)	$M = \frac{\Delta(Forces)_{predicted}}{\Delta(Forces)_{actual}}$

Where;

M_i is the predicted value

O_i is the actual value

σ_o is the standard deviation of actual values

σ_m is the standard deviation of predicted values

$\bar{X},\ \bar{M}$ & $\bar{O}$ are the mean values respectively

Chapter 3 RESULTS

3.1. Effective Thickness of Water Mass Study

It is apparent from the Bagnold (1939) trapped air model that the effective thickness of water mass (k_t) plays a significant role in absolute pressure created due to air entrapment in that an increase in effective thickness corresponds to an increase in trapped air pressure (Figure 3-1).

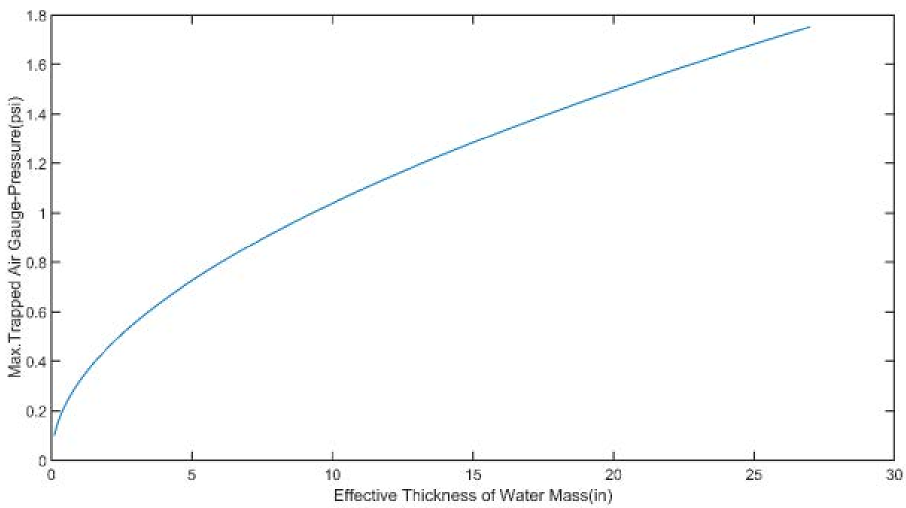

Figure 3-1. Variation of Maximum Trapped Air Pressure with Effective Thickness of Water Mass

As summarized above in Table 2-1 and discussed briefly above, several authors have proposed various values for k_t over the years. During this study, k_t was further analyzed for a range of values from 0.1 inches (2.54 mm) to the total water depth, h using a discretized time step of 0.001 seconds. Each value for k_t was used to compute high-frequency uplift force on the bridge as a function of time. Maximum total high-frequency uplift force was plotted as a function of k_t (Figure 3-2) to illustrate the influence of the effective water mass thickness on the high-frequency oscillatory force.

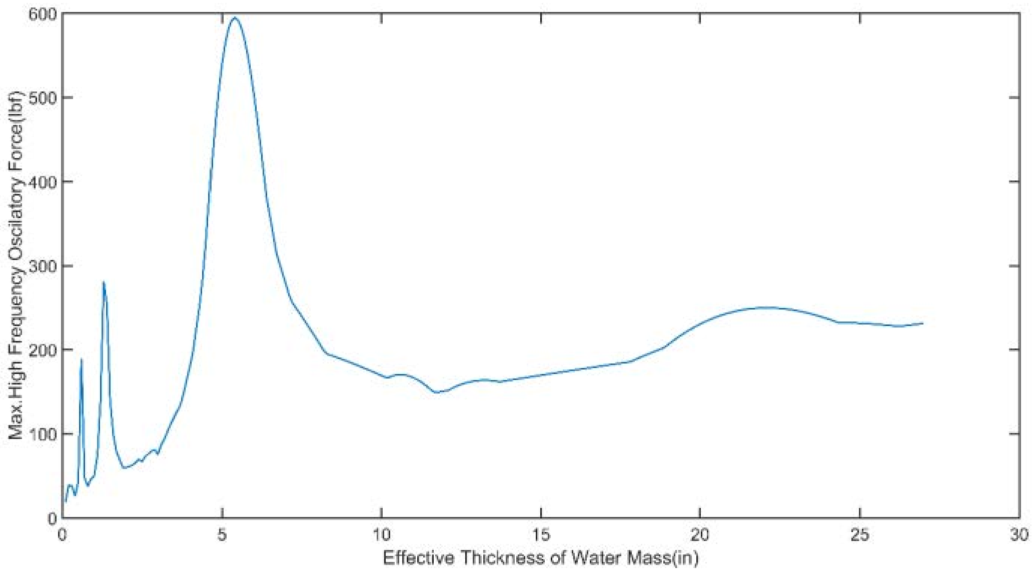

Figure 3-2. Variation of High Oscillatory Force with Effective Thickness of Water Mass

In addition, different values of k_t from literature were used to compute high-frequency oscillatory force to further illustrate k_t's importance. Force results were normalized as a function of wave energy per unit length $(\rho g H^2 L)$ and plotted as a function of non-dimensionlized wavelength $\left(\frac{W}{\lambda}\right)$ as shown in Figure 3-3. In these expressions, W is the bridge width, λ is the wavelength, and L is the bridge length.

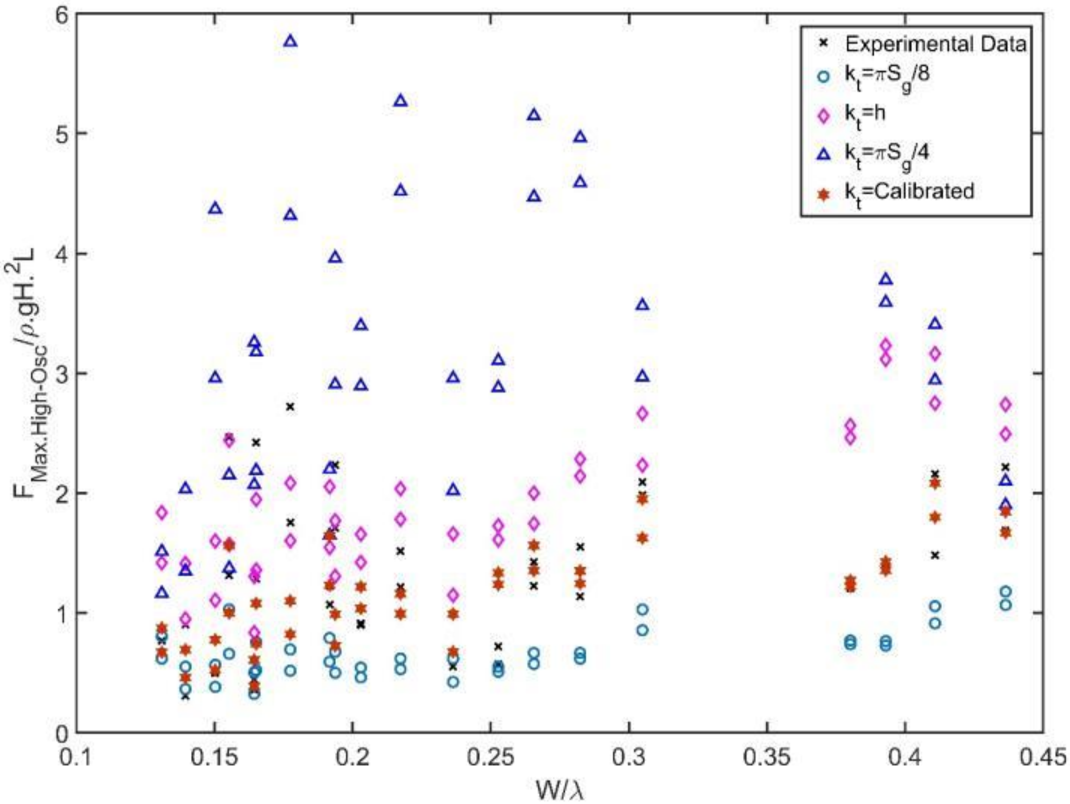

Figure 3-3. Comparison of High-frequency Oscillatory Force Computed Based on Different Effective Thickness of Water Mass from Literature

3.2. Calibration of k_t

As discussed by Bagnold (1939), one plausible method for determining k_t was to calibrate it from experimental data. Based upon the variability shown in Figure 3-3, such a calibration appeared to be warranted. Reported high-frequency oscillatory force data from Marin and Sheppard (2009) and Marin (2010) were used to calibrate k_t. For each experimental run, figures similar to Figure 3-2 were prepared, and the value for k_t that resulted in the force that most-closely corresponded to experimental data was dubbed "calibrated k_t." Investigators hypothesized that k_t should be a function of wave parameters. A large wave would tend to have significant momentum upward as it approaches the trapped air chamber. Under these conditions, pressure due to trapped

air should not significantly affect the water surface. Conversely, a small wave would tend to have less upward momentum, and therefore it would be more sensitive to trapped air pressure. After some trial-and-error/dimensional analysis, an empirical data fit was developed between wave parameters and k_t (Figure 3-4) where T is the wave period and all other terms have previously been defined.

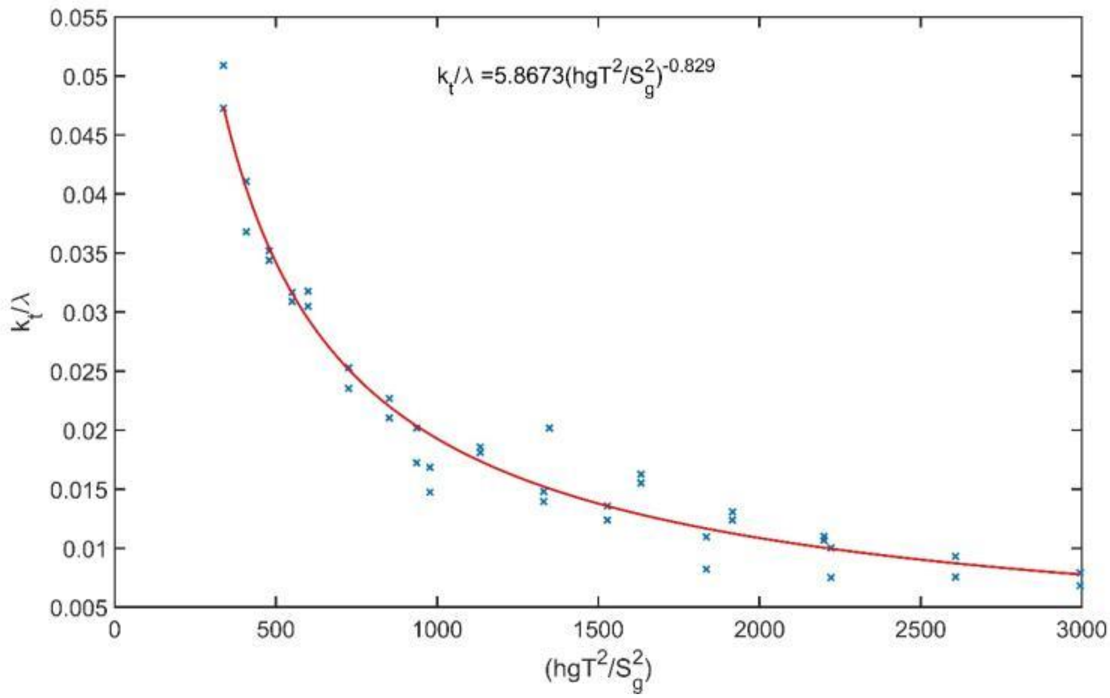

Figure 3-4. Calibration of Effective Thickness of Water Mass

This relationship was used to back-calculate a predicted value for k_t. These predicted values for k_t were plotted as a function of calibrated k_t from data to demonstrate the prediction model's quality (Figure 3-5).

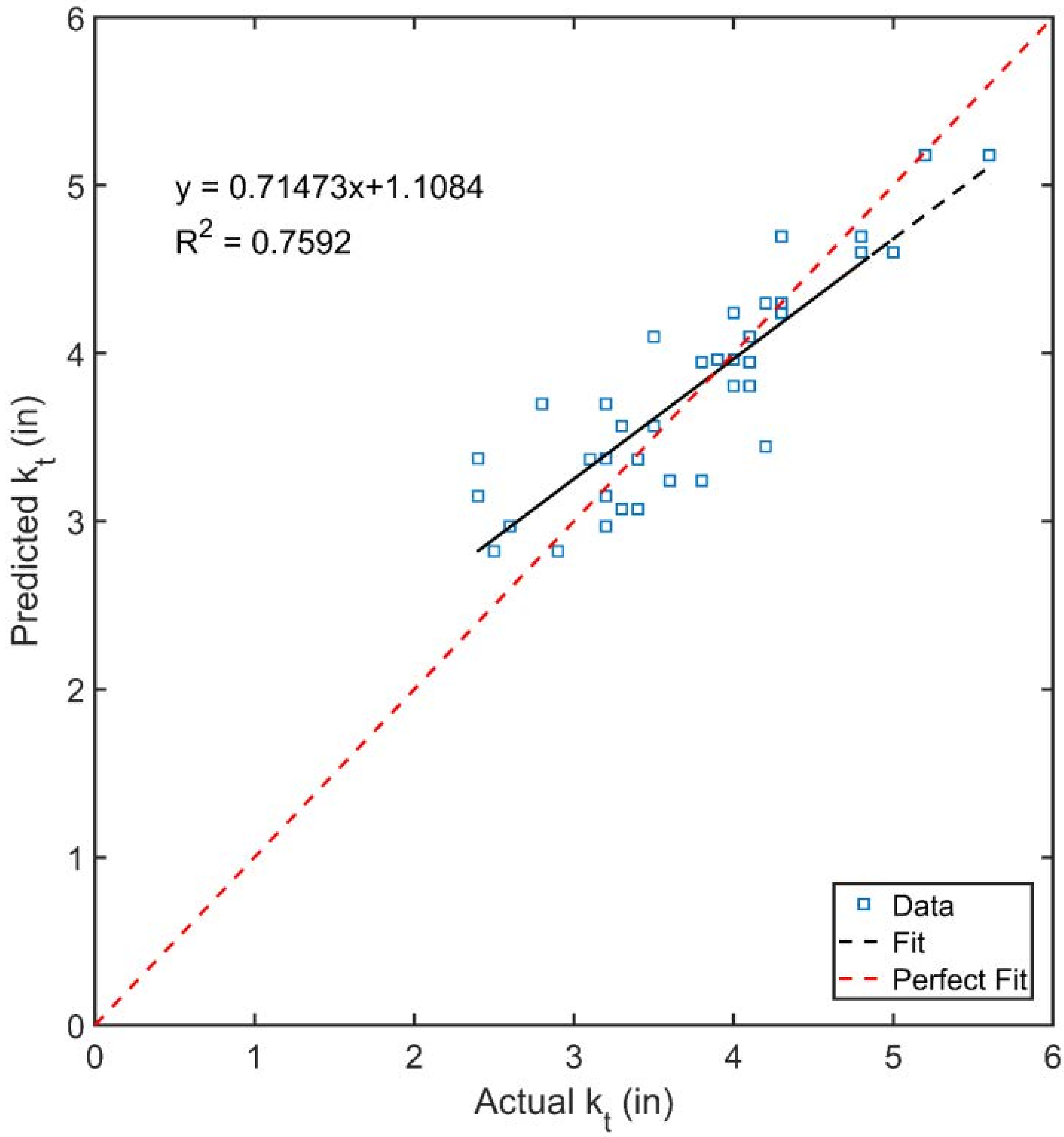

Figure 3-5. Comparison between Predicted and Actual Values of Effective Thickness of Water Mass, where the "perfect fit" assumes that this force should approach zero when k_t is zero.

3.3. Pressure and Force Time History

3.3.1. Trapped Air-Pressure Characteristics

One of the assumptions in this study was that there was no air leakage. Absolute pressures (Figure 3-6) computed numerically at each bridge chamber for a corresponding duration of sealing

time appeared to follow a sinusoidal pattern. This pattern conformed to the results of a study done by Cuomo et al. (2009) for the case with no leakage and no lateral air movement. In future work, it should be possible to take leakage into account via methods described in-depth by Cuomo et al. (2009).

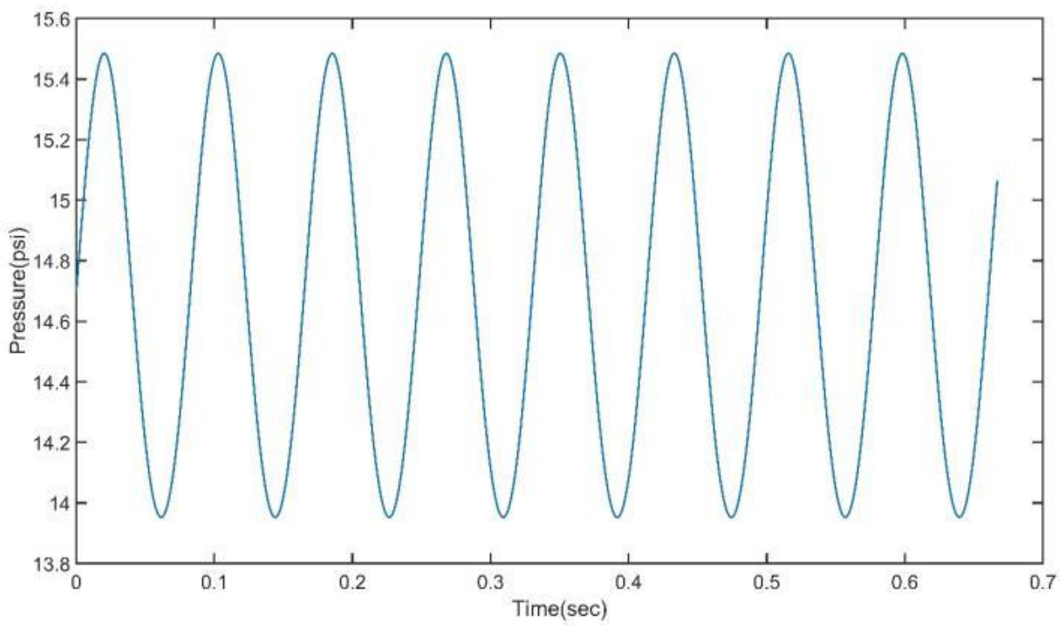

Figure 3-6. Pressure Time History during Sealing in One Chamber

3.3.2. Force Characteristics

Results of a typical force time history for vertical quasi-static force, high oscillatory force, total vertical force and horizontal forces are shown in Figure 3-7. They are representative of simulation of a BSXX136 test case from experimental work of Marin and Sheppard (2009) and Marin (2010). The simulation results are only for one wave period.

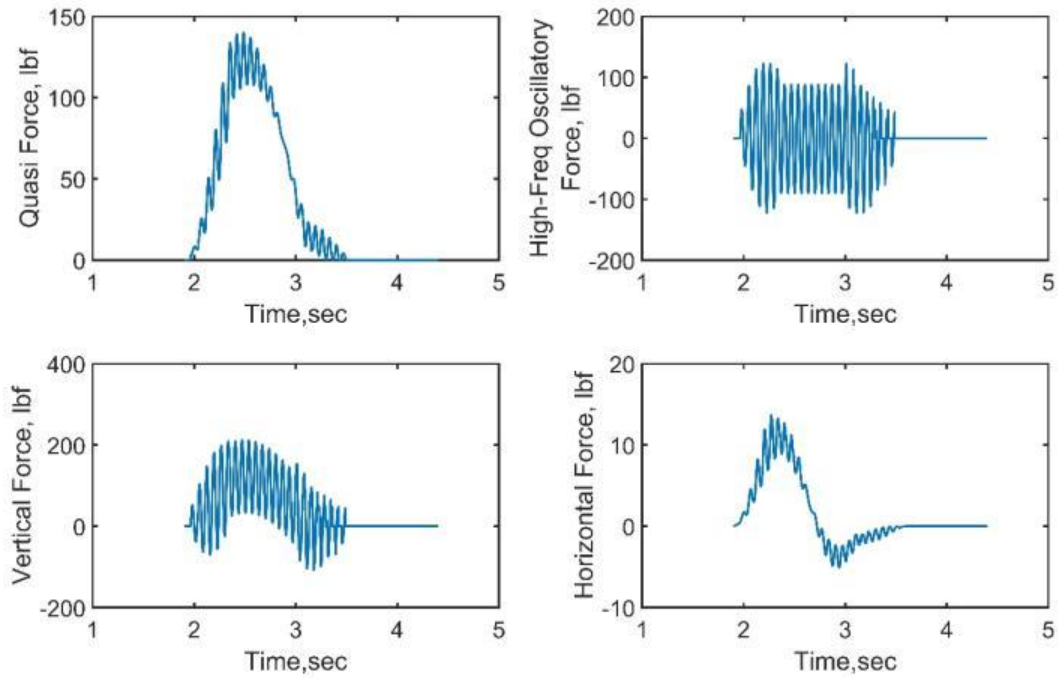

Figure 3-7. Representative Force Time History

3.4. Wave Height Influence on Wave Forces

Intuitively, as wave height increases, forcing should concomitantly increase (Jin and Meng, 2011; Meng, 2008). To demonstrate that the one-way coupled model behaved this way, a test-case was used whereby increasing wave heights were simulated while all other variables (water depth, wave period, etc.) remained constant. Results (Figure 3-8) demonstrate that the model appears to be behaving as designed.

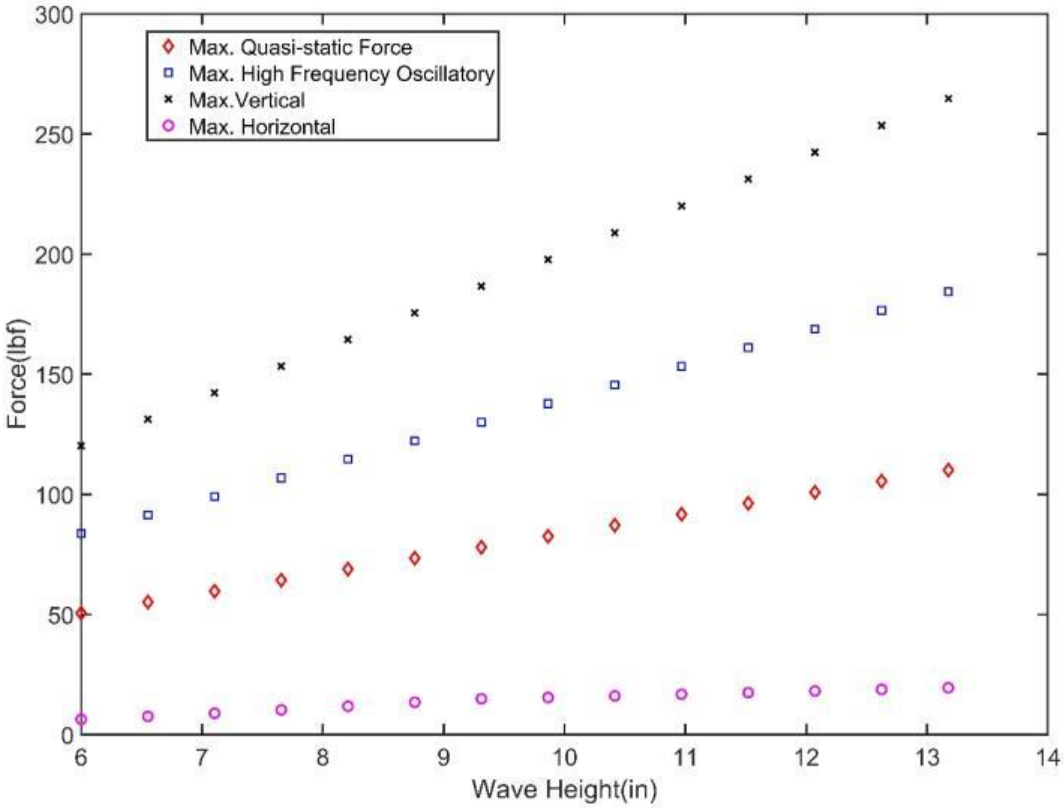

Figure 3-8. Maximum Wave Forces against Wave Heights

3.5. Role of Wave-Structure Interaction

Wave-structure interaction should have an influence on wave forces. To demonstrate that the new model took wave-structure effects into account, results were compared with the method described by Dean and Dalrymple (1999). Results (Figure 3-9) appear to indicate that diffraction is indeed having an effect on results – particularly on forcing in the horizontal direction.

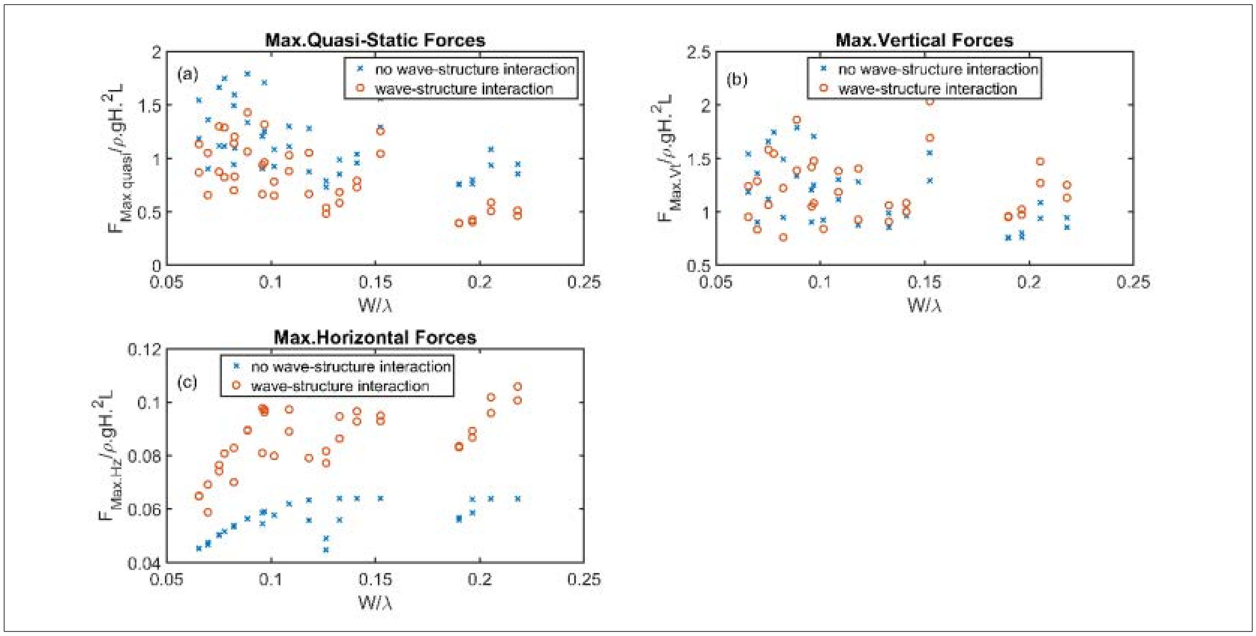

Figure 3-9. Comparison of Maximum Wave Forces Computed With and Without Wave-Structure Interaction

3.6. Comparison between Model Prediction and Experimental Results of Maximum Wave Forces

Once model behavior had been verified, investigators ran the model for each "BSXX" configuration reported in Marin and Sheppard (2009) and Marin (2010) (note that BSXX stands for bridge with girders, without side rails, and without overhangs) using each expression for k_t displayed in Table 2-1 and the newly calibrated values for k_t. Results are presented from Figure 3-10 through Figure 3-13. The model's statistical evaluation parameters for each expression of k_t were computed and their results are shown in Table 3-1.

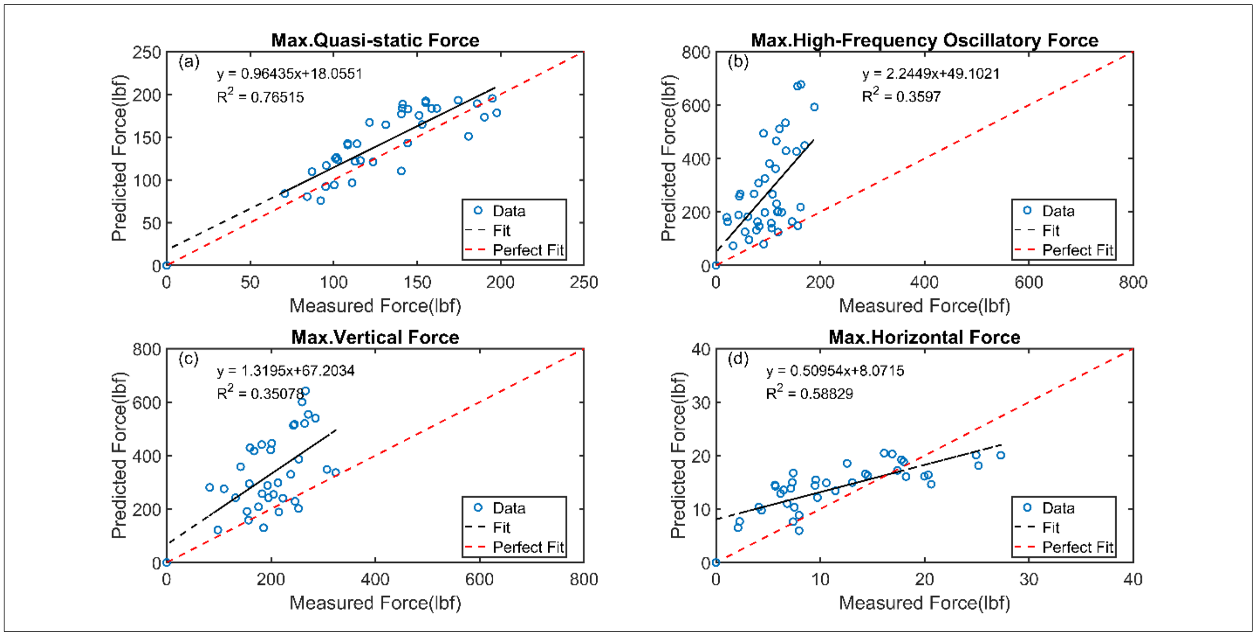

Figure 3-10. Comparison between Model Prediction and Experimental Values of Maximum Forces When the Effective Thickness of Water Mass $k_t = (\pi s_g)/4$

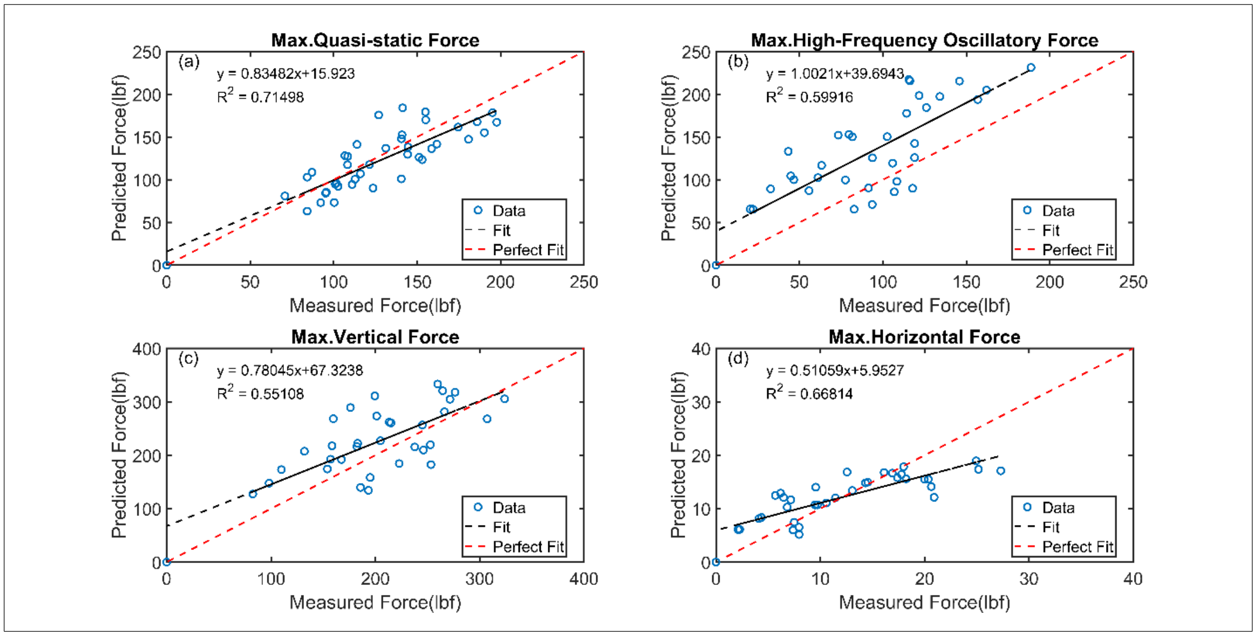

Figure 3-11. Comparison between Model Prediction and Experimental Values of Maximum Forces When the Effective Thickness of Water Mass $k_t = h$

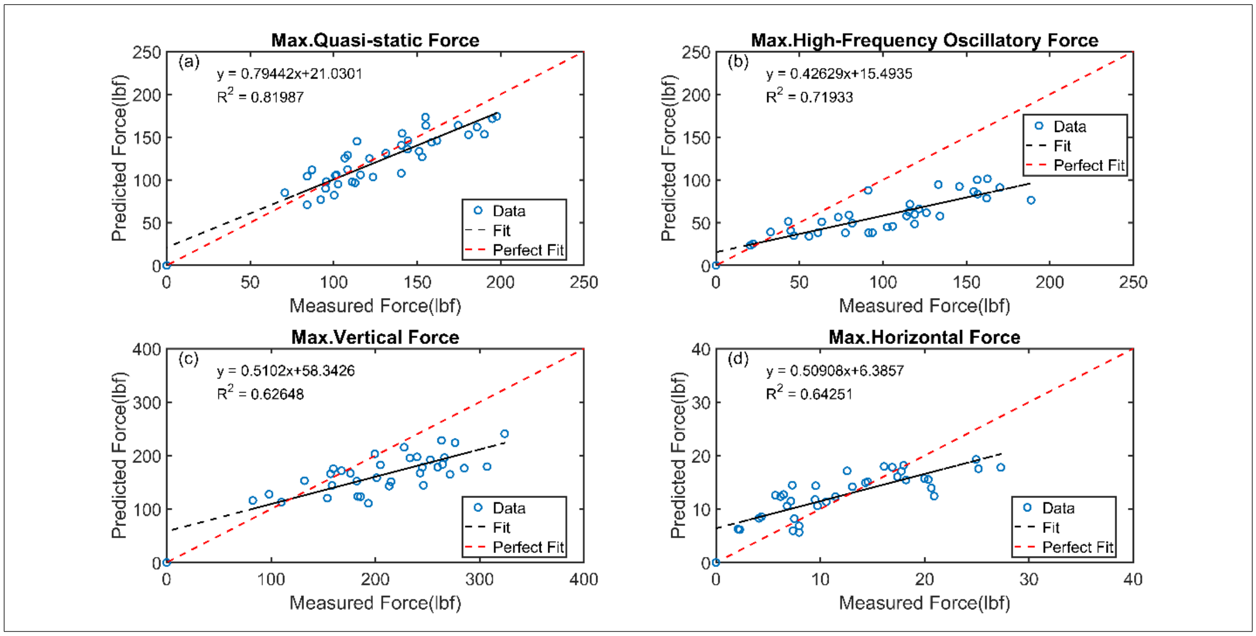

Figure 3-12. Comparison between Model Prediction and Experimental Values of Maximum Forces When the Effective Thickness of Water Mass $k_t = (\pi s_g)/8$

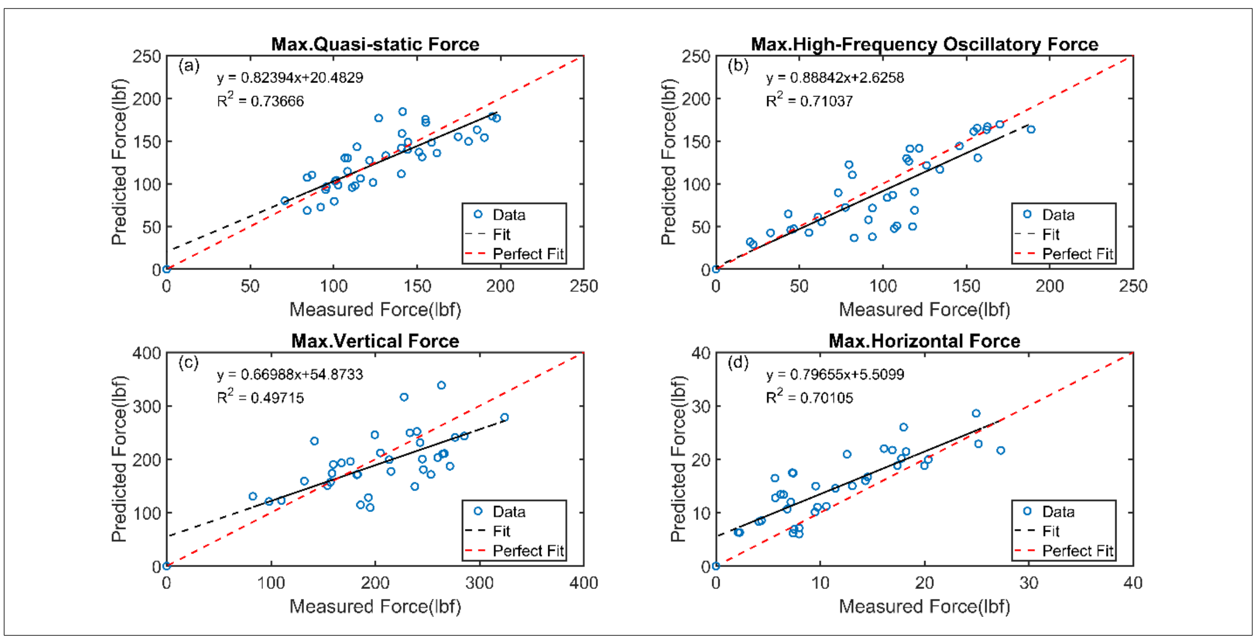

Figure 3-13. Comparison between Model Prediction and Experimental Values of Maximum Forces When the Effective Thickness of Water Mass k_t was calibrated

Table 3-1. Model Evaluation parameters for each effective thickness of water mass

Force Component	Parameter	$k_t = \frac{\pi S_g}{4}$	$k_t = h$	$k_t = \frac{\pi S_g}{8}$	Calibrated k_t
Horizontal Force	Correlation Coefficient, R	0.781	0.782	0.794	0.837
	Coefficient of Determination, R^2	0.610	0.612	0.631	0.701
	Mean Bias Error, MBE	2.563	0.962	1.237	3.180
	Mean Absolute Error, MAE	4.250	3.392	3.483	3.948
	Root Mean Squared Error, RMSE	4.969	4.397	4.368	4.923
	Index of Agreement, IA	0.815	0.836	0.842	0.866
	Standard Deviation, Experiment	6.821	6.821	6.821	6.821
	Standard Deviation, Model	4.640	4.403	4.487	6.489
Quasi-Static Force	Correlation Coefficient, R	0.849	0.846	0.865	0.858
	Coefficient of Determination, R^2	0.720	0.715	0.748	0.737
	Mean Bias Error, MBE	16.205	-5.052	-2.594	-1.873
	Mean Absolute Error, MAE	23.250	18.837	16.097	16.578
	Root Mean Squared Error, RMSE	27.775	21.890	19.692	20.259
	Index of Agreement, IA	0.881	0.913	0.926	0.923
	Standard Deviation, Experiment	39.038	39.038	39.038	39.038
	Standard Deviation, Model	42.875	38.542	36.388	37.476
High-frequency Oscillatory Force	Correlation Coefficient, R	0.615	0.782	0.808	0.843
	Coefficient of Determination, R^2	0.378	0.612	0.652	0.710
	Mean Bias Error, MBE	161.599	55.781	-46.544	-8.435
	Mean Absolute Error, MAE	162.625	60.888	47.586	20.271
	Root Mean Squared Error, RMSE	212.260	80.220	55.237	27.419
	Index of Agreement, IA	0.338	0.665	0.619	0.910
	Standard Deviation, Experiment	45.714	45.714	45.714	45.714
	Standard Deviation, Model	162.794	86.771	23.447	48.187
Total Vertical Force	Correlation Coefficient, R	0.580	0.659	0.669	0.690
	Coefficient of Determination, R^2	0.337	0.434	0.447	0.476
	Mean Bias Error, MBE	159.257	42.995	-45.639	-23.194
	Mean Absolute Error, MAE	166.921	63.529	56.031	42.436
	Root Mean Squared Error, RMSE	219.631	80.961	66.335	52.644
	Index of Agreement, IA	0.406	0.723	0.691	0.790
	Standard Deviation, Experiment	65.563	65.563	65.563	65.563
	Standard Deviation, Model	181.647	92.191	42.360	51.656

3.7. Role of entrapped air

Entrapped air should have an influence on the wave forces. To investigate this, the model was run without trapped air. Computed forces were compared with experimental data using calibrated k_t and k_t = h (Figure 3-14, Figure 3-15, and Figure 3-16).

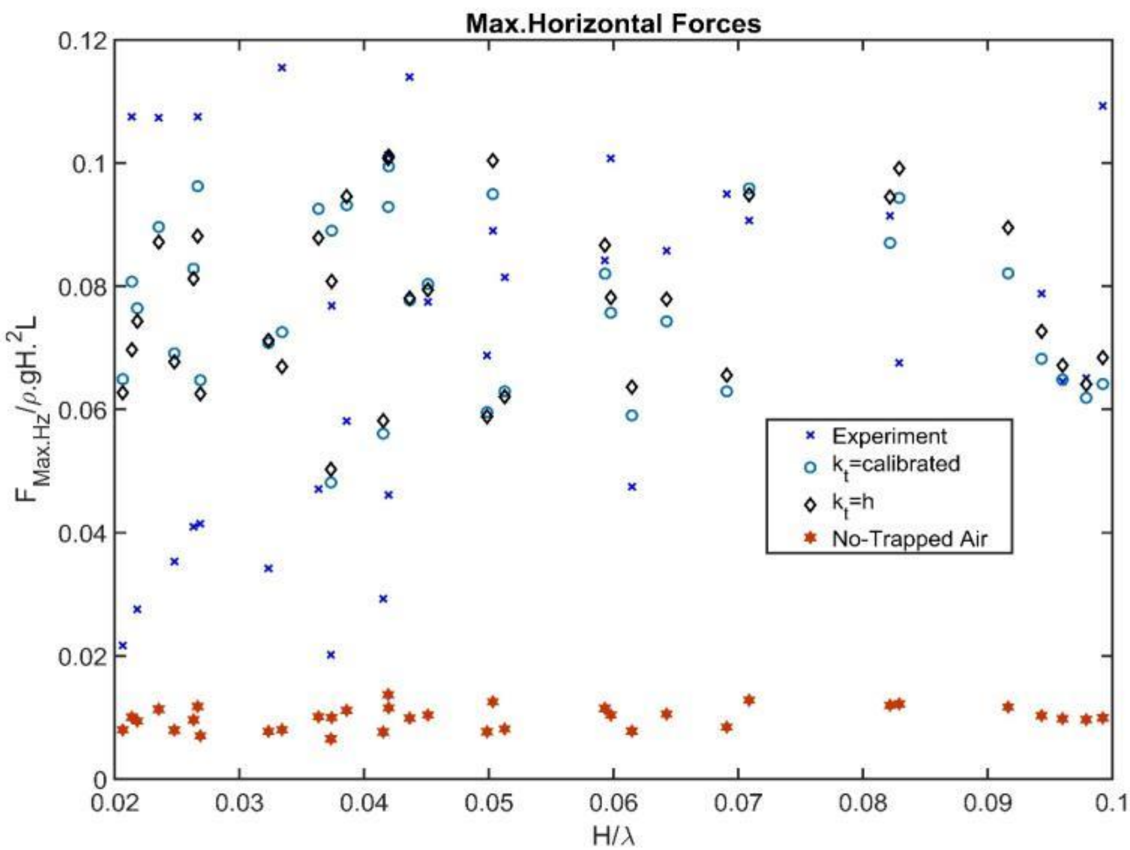

Figure 3-14. Comparison of Maximum Horizontal Forces obtained for the case of with and without trapped air (full venting)

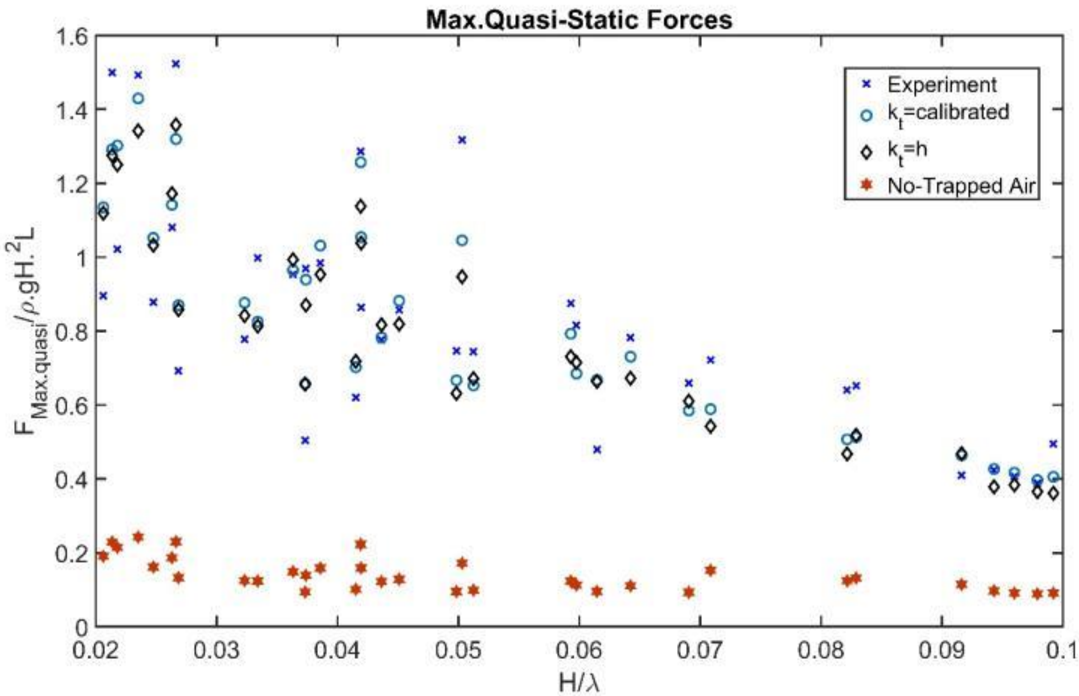

Figure 3-15. Comparison of Maximum Quasi-Static Forces obtained for the case of with and without trapped air (full venting)

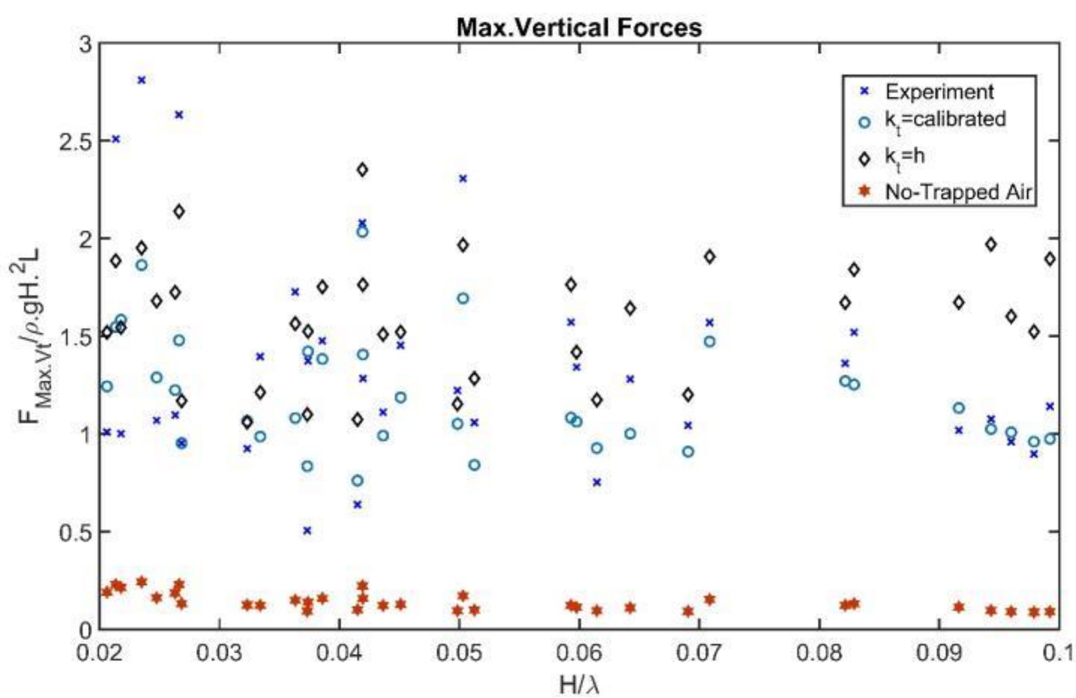

Figure 3-16. Comparison of maximum Vertical Forces obtained for the case of with and without trapped air (full venting)

The trapped air should also have an influence on force-time history. To demonstrate that, for each experimental run, the forces were computed at each time increment. The results of typical time history for horizontal and vertical forces are shown in Figure 3-17 below. They are representative of simulation of the BSXX136 test case.

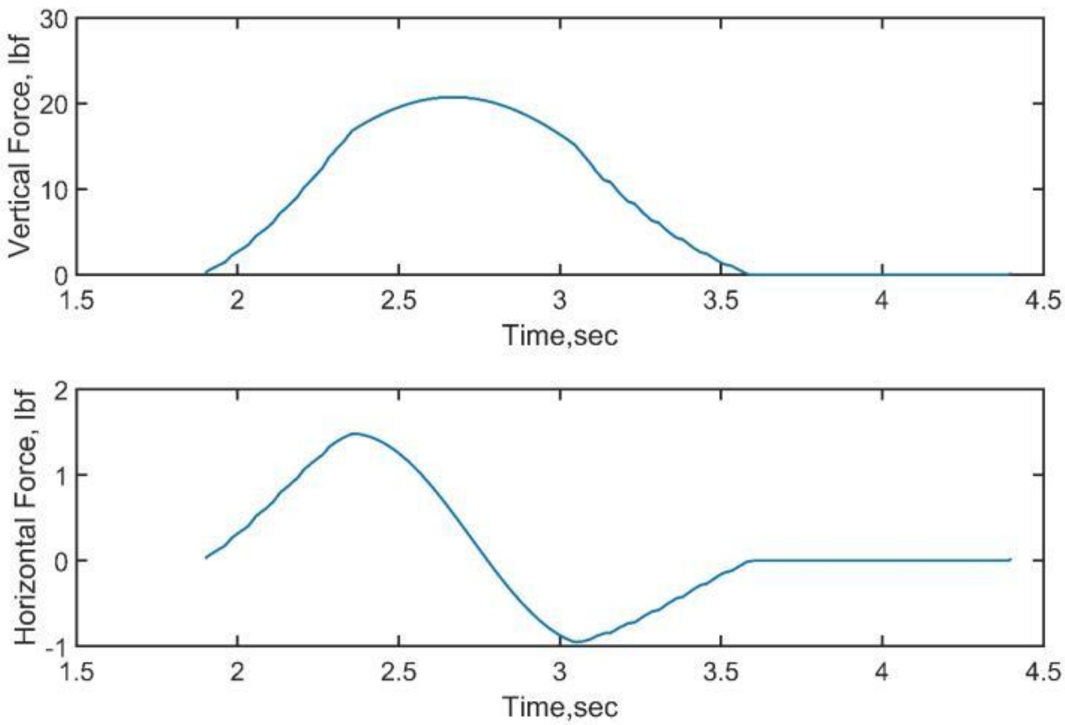

Figure 3-17. Force time history for the case of a full vented deck

Chapter 4 DISCUSSION

4.1. Comparison with Data

Overall, results suggest that a one-way coupled two-dimensional physics-based model such as the one presented here can be used to predict wave loading on bridge superstructures with reasonable accuracy as shown in error index, R-squared and t-test results. In particular, quasi-static forcing results appeared to be reasonably replicated for all values of k_t used during this study, although some variability was still observed. This appears to show slight variations in the effect of trapped air have only small effects on the quasi-static force.

High-frequency oscillatory force results were very sensitive to k_t. The two values for k_t that performed the best were $k_t = h$ and the calibrated k_t. For the $k_t = h$ situation, the slope of the best-fit line was 1.002 which is very close to that of experimental data (1.0), although the best-fit line was consistently 40 pounds higher than the data, and the corresponding R-squared value was relatively low. When k_t was calibrated, R-squared improved to 0.71 and the apparent shift appeared to be eliminated. When $k_t = \frac{\pi s_g}{4}$ or $k_t = \frac{\pi s_g}{8}$, high-frequency oscillatory forcing was badly over- and under-predicted respectively. Holistically, analysis of high-frequency oscillatory force results would appear to show that using a correct value for k_t is critical.

As illustrated in Table 3-1, the SD for the observed forces was captured by the modeled values, and the models with calibrated k_t appeared to perform the best when compared with the data. While a SD's difference of 21.21% may be considered relatively high, as will be discussed below, this model represents a first-step at creating a more-accurate PBM. There are several areas where this model could be improved that are discussed below. These modifications should improve this 21.21%. Error index results appear to support the idea that calibrated k_t performed better than other values of k_t.

Only the calibrated k_t model reproduced horizontal forcing with reasonable accuracy. The horizontal force should be significantly affected by wave-structure interaction terms because net horizontal forcing is caused by the upstream-downstream pressure gradient around the structure. As such, results imply that trapped air has an indirect effect on horizontal force. Physically, this appears to be reasonable because trapped air should influence diffraction.

Trapped air showed to have a significant impact on the wave forces acting on bridge superstructure. When trapped air was allowed to escape, the maximum forces computed were lower than the forces observed when full entrapment was considered. The forces were also lesser than the experimental forces for all test cases. This was expected because by allowing air to escape, the buoyancy force due to the displacement of water by trapped air is reduced. The horizontal force was also reduced when full venting was considered. Again, this supports the argument stated in the above discussion that trapped air influences diffraction which indirectly affects the horizontal force. This shows the potential of venting a bridge deck as one of the adaptive measures to reduce the wave forces.

4.2. Areas for Improvement

While this model appears to reproduce experimental data with reasonable accuracy, there are several areas where it could be improved. First, an inherent assumption throughout this model is that the wave-structure interaction does not reduce wave celerity. As discussed by Abrahamsen and Faltinsen (2011), trapped air-water interaction will transform some of the wave energy into heat which would then necessarily result in a decay in wave celerity over time.

In addition, this one-way coupled model assumed that air in each chamber (i.e. under each girder) compressed equally as a function of length along the bridge, and recent work has shown that this assumption is slightly inaccurate. Araki and Deguchi (2015) and Azadbakht and Yim

(2016) showed that the second chamber (girder space) experienced maximum trapped air pressure. Based upon data, it should be possible to define a pressure reduction coefficient as a function of bridge length, and this may help to improve future model results.

During the experiments, the maximum total uplift force was not the summation of the maximum quasi-static force and the maximum high-frequency oscillatory force. Rather, maximum total uplift was slightly out of phase with both of these values. When the one-way coupled model was used to compute maximum uplift force, it performed relatively poorly for all values of k_t including the case when k_t was calibrated from the data. This would appear to indicate that while the one-way coupled model performs well from a component-to-component perspective (i.e. in terms of horizontal, quasi-static vertical forcing, and high-frequency vertical forcing), these individual component results are out-of-phase with the data. This result adds further weight to the wave celerity issue described above.

4.3. Computational Time

As stated in the introduction, this model presents an important advantage when compared with other computational techniques in that it can generate results relatively quickly on common personal computers (during this study, an Intel i7 processor was used). On average, one computational run could be completed in approximately an hour.

Chapter 5 CONCLUSION AND RECOMMENDATIONS

A simplified physics-based model based on diffraction and trapped air models was developed. The model was applied to compute wave forces on bridge superstructures for various combinations of wave period, water depth, and wave height. Different values for the effective water mass thickness were computed, and data were used to calibrate a new expression for this variable. Entrapped air was found to have a small effect on resultant quasi-static forcing; a significant effect on high-frequency oscillatory forcing; and an indirect effect on horizontal forcing. Wave diffraction was also found to play a role in forcing results. While this model performed well on a component-by-component basis, its performance was less accurate from a total vertical uplift forcing perspective. This issue is believed to be due to one of the model's assumptions – that the bridge did not significantly slow the wave celerity.

Despite this, results on a component-by-component basis are strong and represent a potential next-step for future physics-based modeling of the wave-bridge interaction problem. The advantage of this model when compared with other computational techniques is that it can be run on a common personal computer with very little run-time (approximately an hour). While computational results using other techniques are very useful, this new model's speed and relative simplicity would appear to give it some advantages when compared to more-complicated modeling options. If the model can be improved to account for wave celerity changes and trapped air pressure variation as a function of air chamber location, it could serve as an important tool for future design equation development.

APPENDIX

A. DISCRETIZATION OF BOUNDARY CONDITIONS

The governing equations were discretized using the finite difference. Consider Figure A-1 below

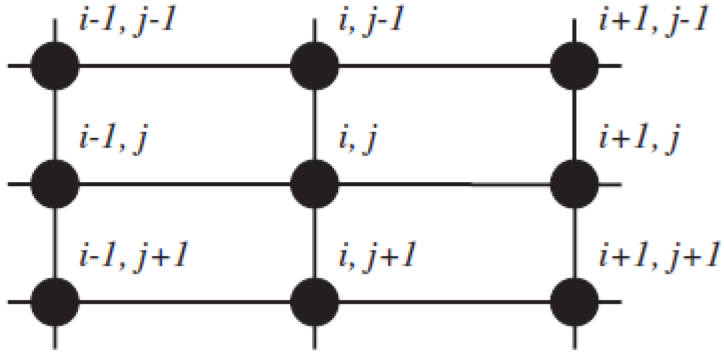

Figure A-1. Discretization of Fluid Domain

Incoming Boundary Conditions

$$\frac{\partial \Phi}{\partial x} - ik(2\Phi_I - \Phi) = 0 \qquad \text{A-1}$$

By discretizing $\frac{\partial \Phi}{\partial x} = \frac{\Phi_1 - \Phi_2}{\Delta x}$ and $\Phi = \frac{\Phi_1 + \Phi_2}{2}$, the following equation is obtained

$$\frac{\Phi_1 - \Phi_2}{\Delta x} - ik\left(2\Phi_I - \frac{\Phi_1 + \Phi_2}{2}\right) = 0 \qquad \text{A-2}$$

Rearrange and simplify the above equation

$$2\Phi_1 - 2\Phi_2 - 4ik\Delta x\Phi_I + ik\Delta x\Phi_1 + ik\Delta x\Phi_2 = 0 \qquad \text{A-3}$$

$$(2 + ik\Delta x)\Phi_1 + (-2 + ik\Delta x)\Phi_2 = 4ik\Delta x\Phi_I \qquad \text{A-4}$$

$$\Phi_1 = \left(\frac{4ik\Delta x}{2 + ik\Delta x}\right)\Phi_I - \left(\frac{-2 + ik\Delta x}{2 + ik\Delta x}\right)\Phi_2 \qquad \text{A-5}$$

Equation A-5 can be rewritten in terms of fluid domain coordinates as:

$$\Phi_{(1,j)} = \frac{4ik\Delta x}{2 + ik\Delta x}\Phi_{I(1,j)} - \left(\frac{-2 + ik\Delta x}{2 + ik\Delta x}\right)\Phi_{(2,j)} \qquad \text{A-6}$$

Outgoing boundary conditions

$$\frac{\partial \Phi}{\partial x} - ik\Phi = 0 \qquad \text{A-7}$$

$$\frac{\Phi_1-\Phi_2}{\Delta x} - ik\left(\frac{\Phi_1+\Phi_2}{2}\right) = 0 \qquad \text{A-8}$$

$$2\Phi_1 - 2\Phi_2 - ik\Delta x\Phi_1 - ik\Delta x\Phi_2 = 0 \qquad \text{A-9}$$

$$(2 - ik\Delta x)\Phi_1 - (2 + ik\Delta x)\Phi_2 = 0 \qquad \text{A-10}$$

$$\Phi_1 = \left(\frac{2+ik\Delta x}{2-ik\Delta x}\right)\Phi_2 \qquad \text{A-11}$$

In terms of fluid domain coordinates, equation A-11 can be written as:

$$\Phi_{(N_x,j)} = \left(\frac{2+ik\Delta x}{2-ik\Delta x}\right)\Phi_{(N_x-1,j)} \qquad \text{A-12}$$

Bottom/Seabed and when the structure was bound by the free surface

$$\frac{\partial\Phi}{dn} = 0 \qquad \text{A-13}$$

$$\frac{\Phi_1-\Phi_2}{\Delta z} = 0 \qquad \text{A-14}$$

$$\Phi_1 = \Phi_2 \qquad \text{A-15}$$

In terms of coordinates, equation A-15 can be written as:

$$\Phi_{(i,N_z)=}\Phi_{(i,N_z-1)} \qquad \text{A-16}$$

At the Free Surface

$$\frac{\partial\Phi}{\partial z} - \frac{\omega^2\Phi}{g} = 0 \qquad \text{A-17}$$

$$\frac{\Phi_1-\Phi_2}{\Delta z} - \left(\frac{\Phi_1+\Phi_2}{2}\right)\frac{\omega^2}{g} = 0 \qquad \text{A-18}$$

$$2\Phi_1 - 2\Phi_2 - \frac{\omega^2}{g}\Delta z\Phi_1 - \frac{\omega^2}{g}\Delta z\Phi_2 = 0 \qquad \text{A-19}$$

$$(2 - \frac{\omega^2}{g}\Delta z)\Phi_1 - \left(2 + \frac{\omega^2}{g}\Delta z\right)\Phi_2 = 0 \qquad \text{A-20}$$

$$\Phi_1 = \left(\frac{2+\frac{\omega^2}{g}\Delta z}{2-\frac{\omega^2}{g}\Delta z}\right)\Phi_2 \qquad \text{A-21}$$

In terms of fluid coordinates, equation A-21 can be written as:

$$\Phi_{(i,1)} = \left(\frac{2+\frac{w^2}{g}\Delta z}{2-\frac{w^2}{g}\Delta z}\right)\Phi_{(i,2)} \qquad \text{A-22}$$

Free surface bounded by a trapped air cavity

$$\frac{\partial \Phi}{\partial z} = \frac{\partial \eta_c}{\partial t} \qquad \text{A-23}$$

$$\frac{\Phi_1 - \Phi_2}{\Delta z} = \frac{\partial \eta_c}{\partial t} \qquad \text{A-24}$$

$$\Phi_1 - \Phi_2 = \frac{\partial \eta_c}{\partial t}\Delta z \qquad \text{A-25}$$

$$\Phi_1 = \Phi_2 + \frac{\partial \eta_c}{\partial t}\Delta z \qquad \text{A-26}$$

In term of fluid domain coordinates, equation A-26 can be written as:

$$\Phi_{i,1} = \Phi(i,2) + \Delta z\left(\frac{\partial \eta_c}{\partial t}\right)_{i,1} \qquad \text{A-27}$$

B. CALIBRATION OF EFFECTIVE THICKNESS OF WATER MASS

As discussed in Chapter 3, k_t was calibrated by comparing the high frequency oscillatory force from experimental data with modeled data computed using the trapped air model with values of k_t ranging from 0.1 inches to total water depth, h. Results from other experiment test cases are shown in this Appendix:

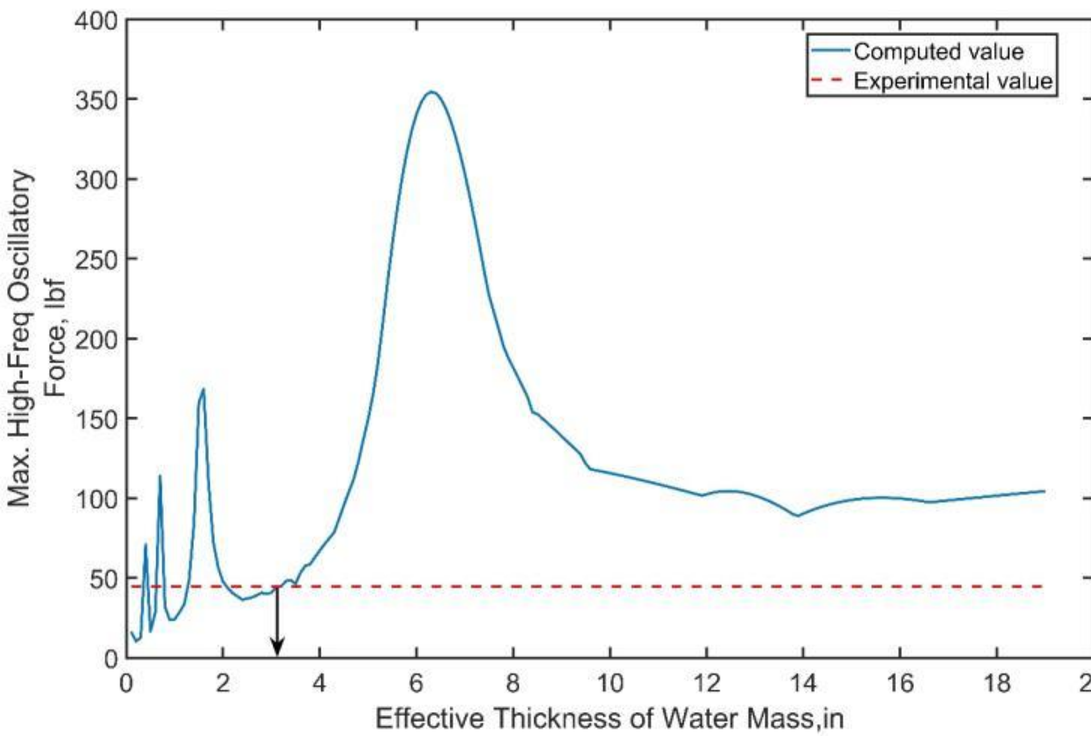

Figure B-1. Effective thickness of water mass Versus Maximum high-frequency oscillatory force for deck configuration BSXX011

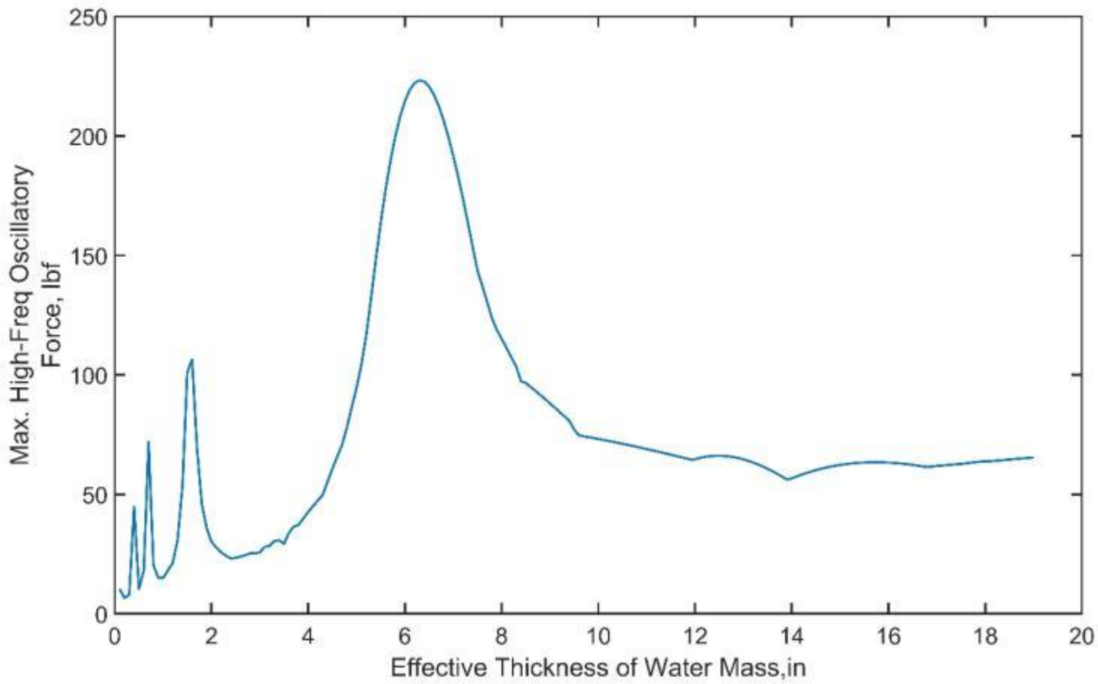

Figure B-2. Effective thickness of water mass Versus Maximum high-frequency oscillatory force for deck configuration BSXX012

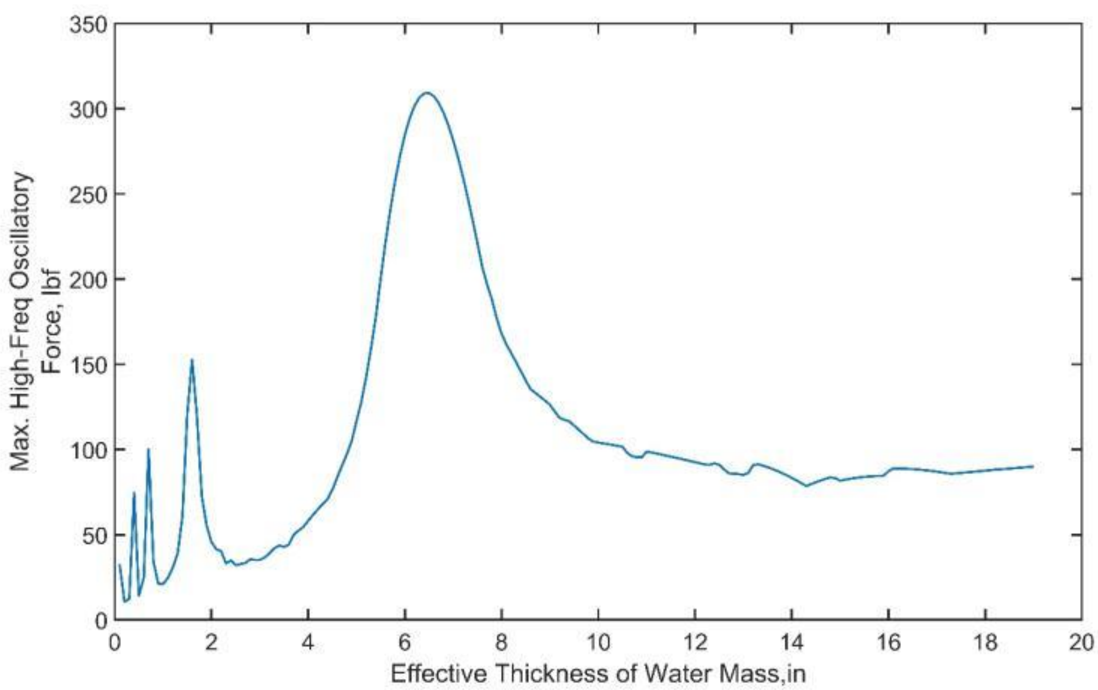

Figure B-3. Effective thickness of water mass Versus Maximum high-frequency oscillatory force for deck configuration BSXX013

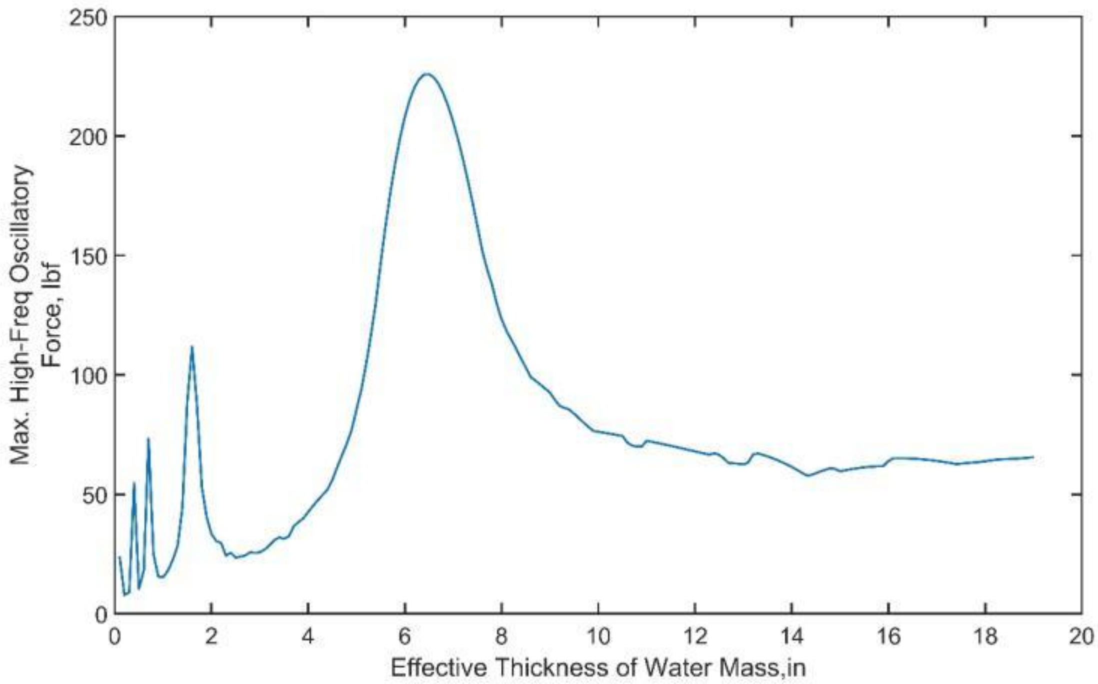

Figure B-4. Effective thickness of water mass Versus Maximum high-frequency oscillatory force for deck configuration BSXX014

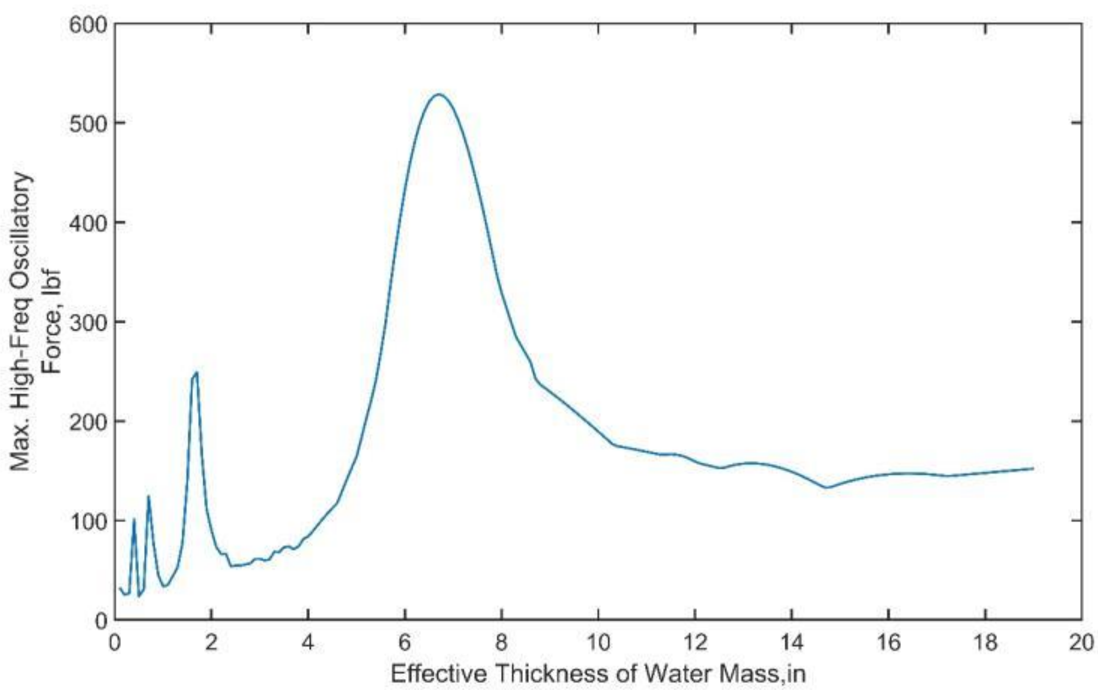

Figure B-5. Effective thickness of water mass Versus Maximum high-frequency oscillatory force for deck configuration BSXX015

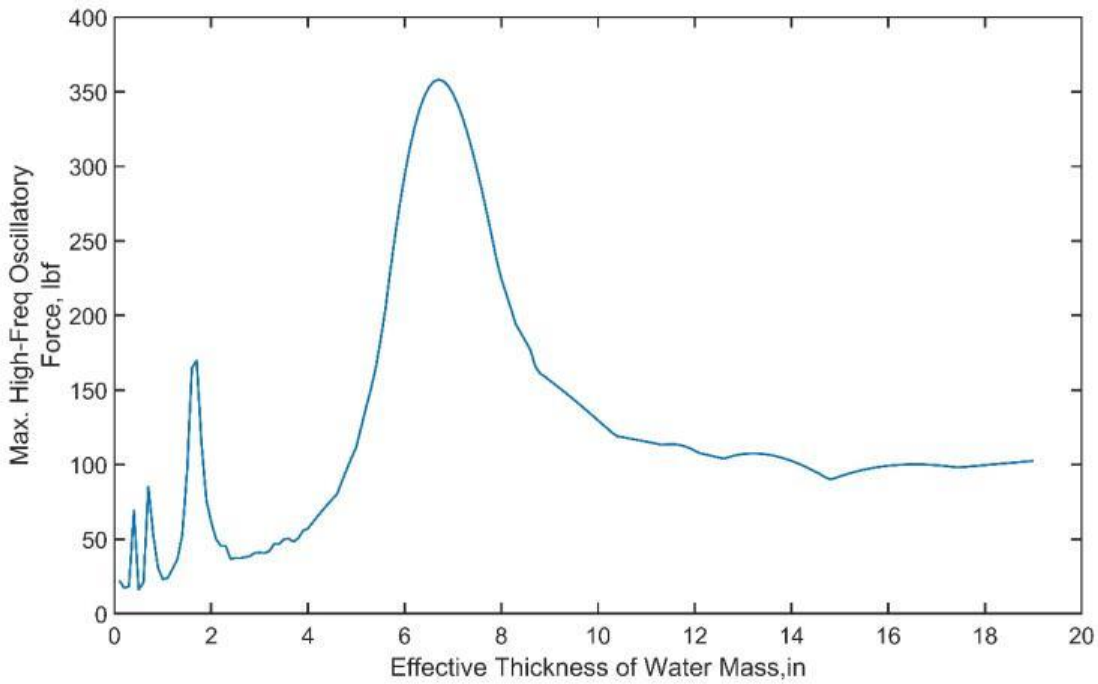

Figure B-6. Effective thickness of water mass Versus Maximum high-frequency oscillatory force for deck configuration BSXX016

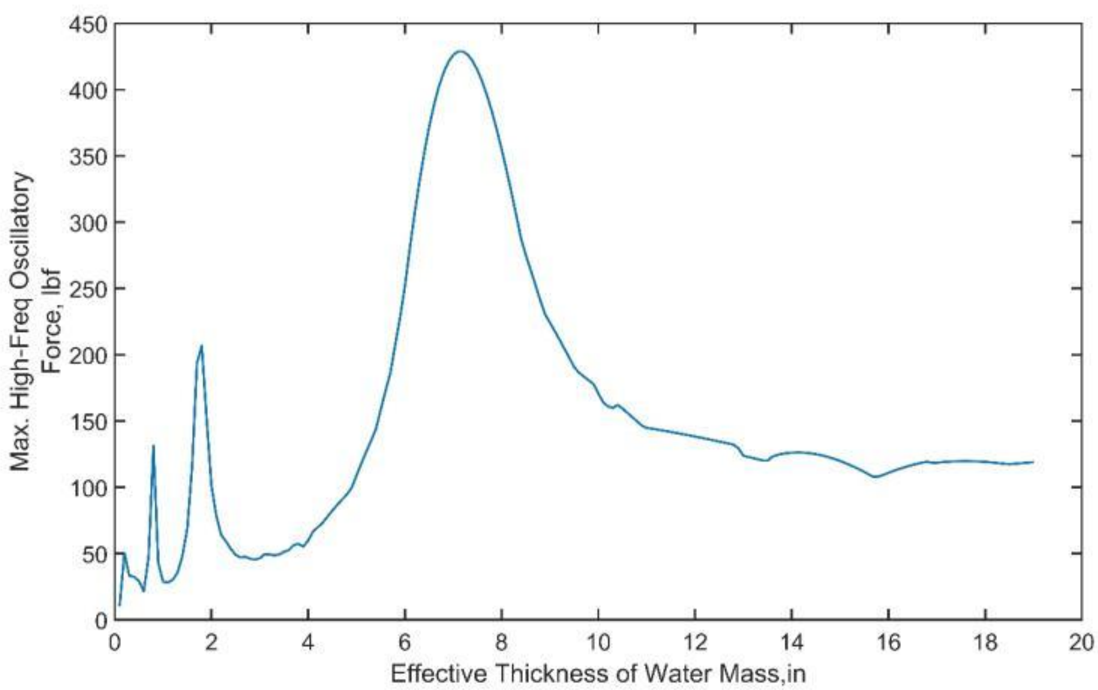

Figure B-7. Effective thickness of water mass Versus Maximum high-frequency oscillatory force for deck configuration BSXX017

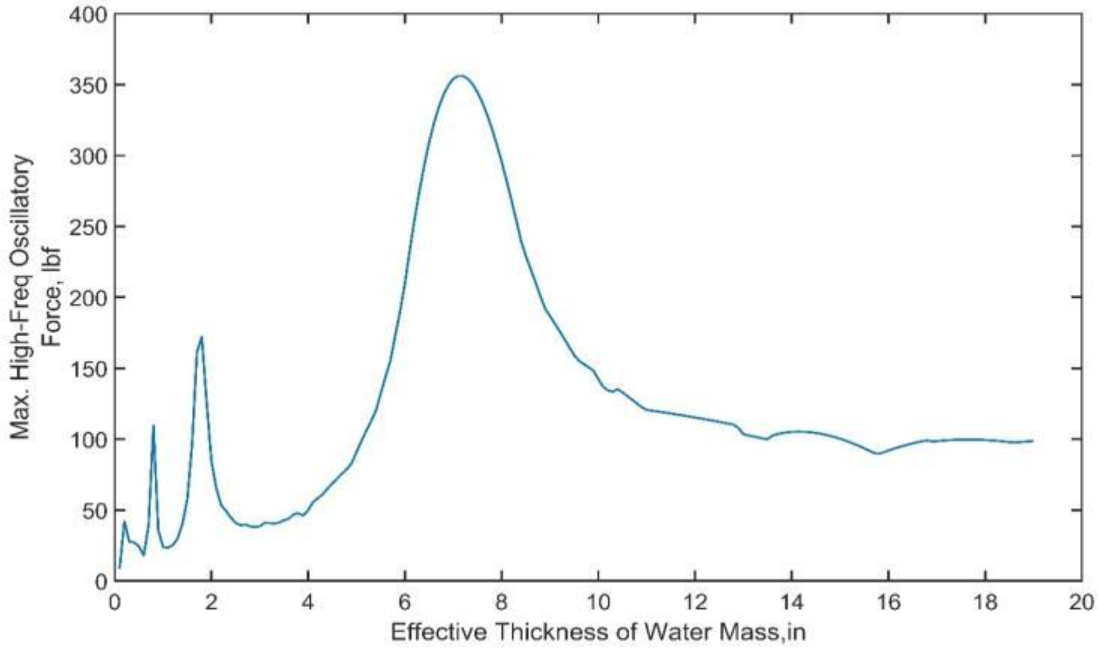

Figure B-8. Effective thickness of water mass Versus Maximum high-frequency oscillatory force for deck configuration BSXX018

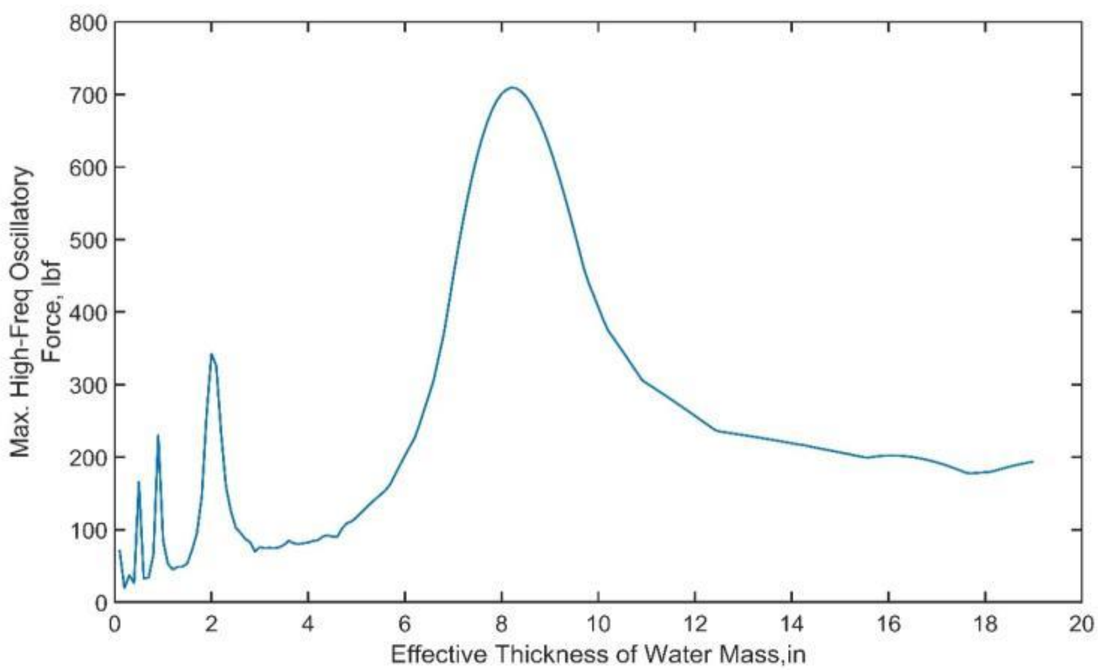

Figure B-9. Effective thickness of water mass Versus Maximum high-frequency oscillatory force for deck configuration BSXX019

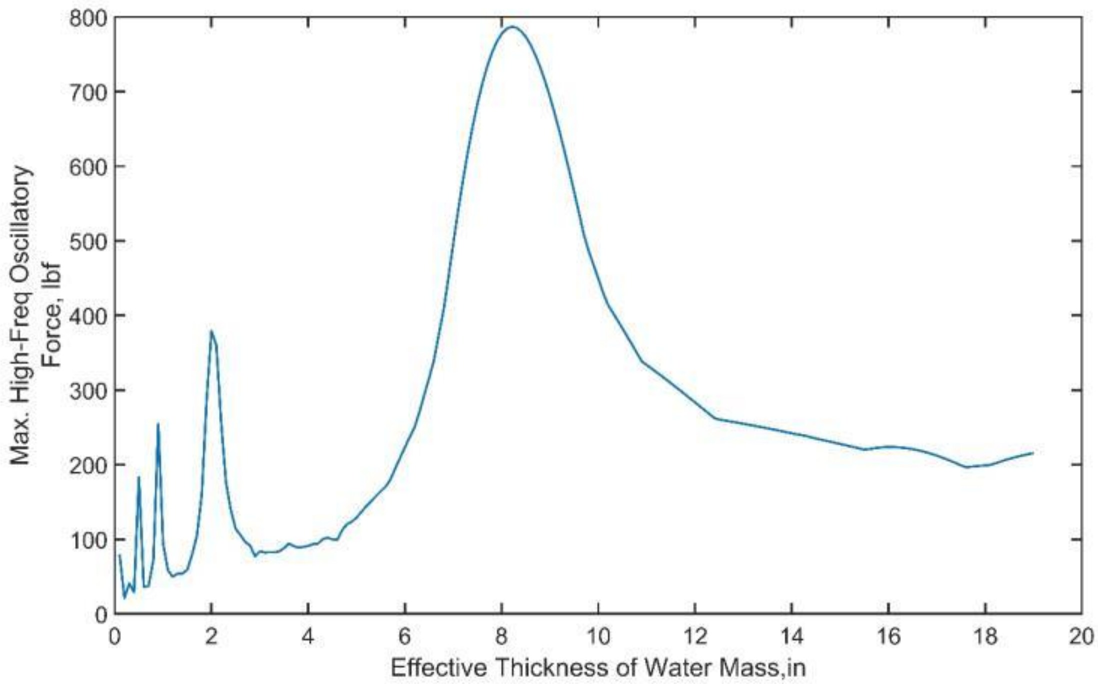

Figure B-10. Effective thickness of water mass Versus Maximum high-frequency oscillatory force for deck configuration BSXX020

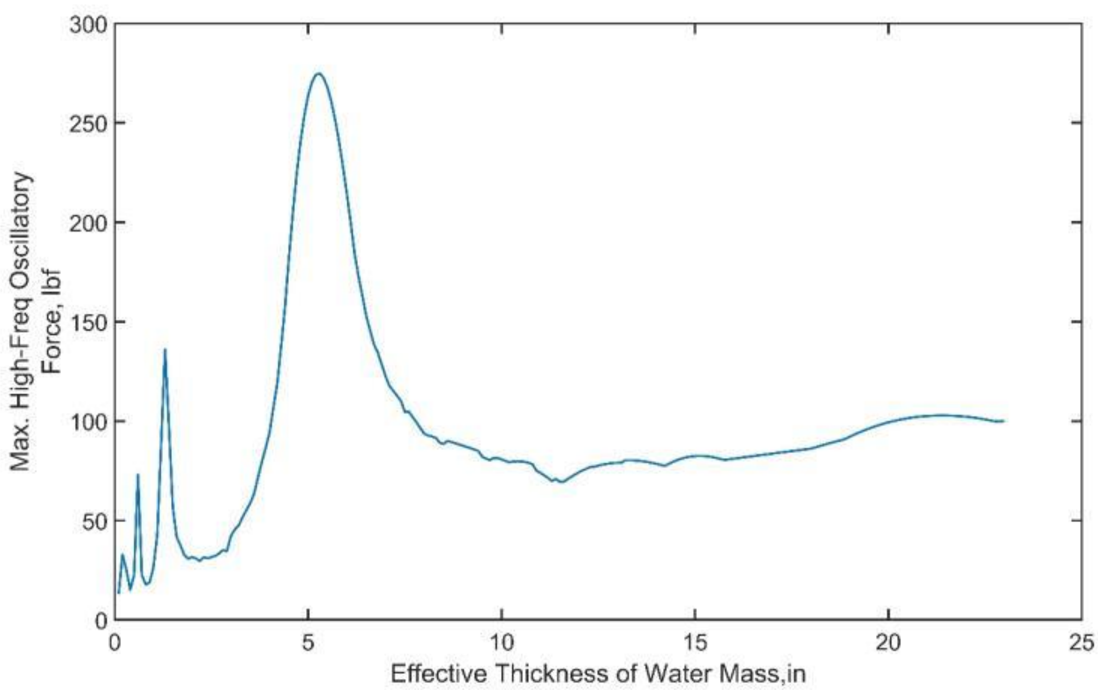

Figure B-11. Effective thickness of water mass Versus Maximum high-frequency oscillatory force for deck configuration BSXX051

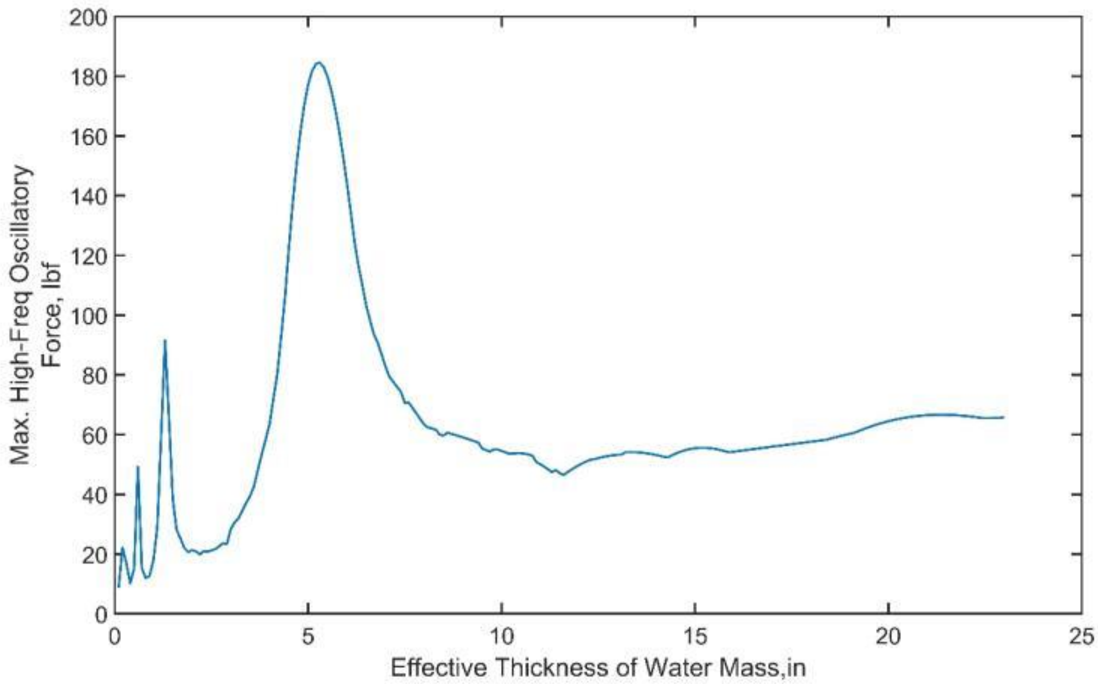

Figure B-12. Effective thickness of water mass Versus Maximum high-frequency oscillatory force for deck configuration BSXX052

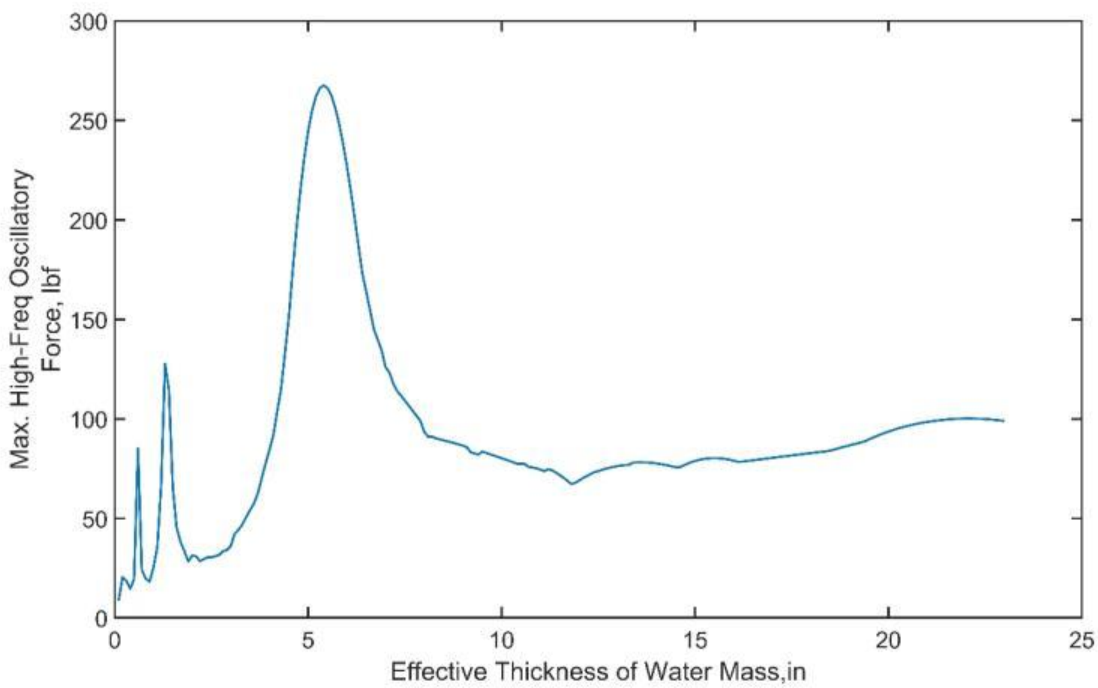

Figure B-13. Effective thickness of water mass Versus Maximum high-frequency oscillatory force for deck configuration BSXX053

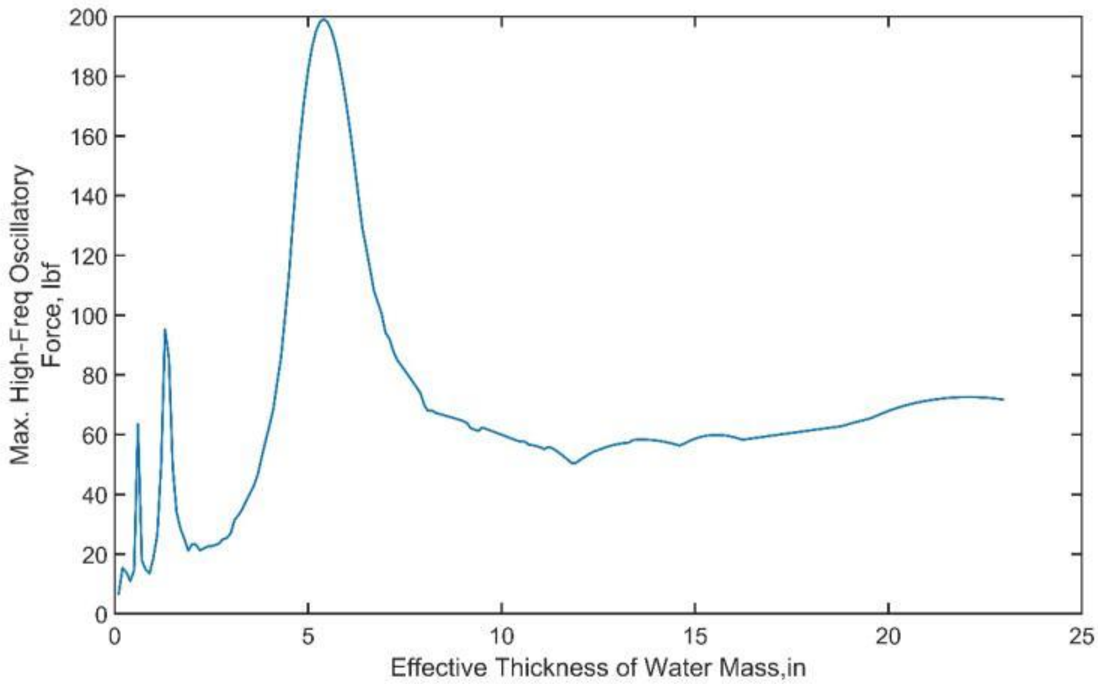

Figure B-14. Effective thickness of water mass Versus Maximum high-frequency oscillatory force for deck configuration BSXX054

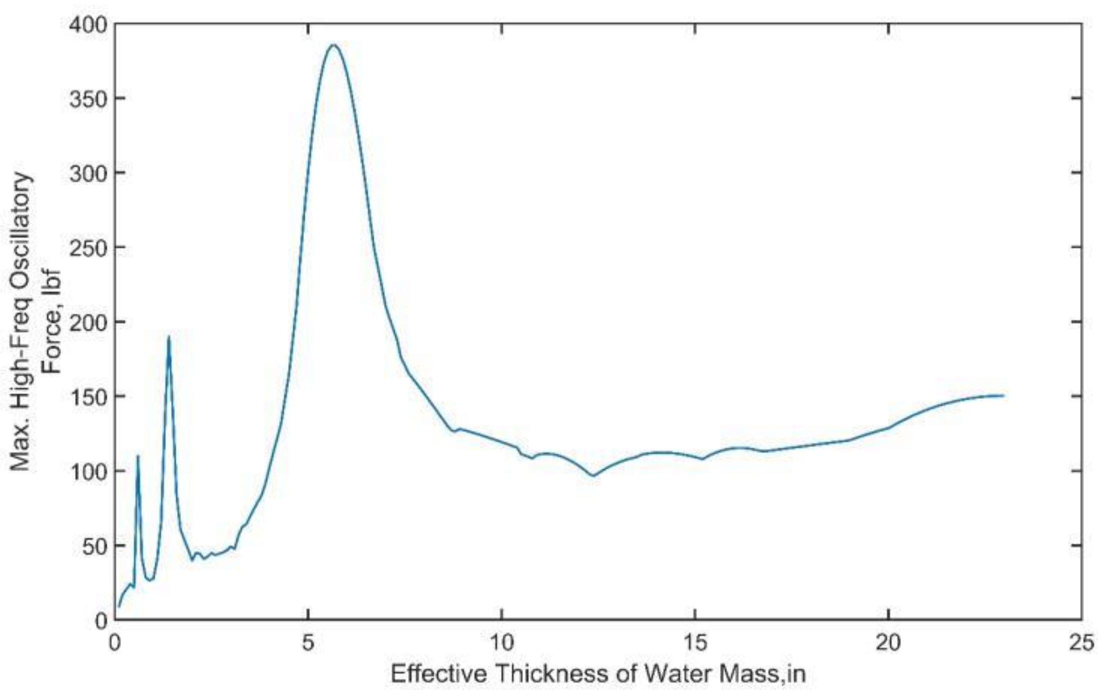

Figure B-15. Effective thickness of water mass Versus Maximum high-frequency oscillatory force for deck configuration BSXX055

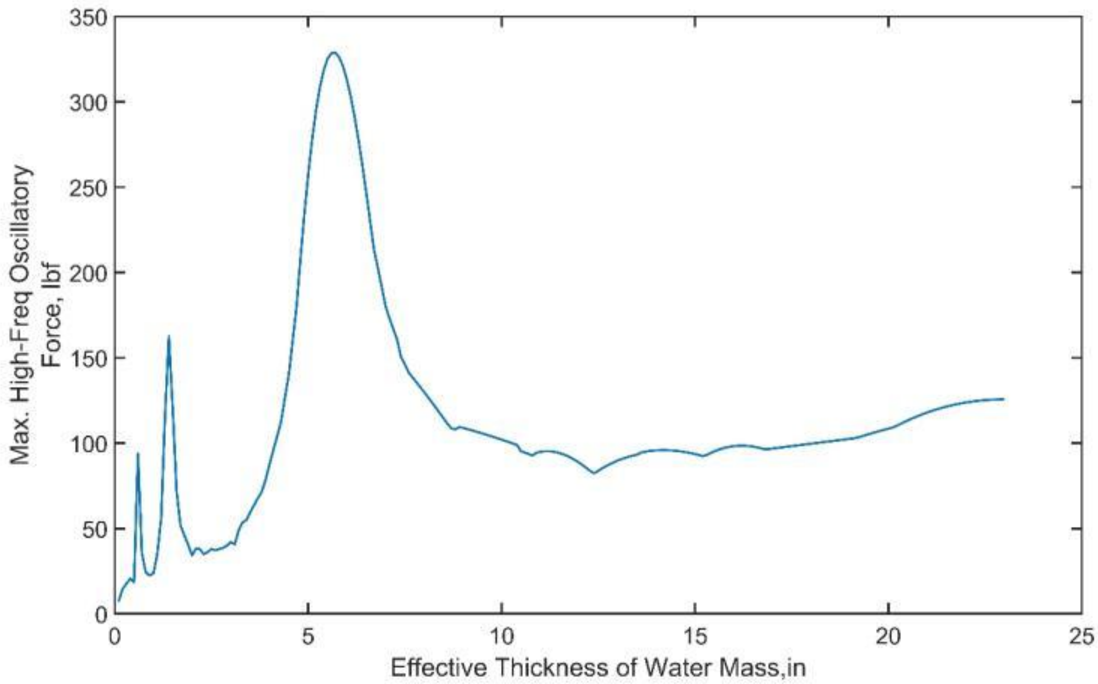

Figure B-16. Effective thickness of water mass Versus Maximum high-frequency oscillatory force for deck configuration BSXX056

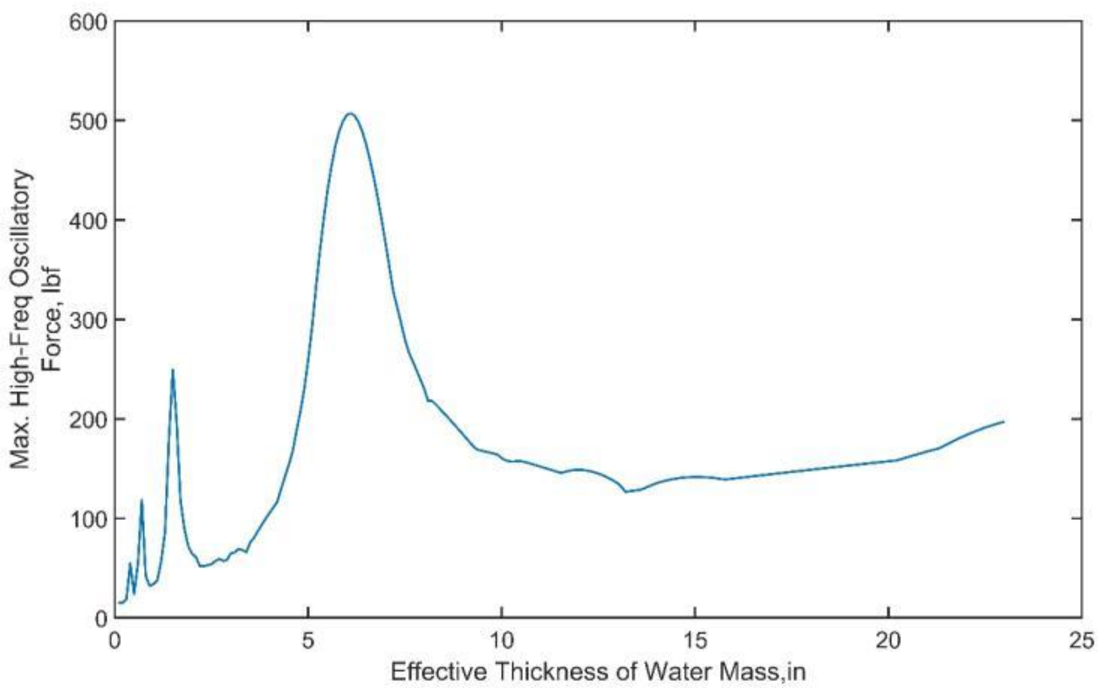

Figure B-17. Effective thickness of water mass Versus Maximum high-frequency oscillatory force for deck configuration BSXX057

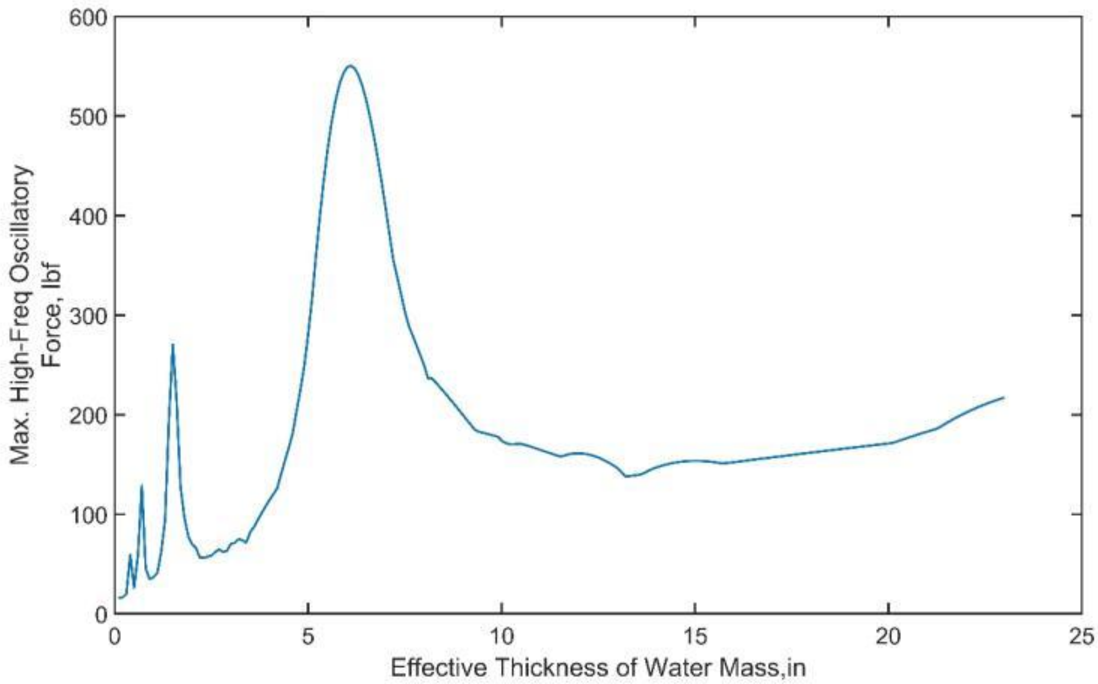

Figure B-18. Effective thickness of water mass Versus Maximum high-frequency oscillatory force for deck configuration BSXX058

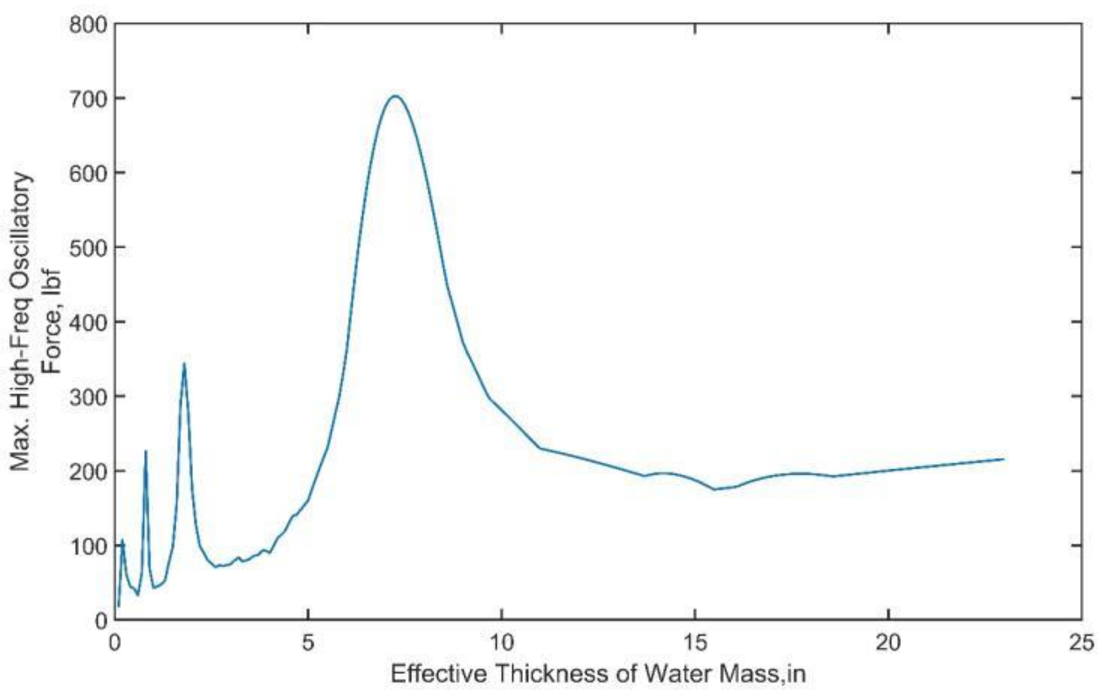

Figure B-19. Effective thickness of water mass Versus Maximum high-frequency oscillatory force for deck configuration BSXX059

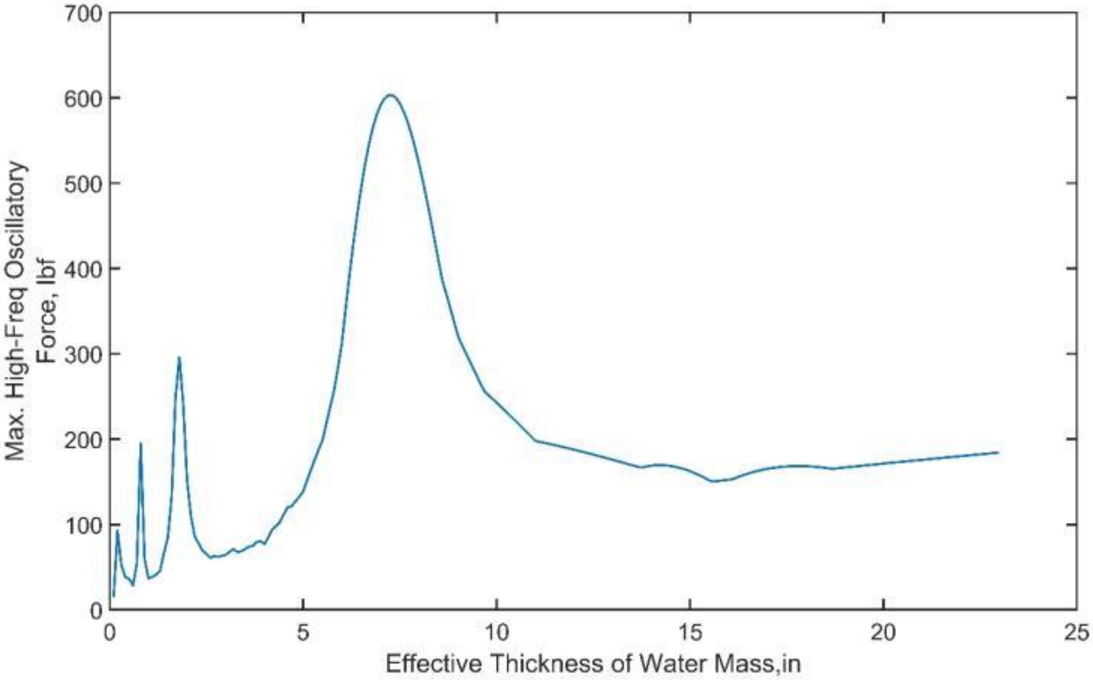

Figure B-20. Effective thickness of water mass Versus Maximum high-frequency oscillatory force for deck configuration BSXX060

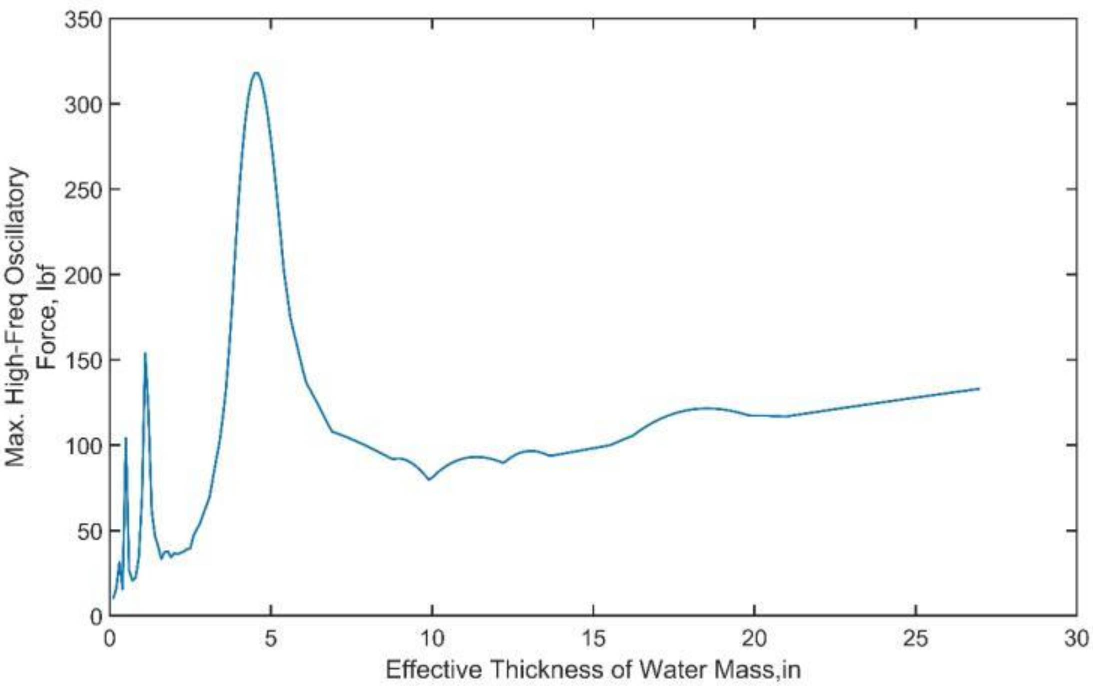

Figure B-21. Effective thickness of water mass Versus Maximum high-frequency oscillatory force for deck configuration BSXX091

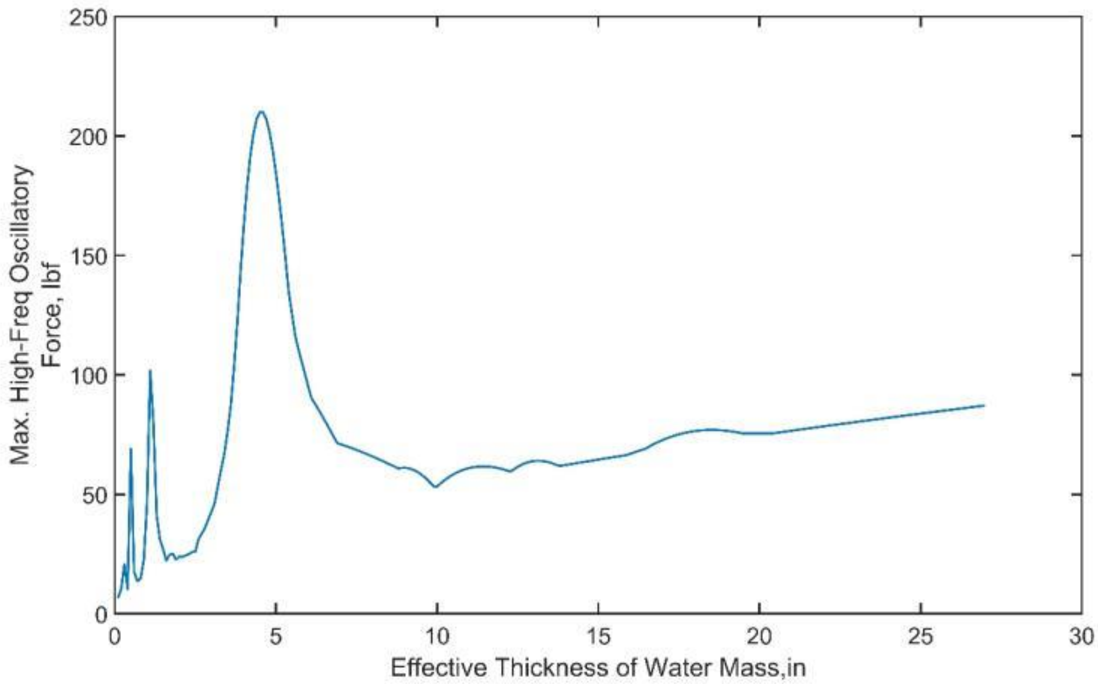

Figure B-22. Effective thickness of water mass Versus Maximum high-frequency oscillatory force for deck configuration BSXX092

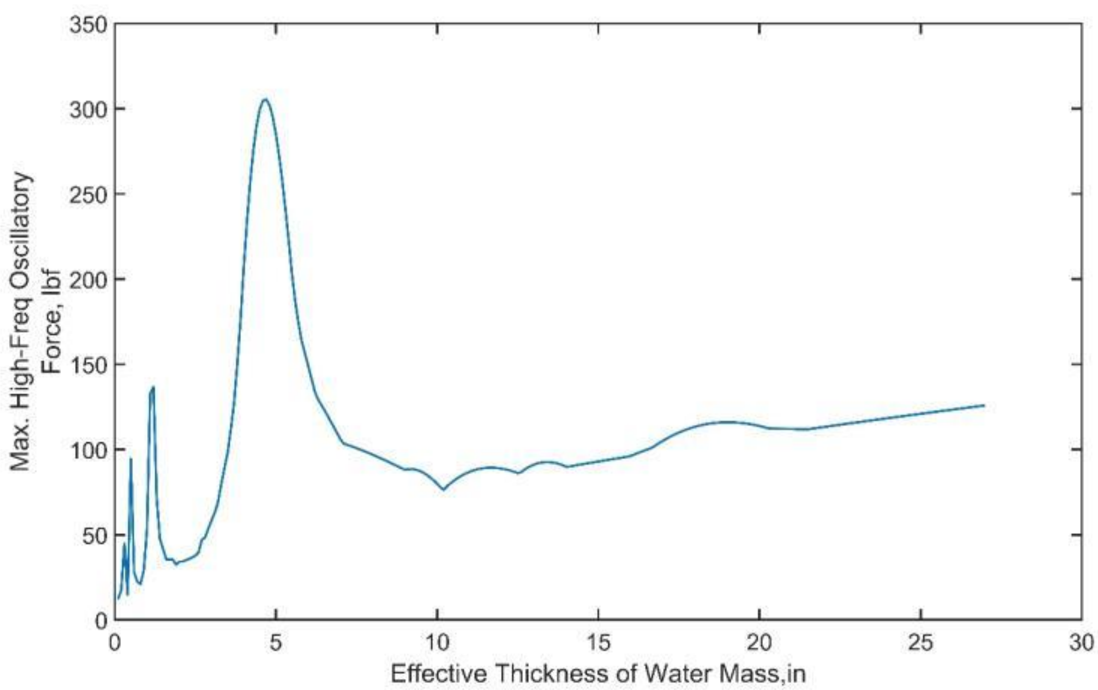

Figure B-23. Effective thickness of water mass Versus Maximum high-frequency oscillatory force for deck configuration BSXX093

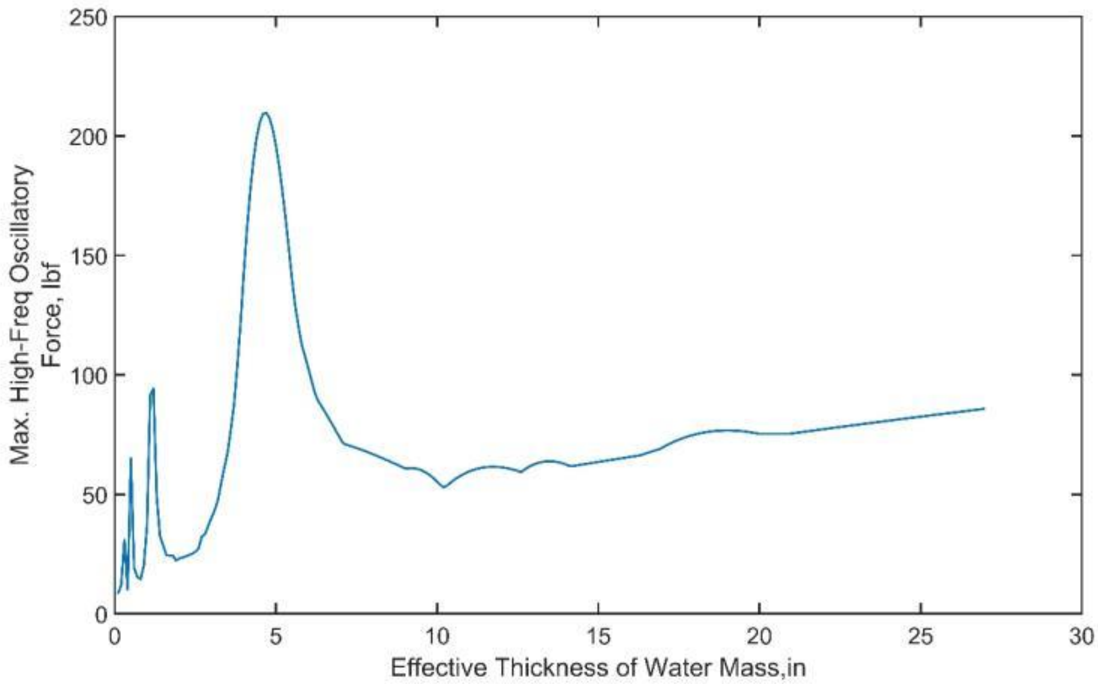

Figure B-24. Effective thickness of water mass Versus Maximum high-frequency oscillatory force for deck configuration BSXX094

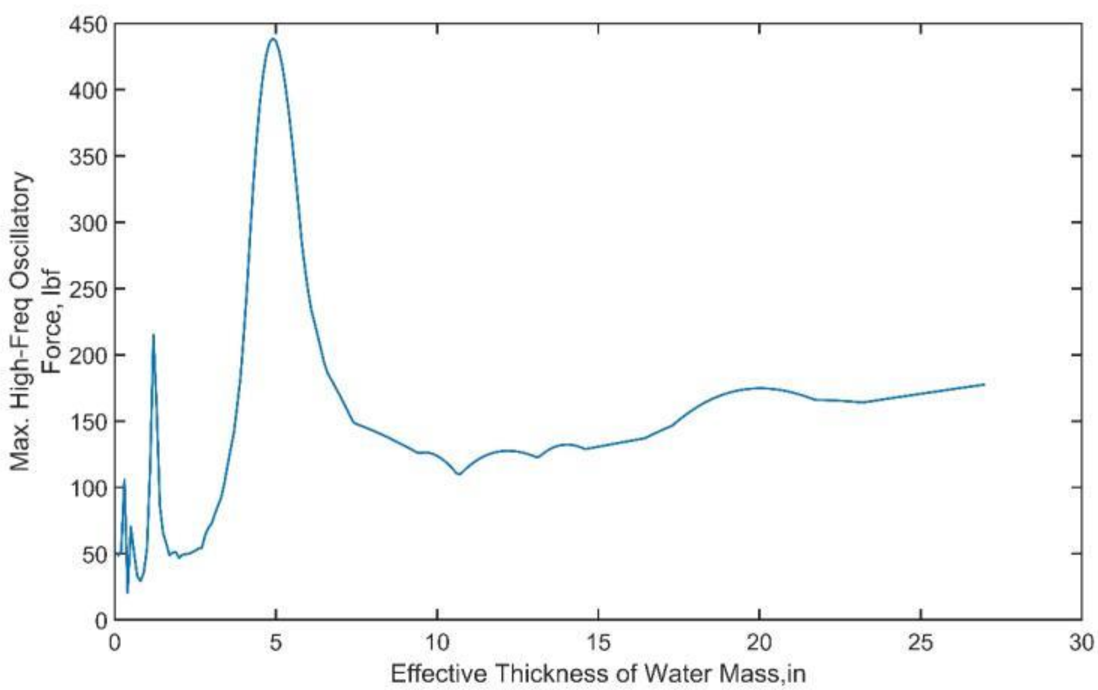

Figure B-25. Effective thickness of water mass Versus Maximum high-frequency oscillatory force for deck configuration BSXX095

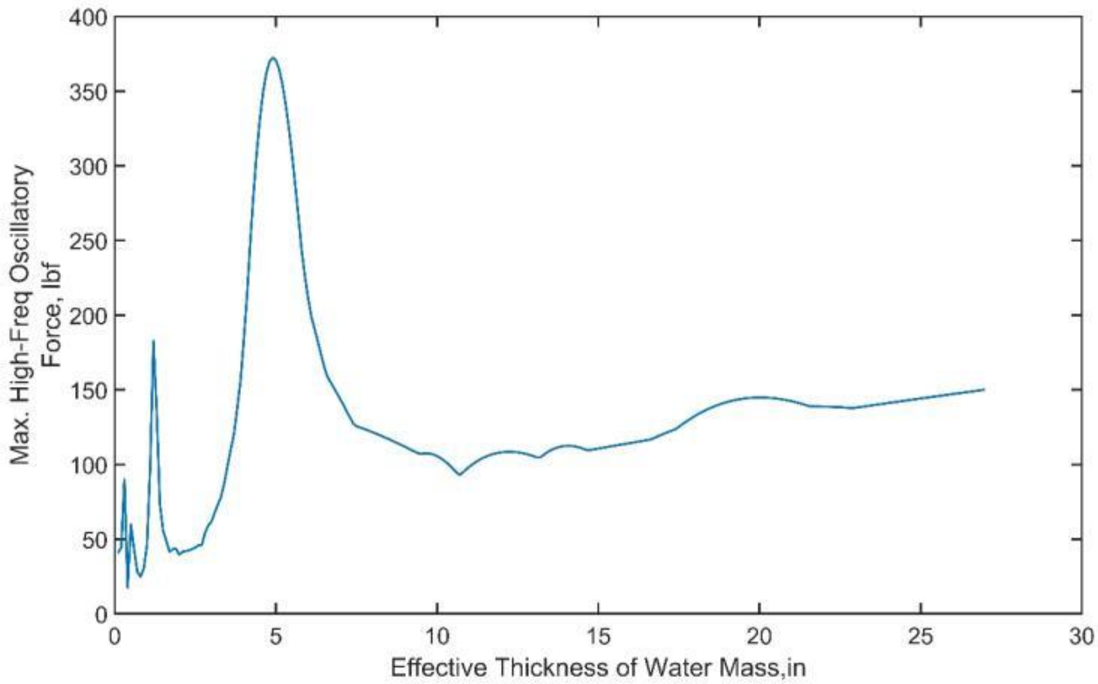

Figure B-26. Effective thickness of water mass Versus Maximum high-frequency oscillatory force for deck configuration BSXX096

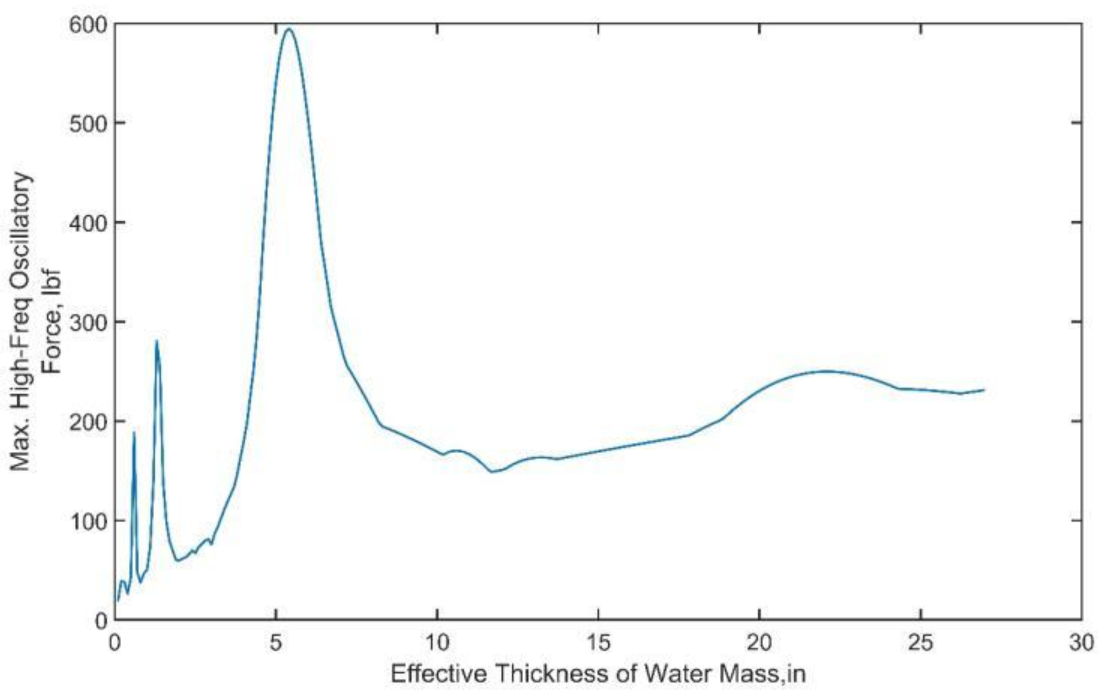

Figure B-27. Effective thickness of water mass Versus Maximum high-frequency oscillatory force for deck configuration BSXX097

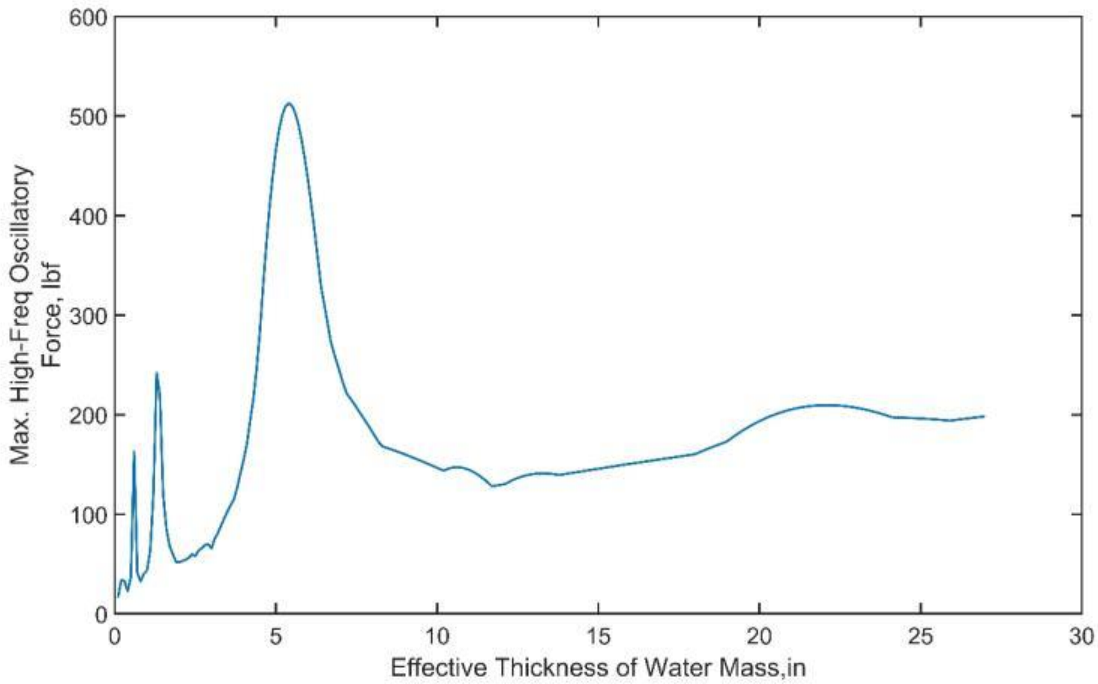

Figure B-28. Effective thickness of water mass Versus Maximum high-frequency oscillatory force for deck configuration BSXX098

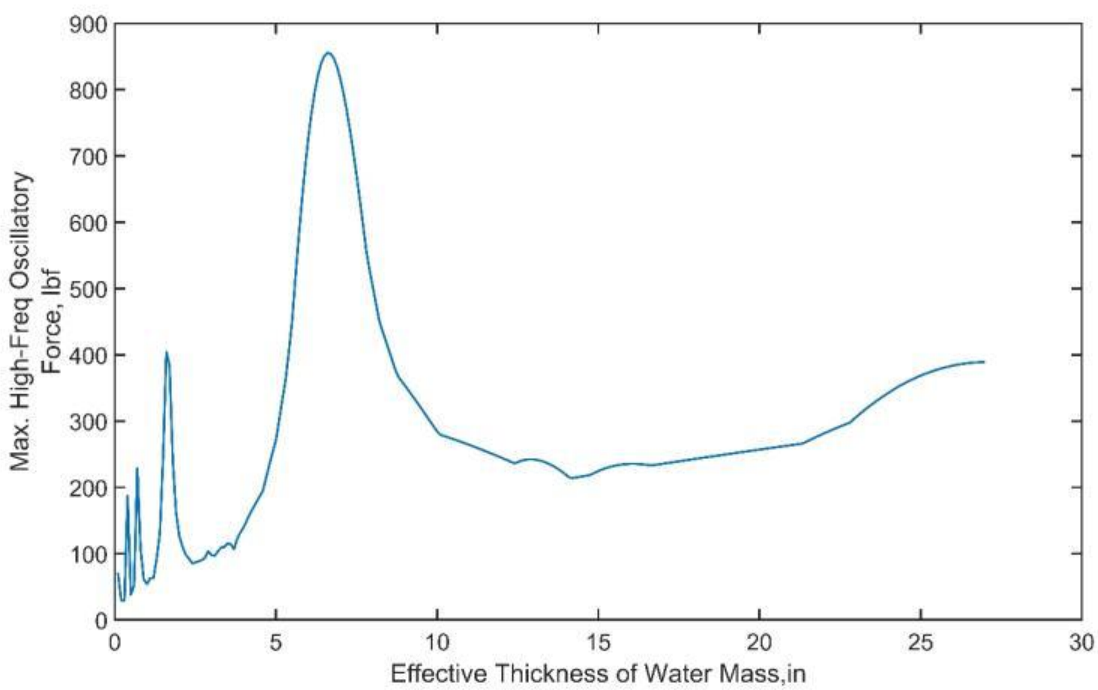

Figure B-29. Effective thickness of water mass Versus Maximum high-frequency oscillatory force for deck configuration BSXX099

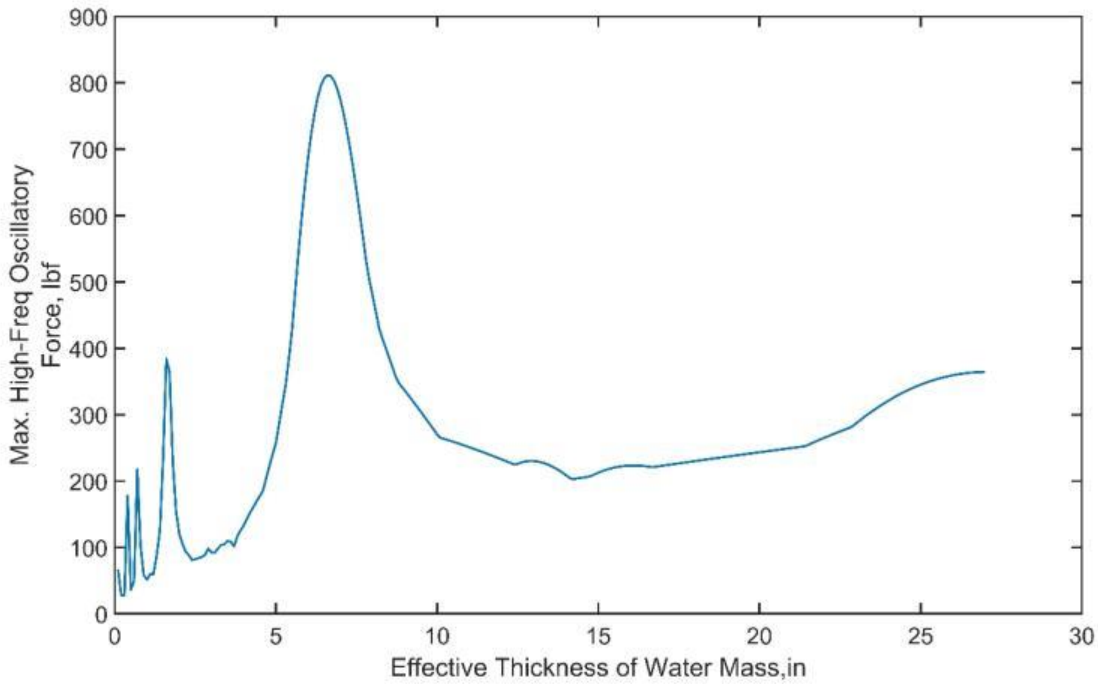

Figure B-30. Effective thickness of water mass Versus Maximum high-frequency oscillatory force for deck configuration BSXX100

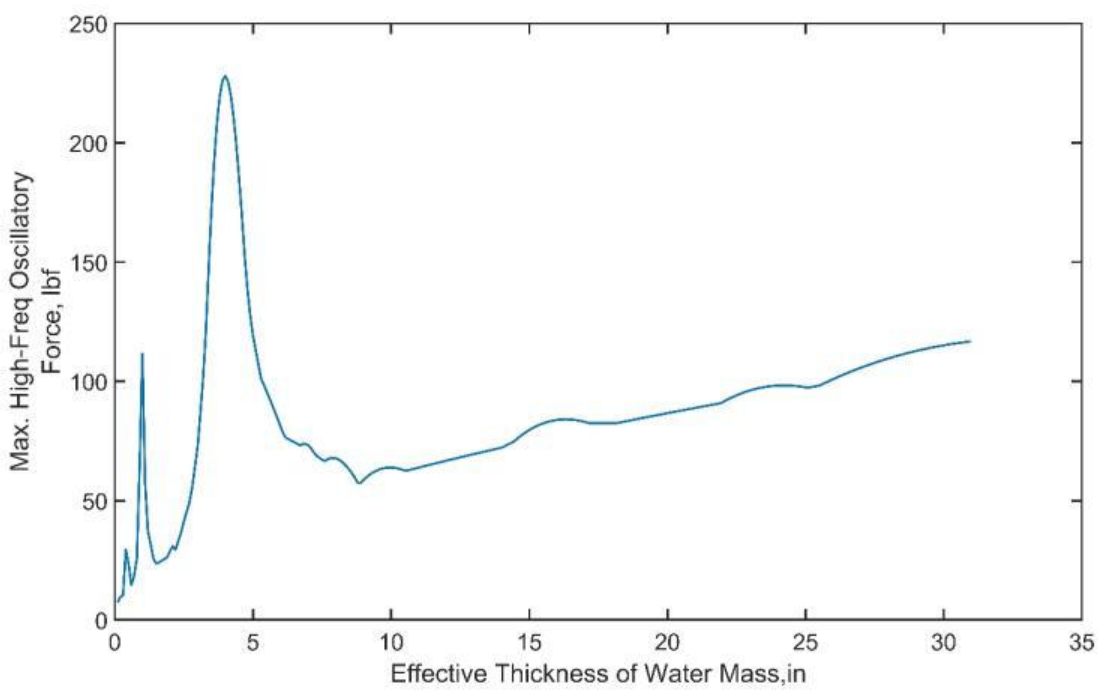

Figure B-31. Effective thickness of water mass Versus Maximum high-frequency oscillatory force for deck configuration BSXX131

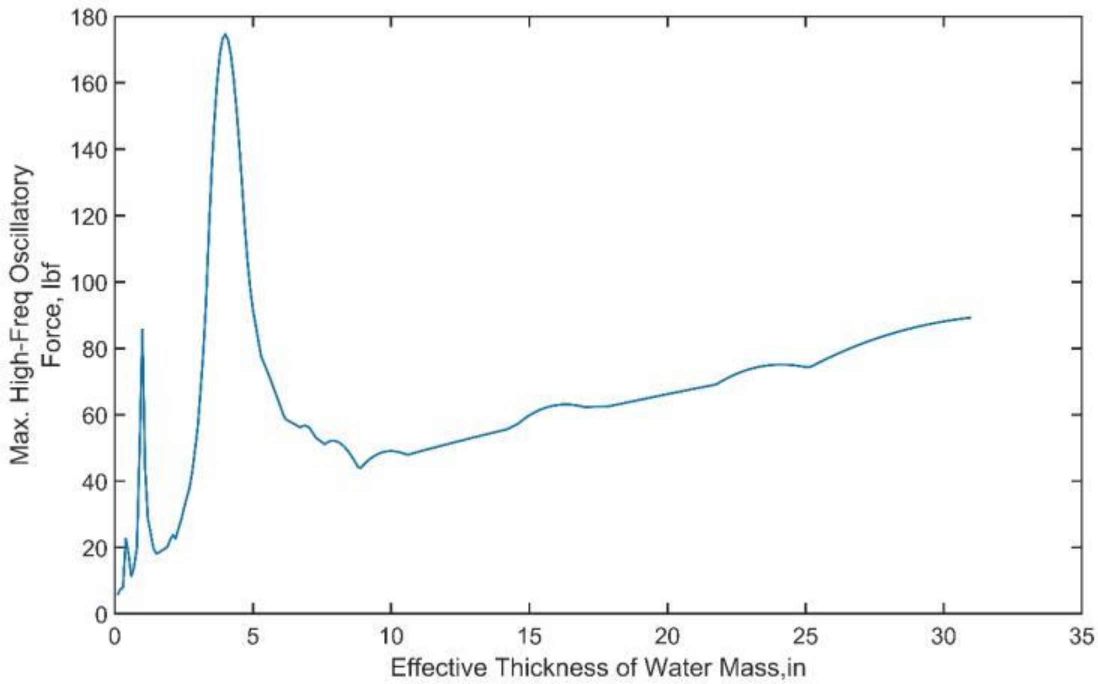

Figure B-32. Effective thickness of water mass Versus Maximum high-frequency oscillatory force for deck configuration BSXX132

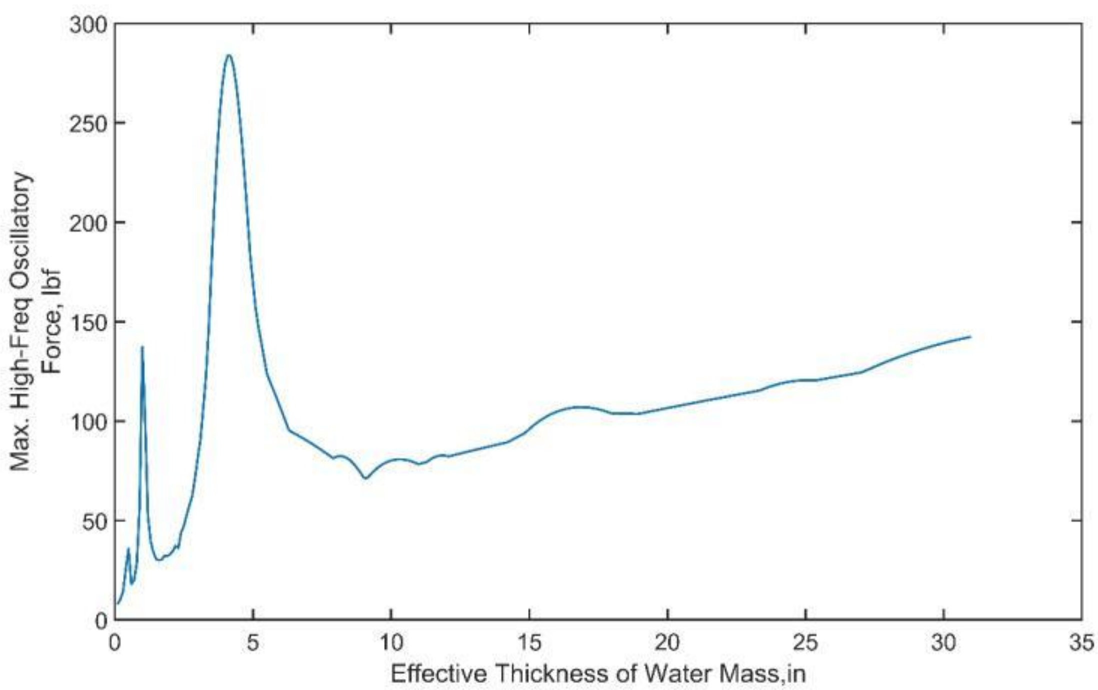

Figure B-33. Effective thickness of water mass Versus Maximum high-frequency oscillatory force for deck configuration BSXX133

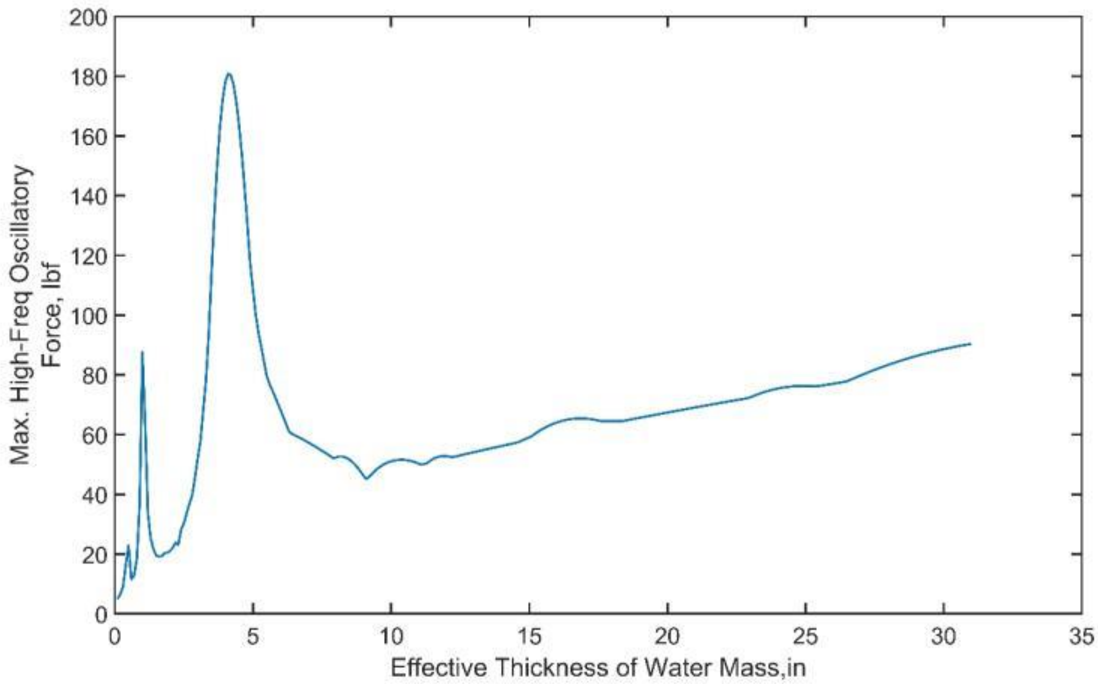

Figure B-34. Effective thickness of water mass Versus Maximum high-frequency oscillatory force for deck configuration BSXX134

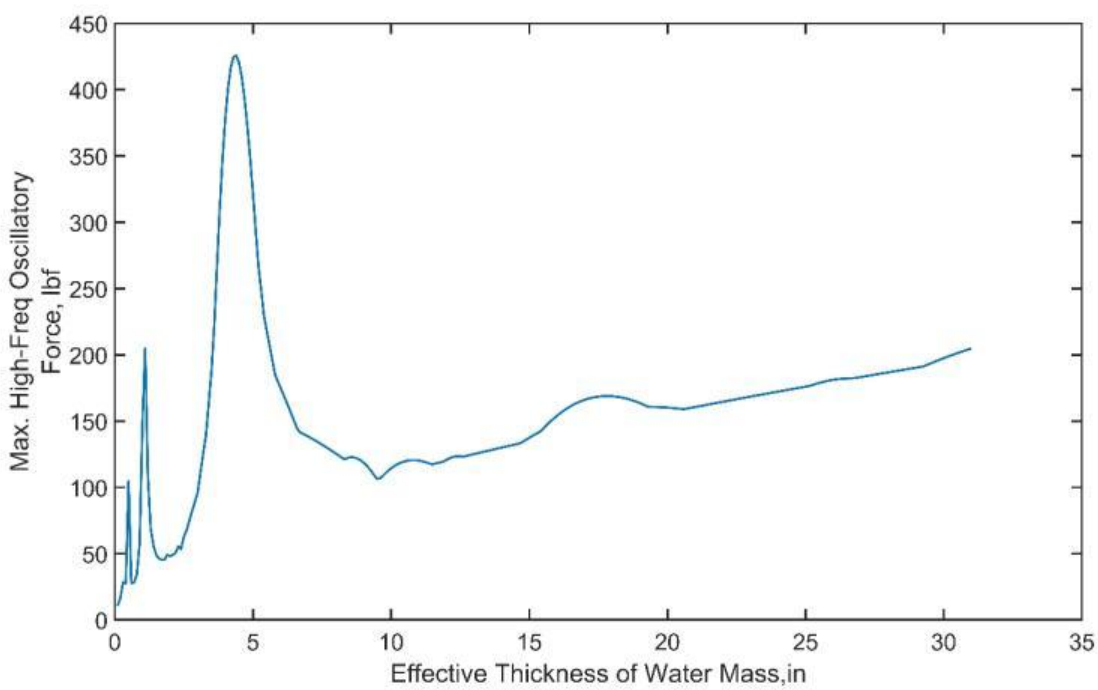

Figure B-35. Effective thickness of water mass Versus Maximum high-frequency oscillatory force for deck configuration BSXX135

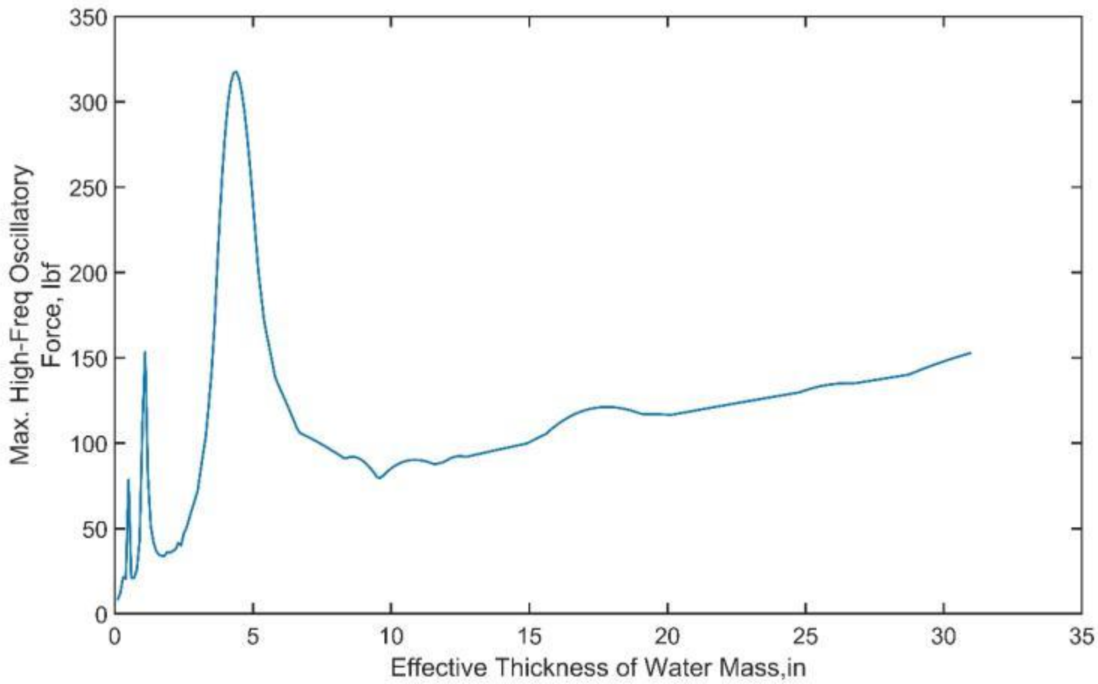

Figure B-36. Effective thickness of water mass Versus Maximum high-frequency oscillatory force for deck configuration BSXX136

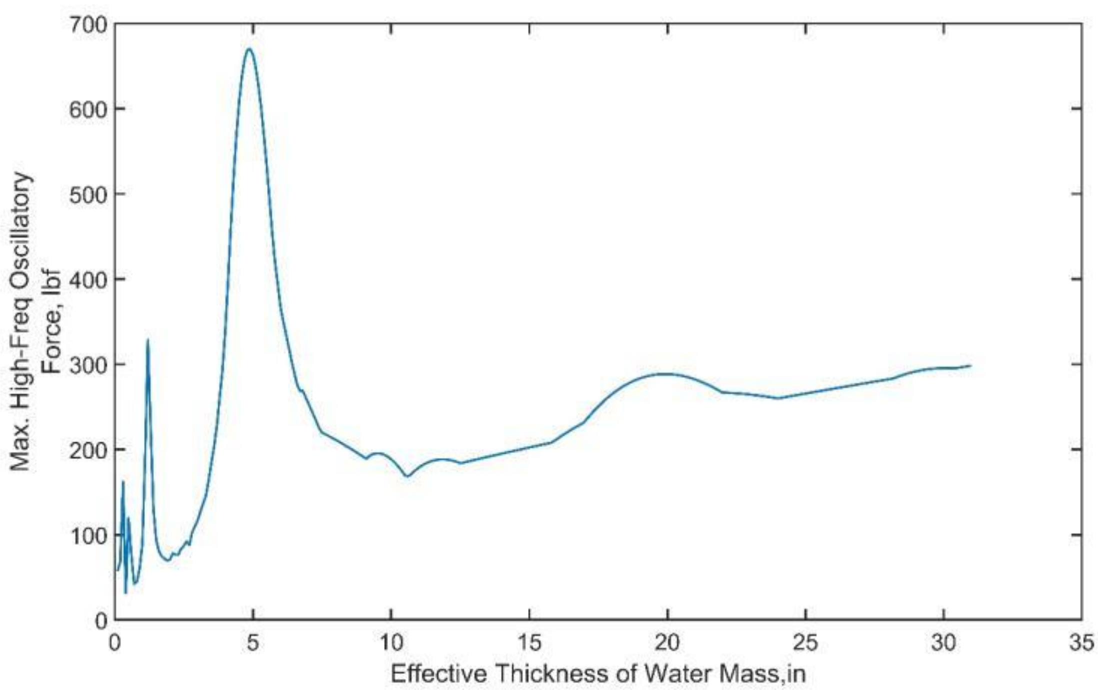

Figure B-37. Effective thickness of water mass Versus Maximum high-frequency oscillatory force for deck configuration BSXX137

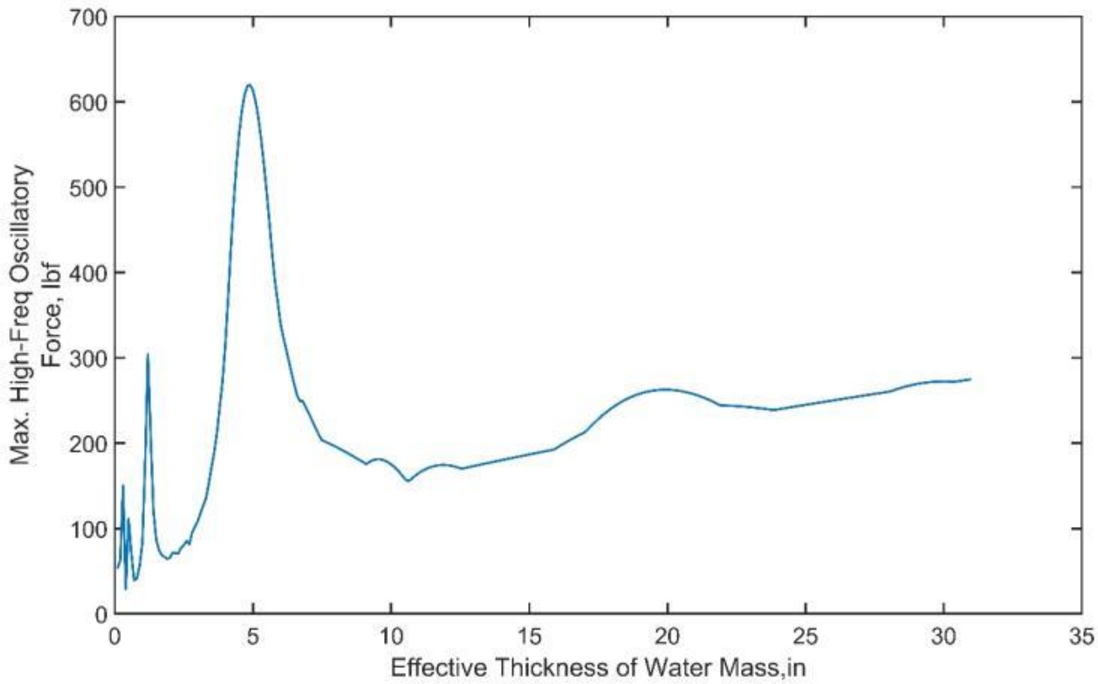

Figure B-38. Effective thickness of water mass Versus Maximum high-frequency oscillatory force for deck configuration BSXX138

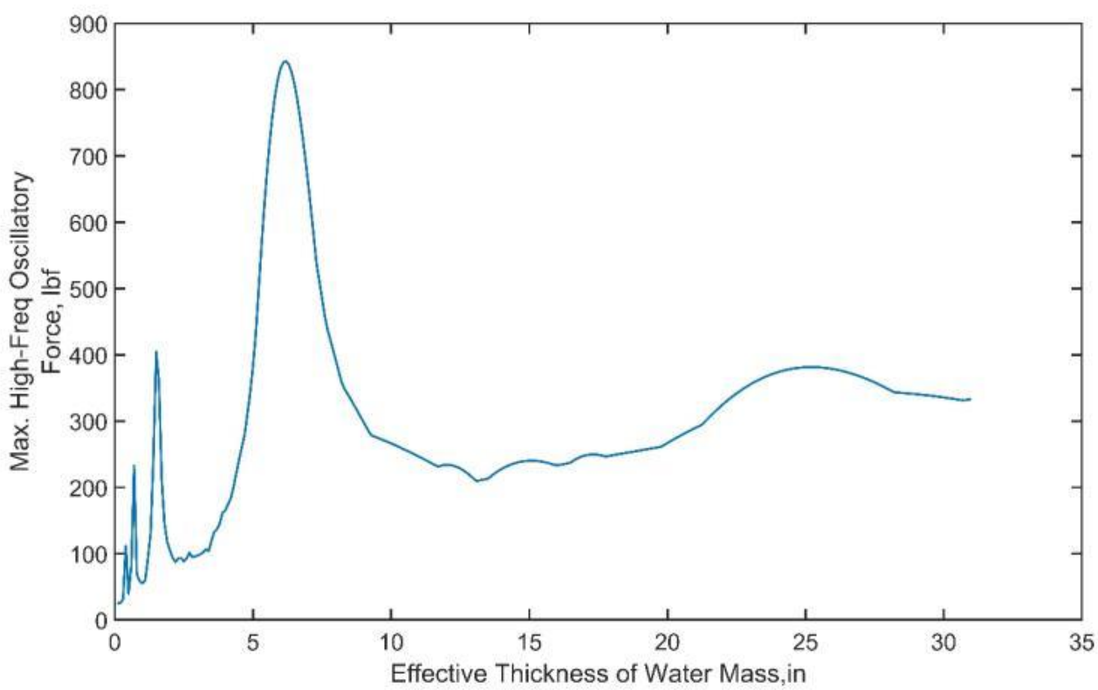

Figure B-39. Effective thickness of water mass Versus Maximum high-frequency oscillatory force for deck configuration BSXX13

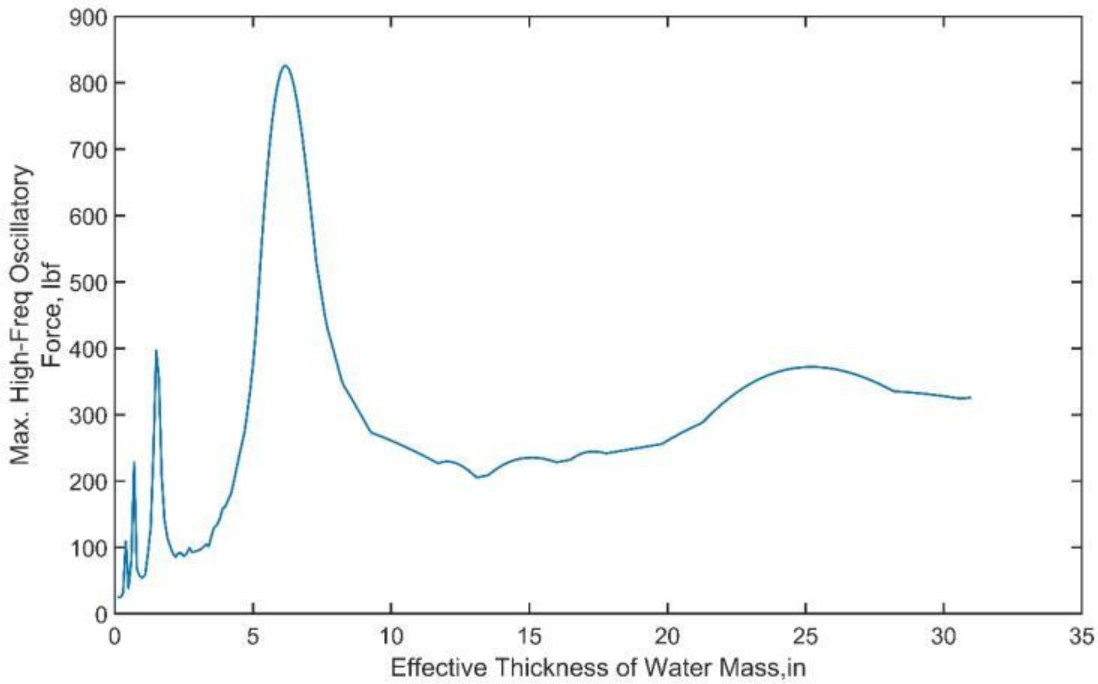

Figure B-40. Effective thickness of water mass Versus Maximum high-frequency oscillatory force for deck configuration BSXX140

C FORCE TIME HISTORY

Full time-history results of forcing on the bridge decks is presented below for the case where k_t was calibrated. In addition, the case where trapped air was not considered (i.e. the hypothetical case with “vented” deck diaphragms) is subsequently presented.

C. 1. WITH TRAPPED AIR

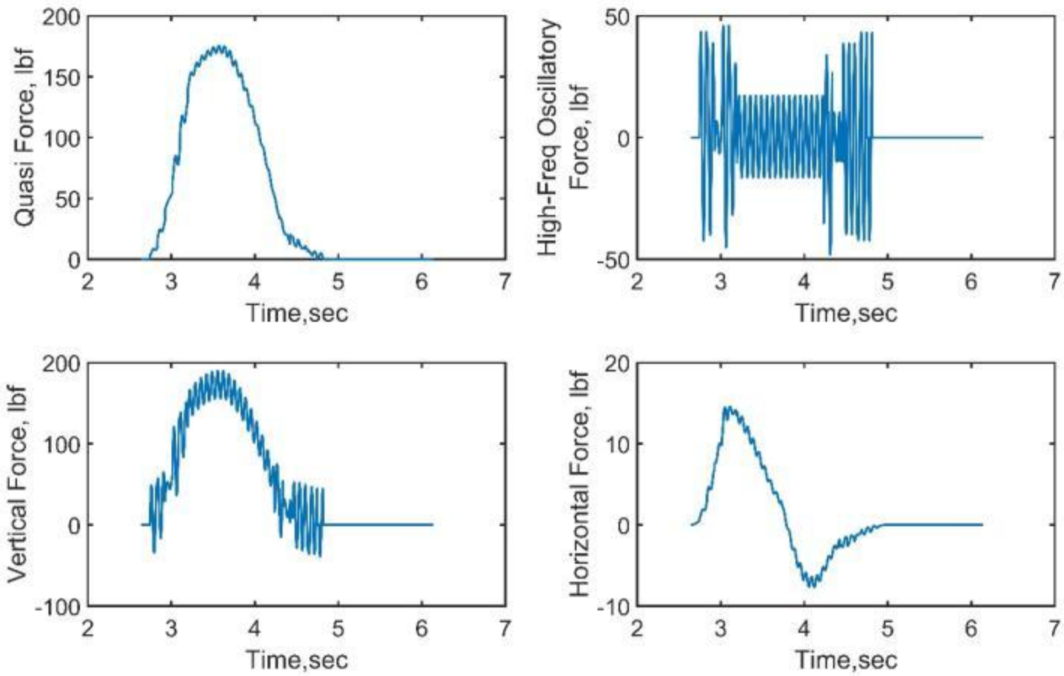

Figure C.1- 1. Force Time-Histories for Bridge Configuration BSXX011

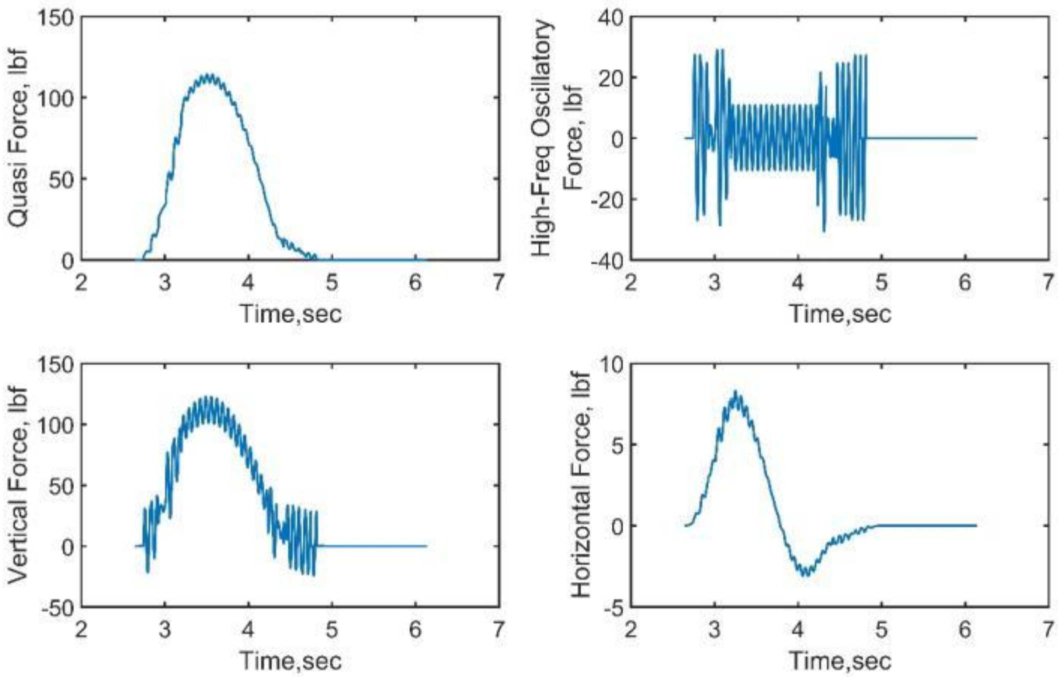

Figure C.1-2. Force Time-Histories for Bridge Configuration BSXX012

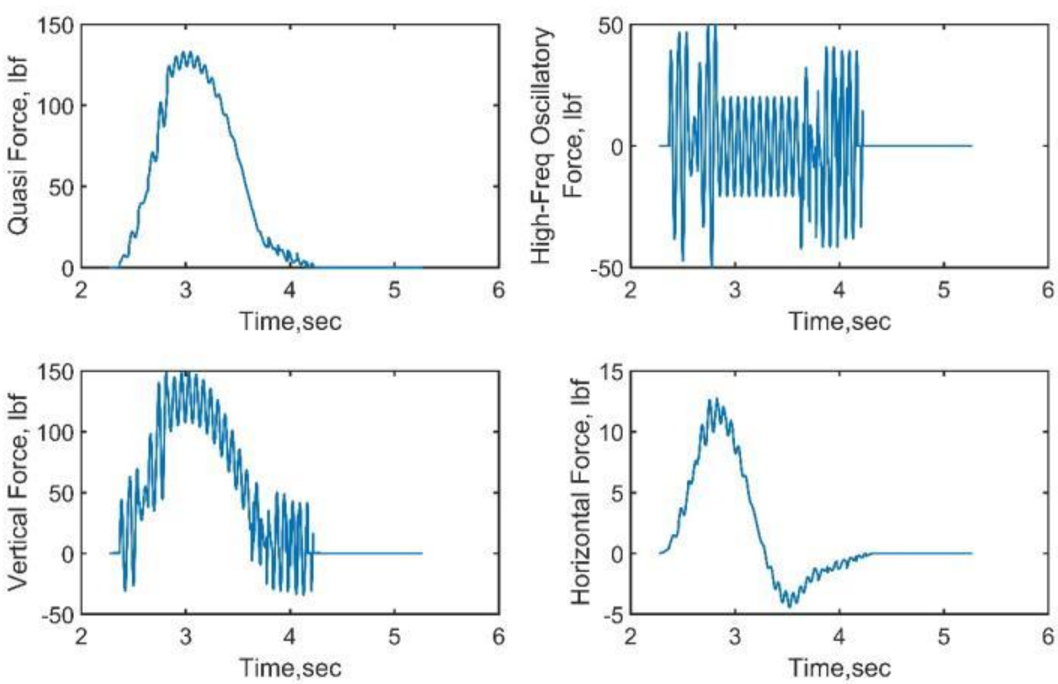

Figure C.1-3. Force Time-Histories for Bridge Configuration BSXX013

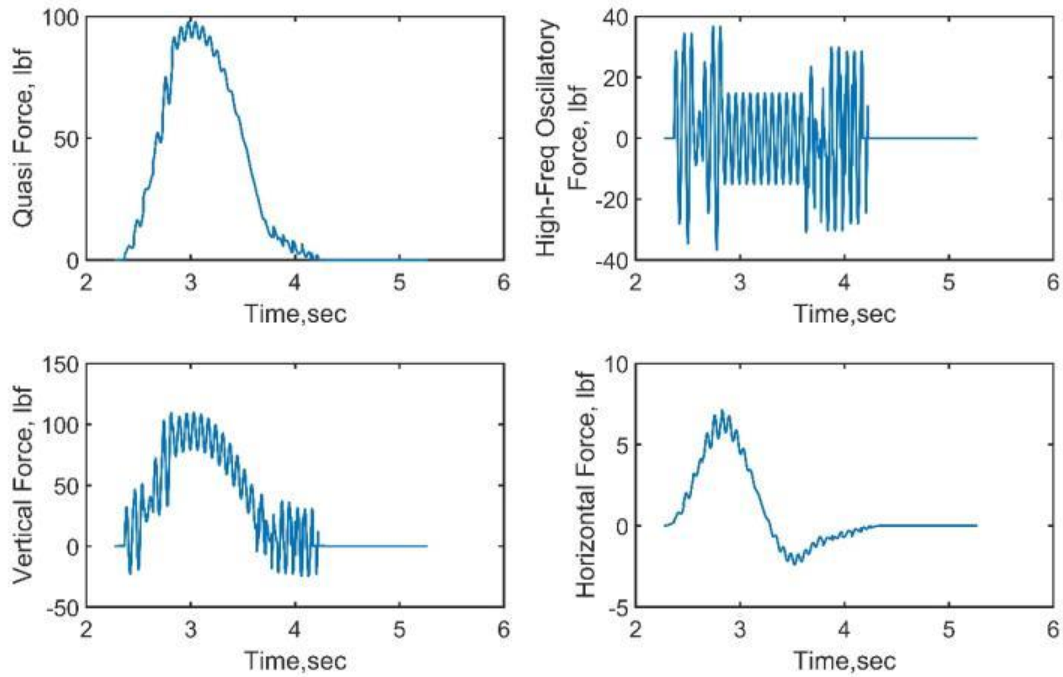

Figure C.1-4. Force Time-Histories for Bridge Configuration BSXX014

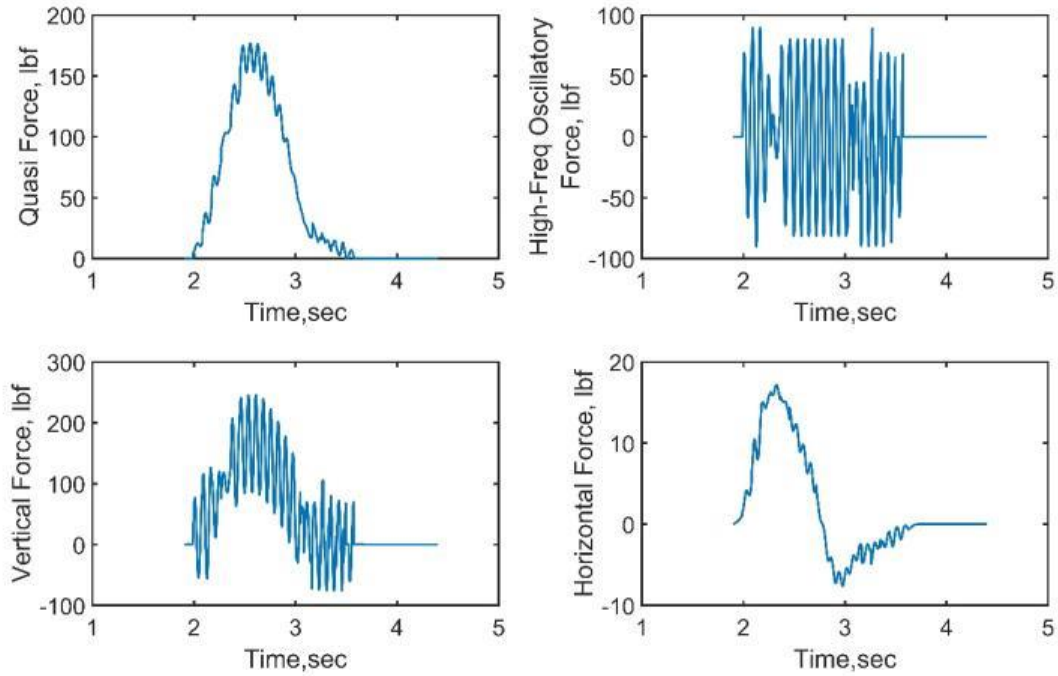

Figure C.1-5. Force Time-Histories for Bridge Configuration BSXX015

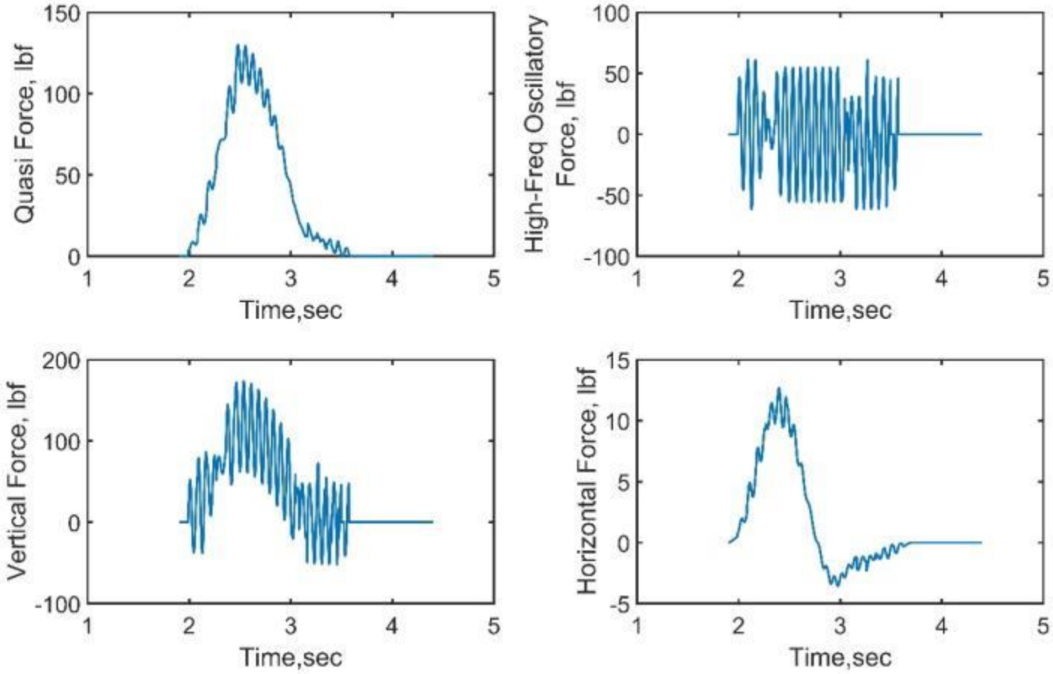

Figure C.1-6. Force Time-Histories for Bridge Configuration BSXX016

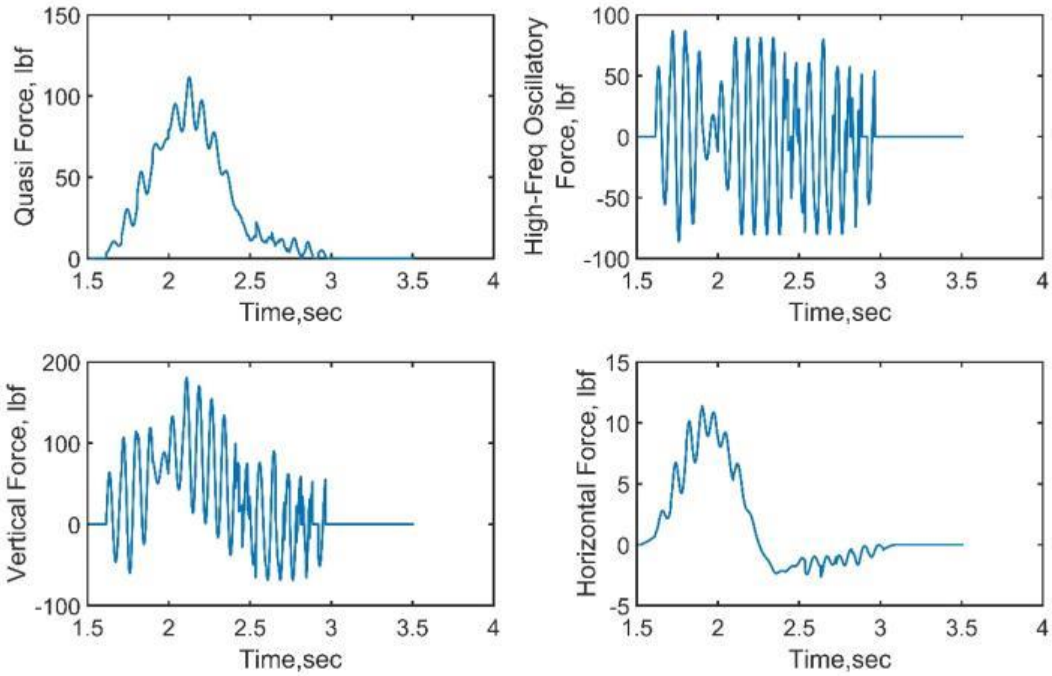

Figure C.1-7. Force Time-Histories for Bridge Configuration BSXX017

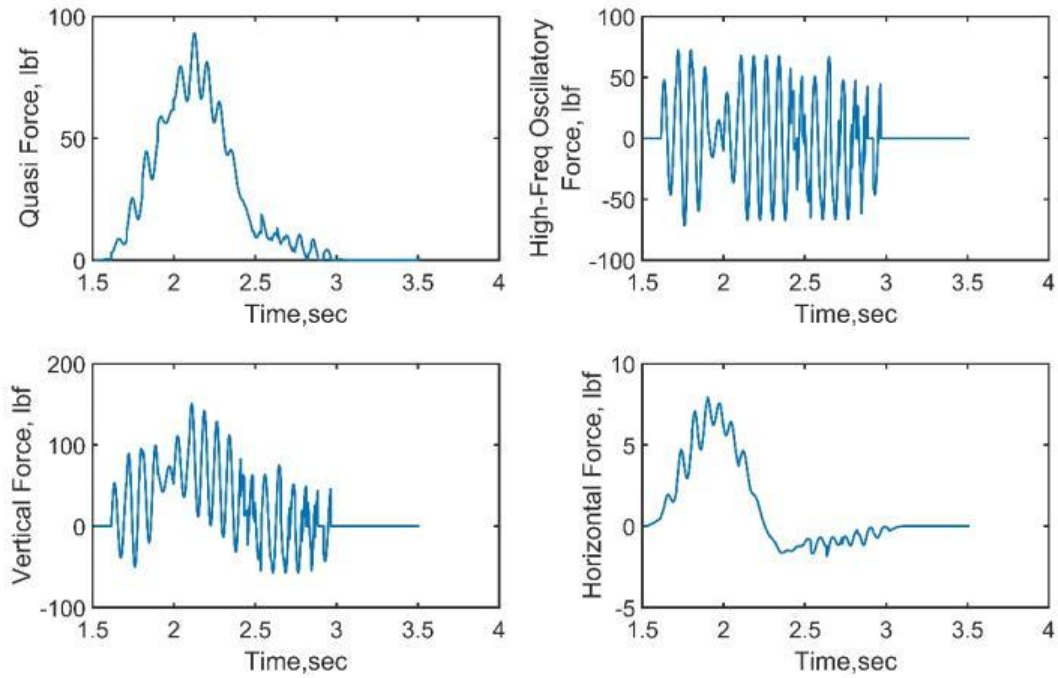

Figure C.1-8. Force Time-Histories for Bridge Configuration BSXX018

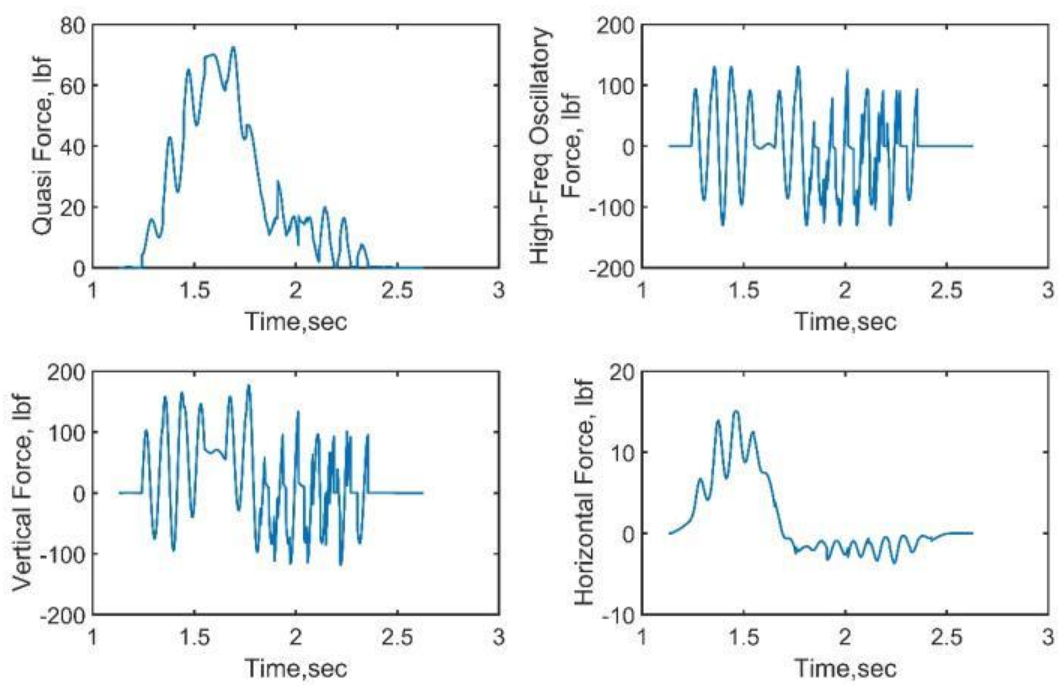

Figure C.1-9. Force Time-Histories for Bridge Configuration BSXX019

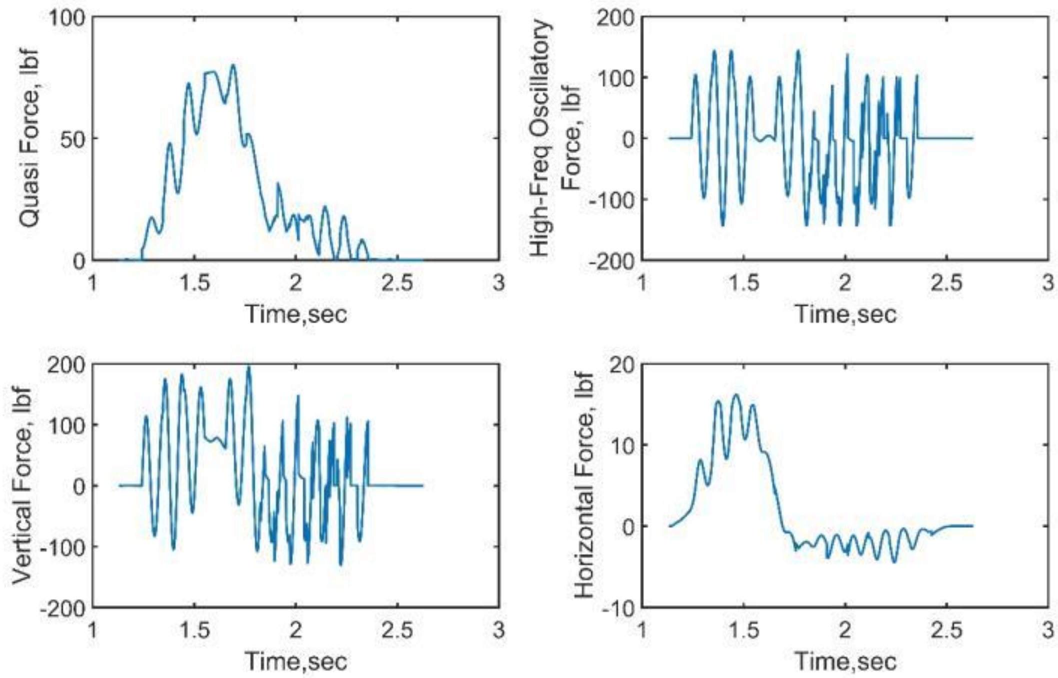

Figure C.1-10. Force Time-Histories for Bridge Configuration BSXX020

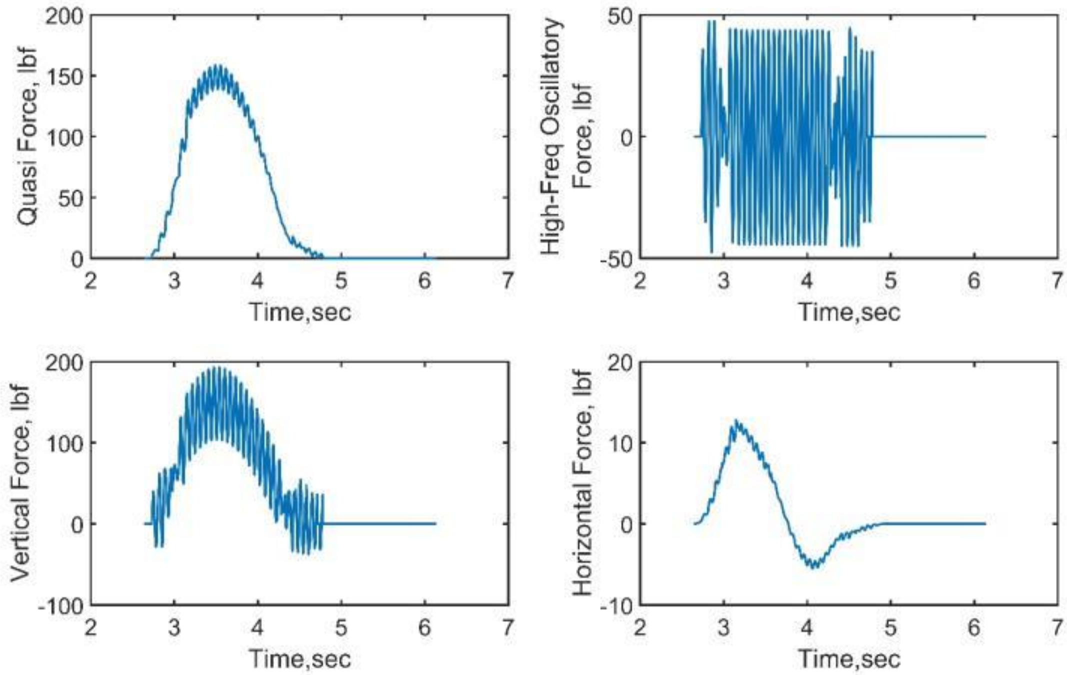

Figure C.1-11. Force Time-Histories for Bridge Configuration BSXX051

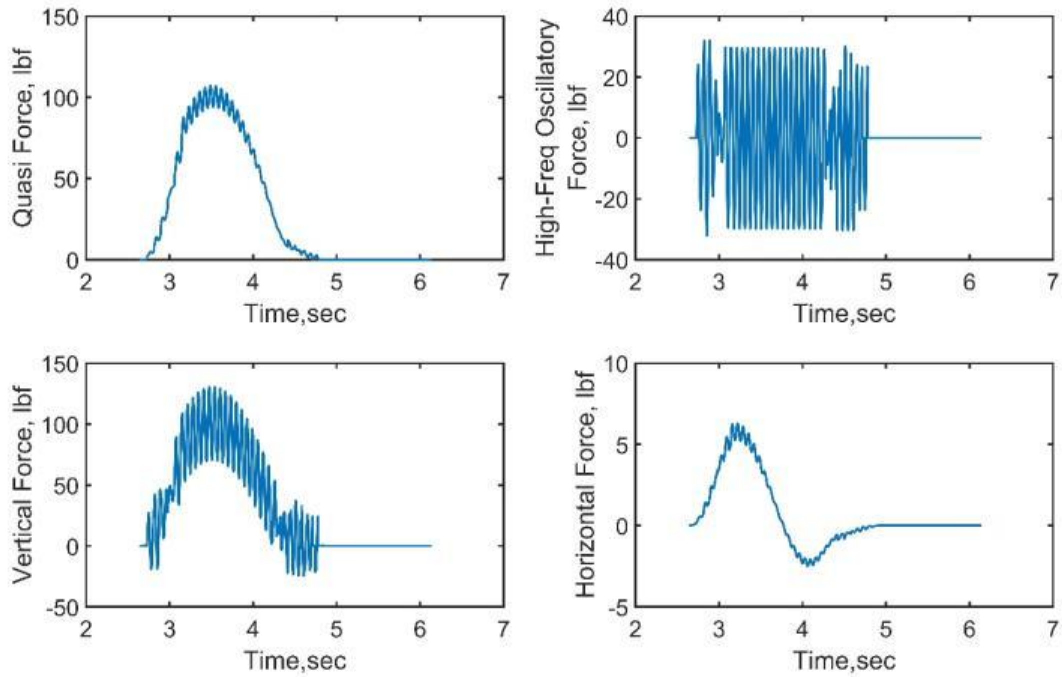

Figure C.1-12. Force Time-Histories for Bridge Configuration BSXX052

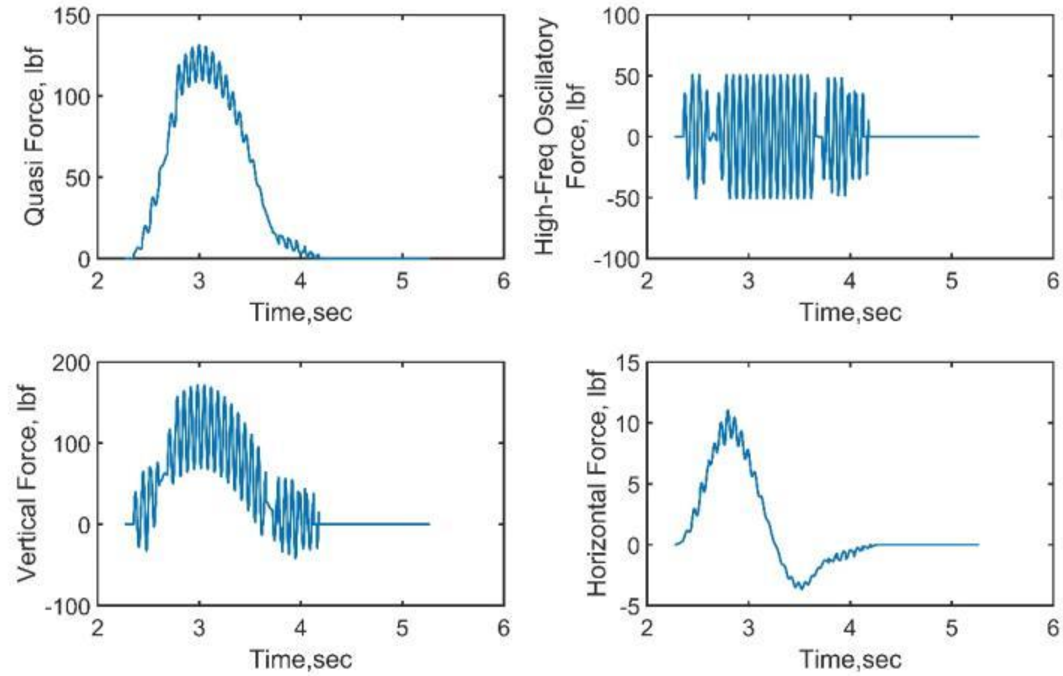

Figure C.1-13. Force Time-Histories for Bridge Configuration BSXX053

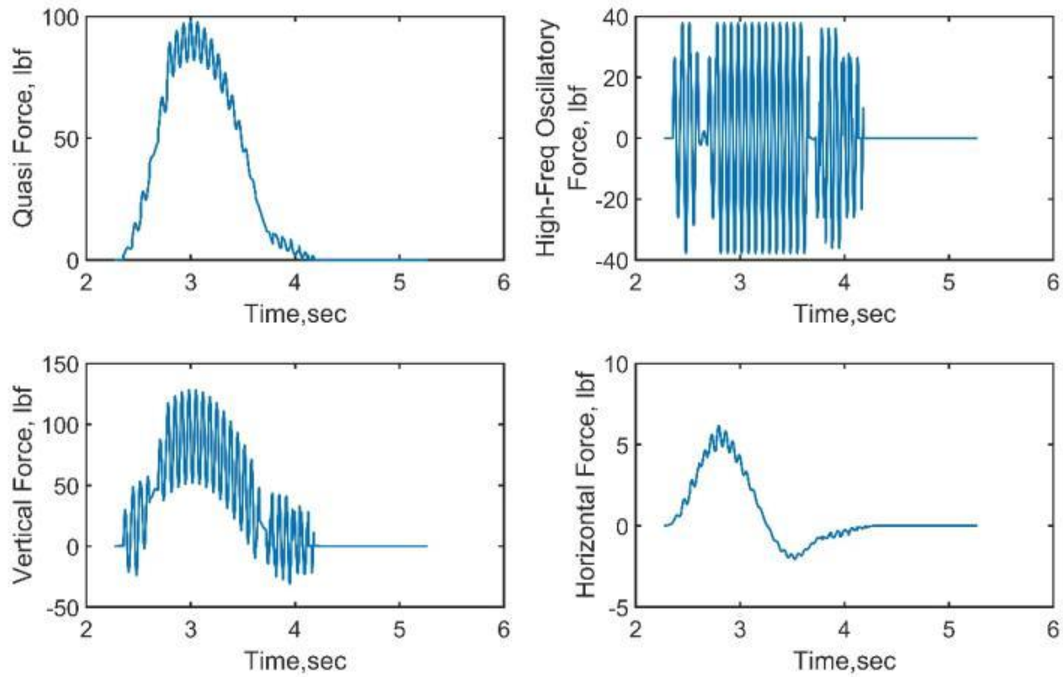

Figure C.1-14. Force Time-Histories for Bridge Configuration BSXX054

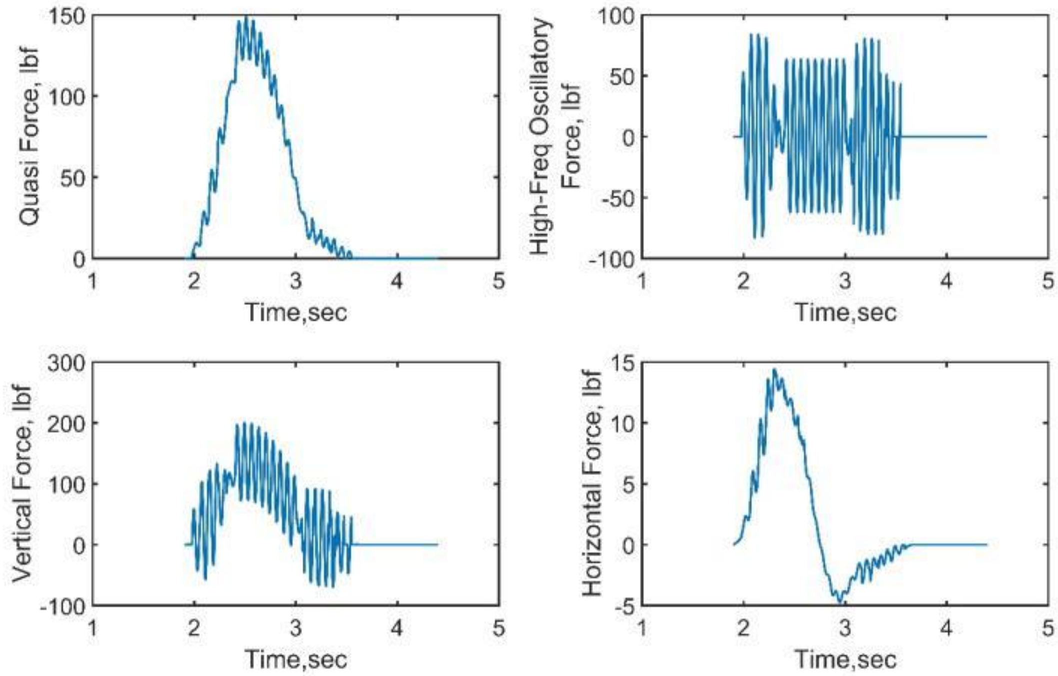

Figure C.1-15. Force Time-Histories for Bridge Configuration BSXX055

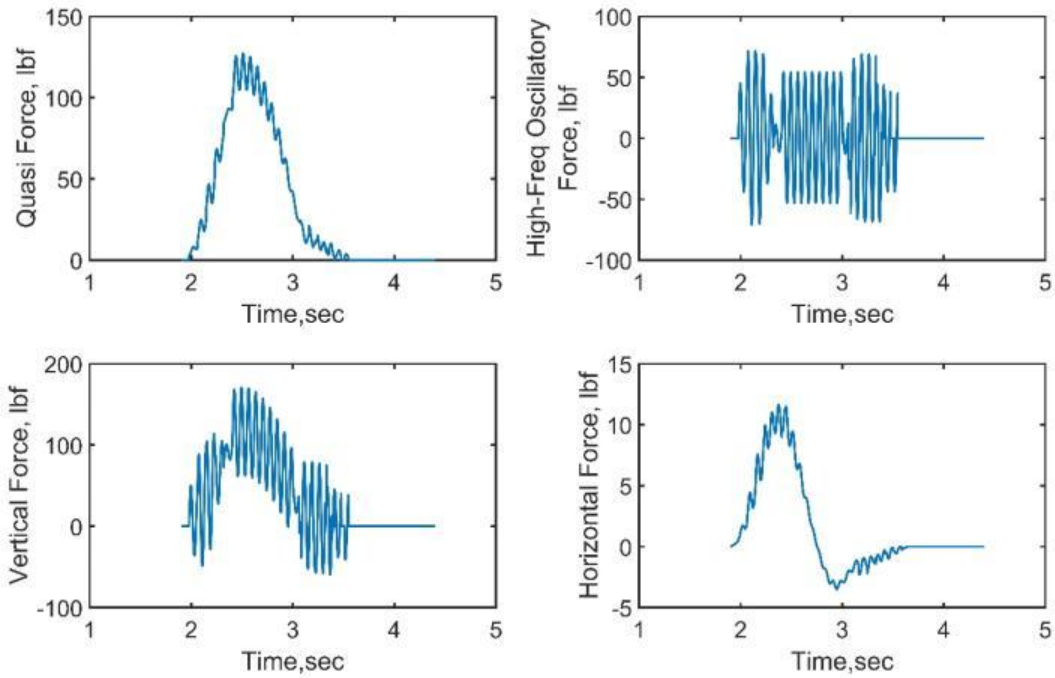

Figure C.1-16. Force Time-Histories for Bridge Configuration BSXX056

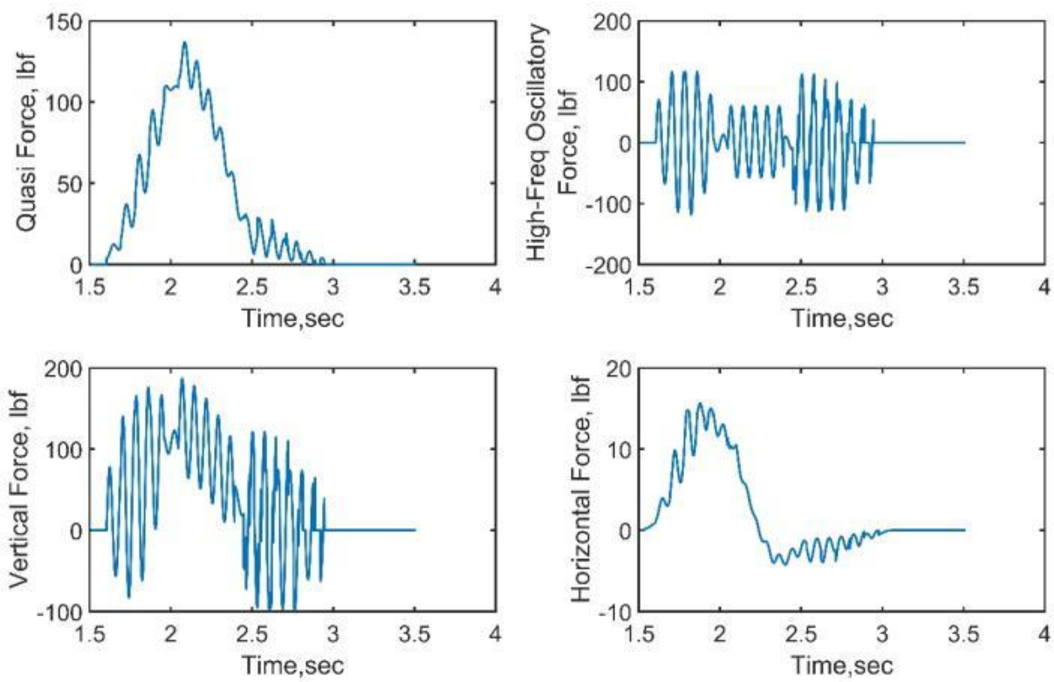

Figure C.1-17. Force Time-Histories for Bridge Configuration BSXX057

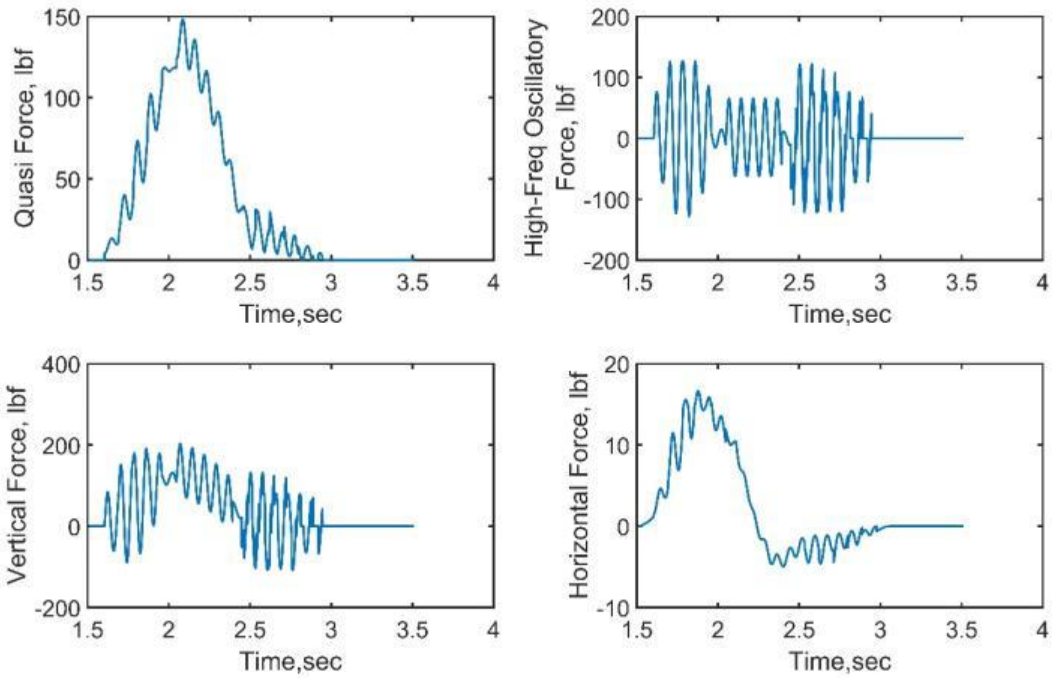

Figure C.1-18. Force Time-Histories for Bridge Configuration BSXX058

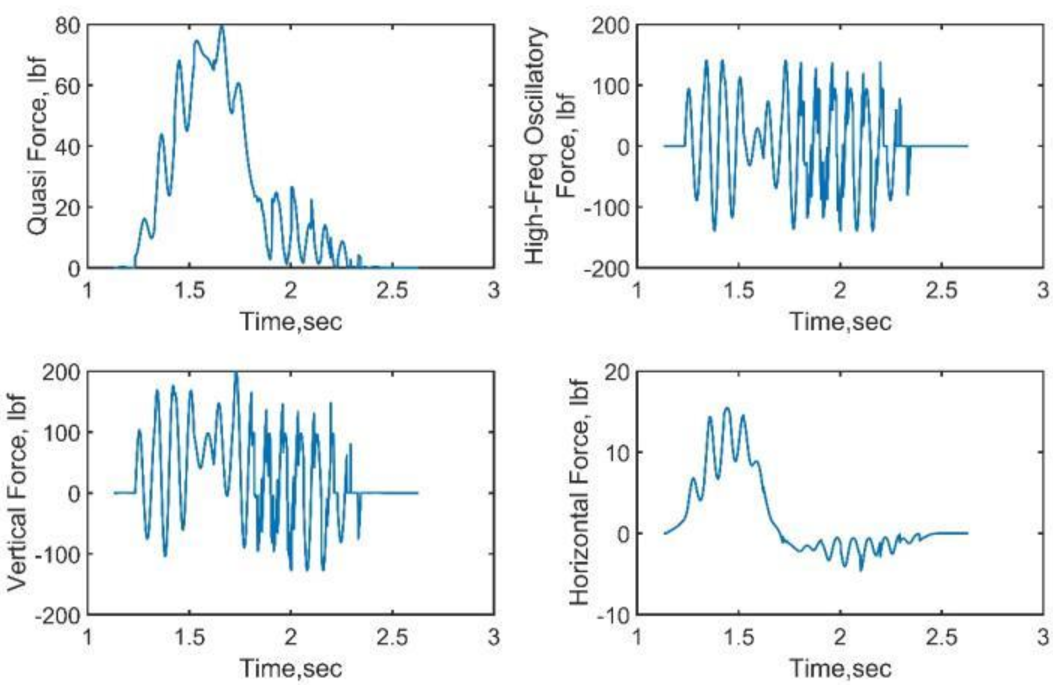

Figure C.1-19. Force Time-Histories for Bridge Configuration BSXX059

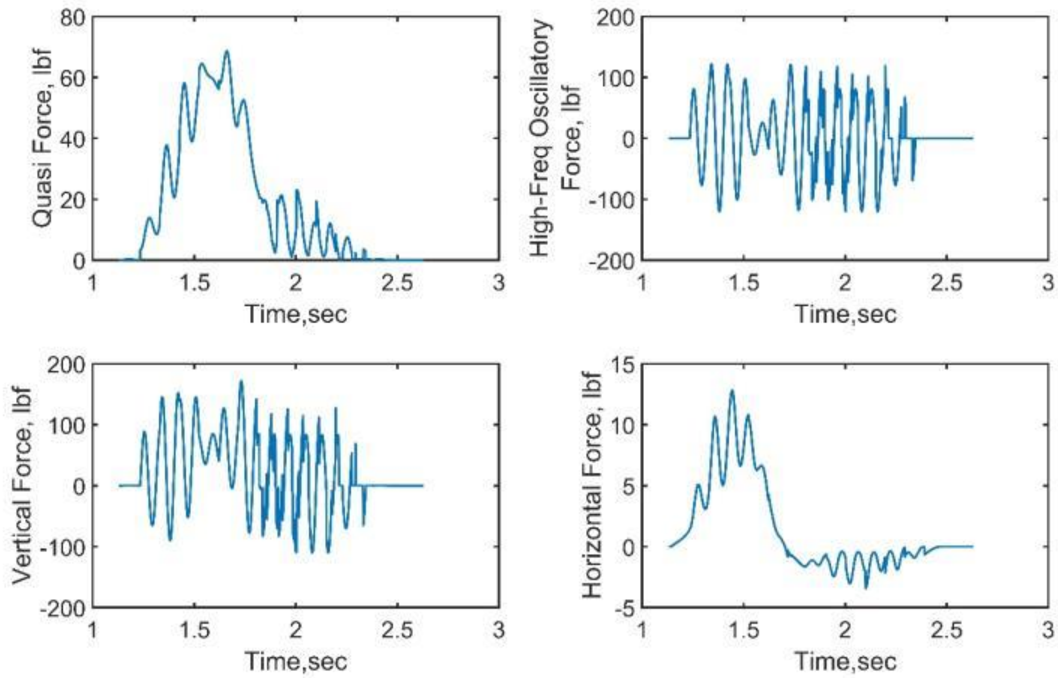

Figure C.1-20. Force Time-Histories for Bridge Configuration BSXX060

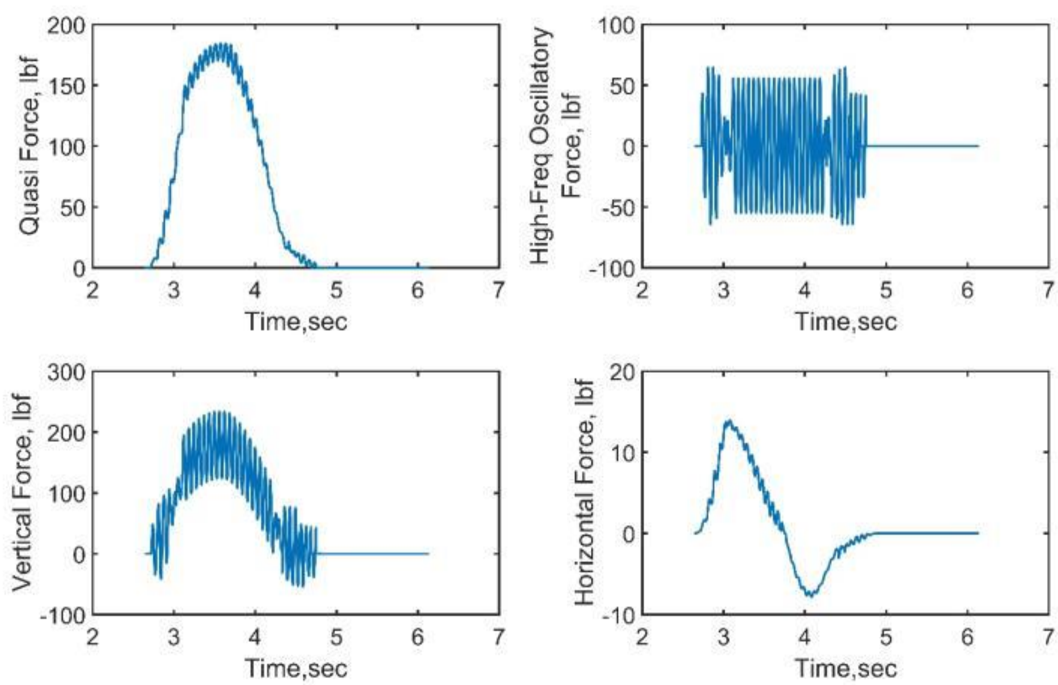

Figure C.1-21. Force Time-Histories for Bridge Configuration BSXX091

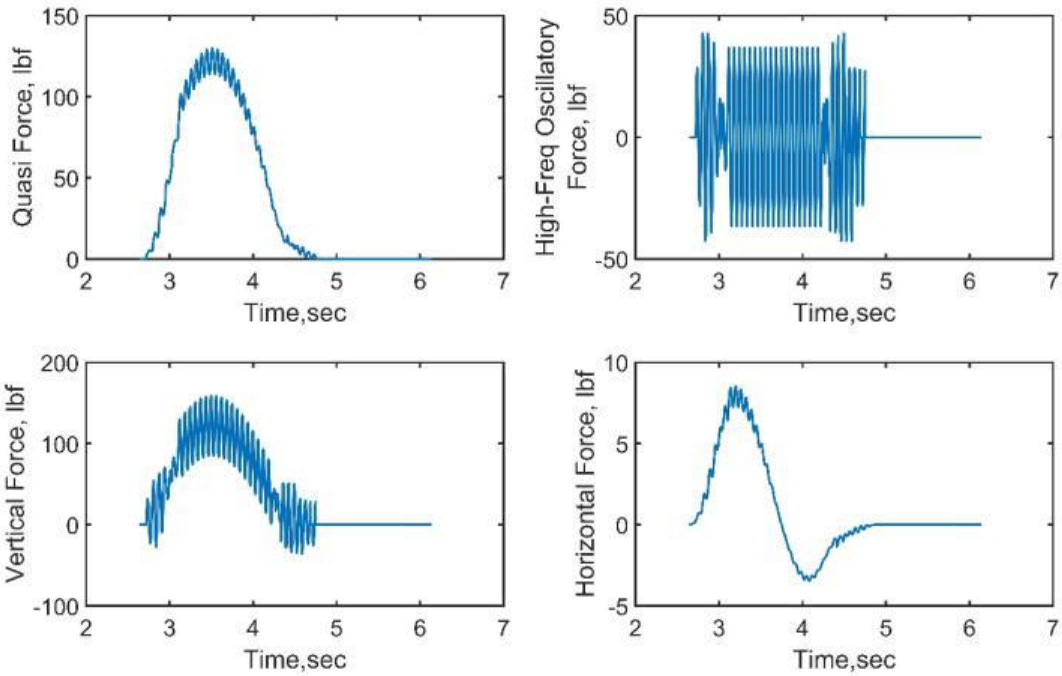

Figure C.1-22. Force Time-Histories for Bridge Configuration BSXX092

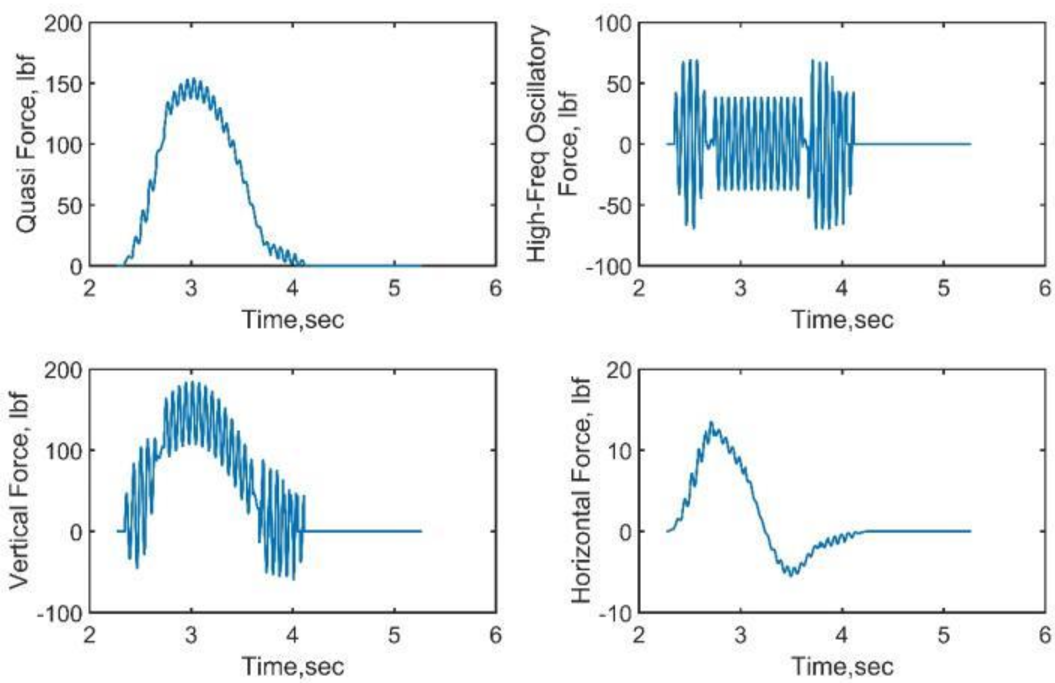

Figure C.1-23. Force Time-Histories for Bridge Configuration BSXX093

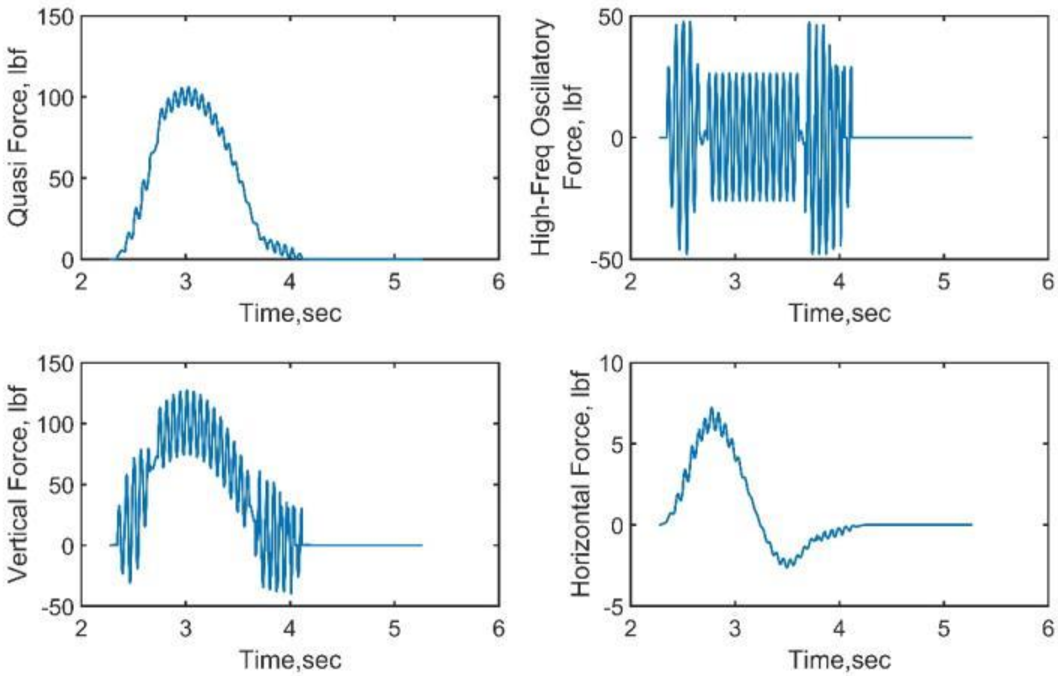

Figure C.1-24. Force Time-Histories for Bridge Configuration BSXX094

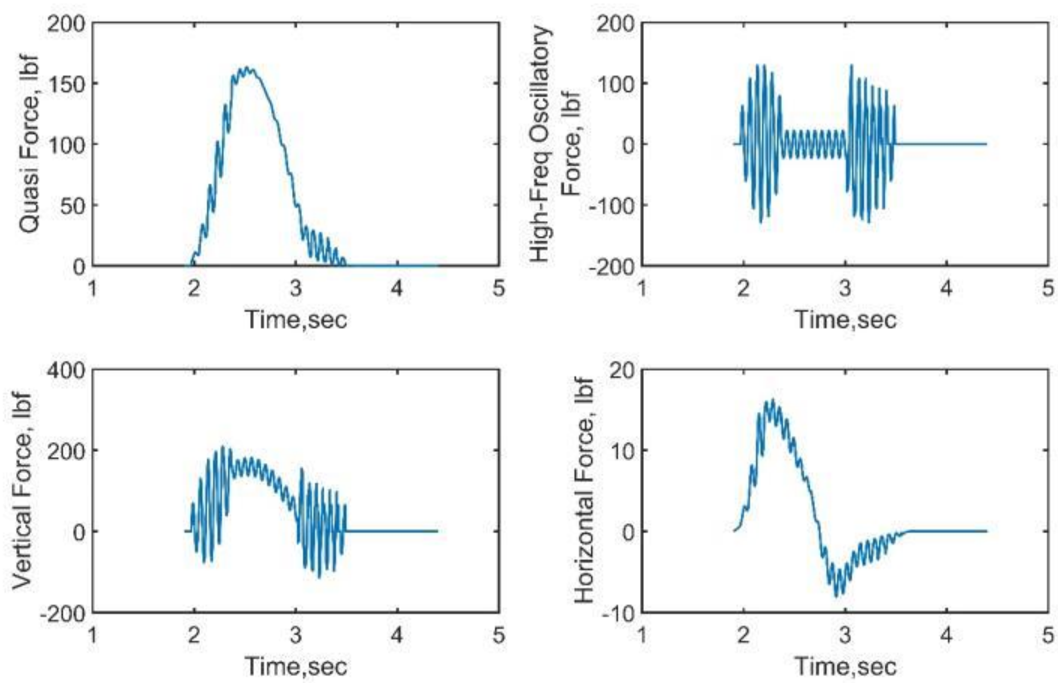

Figure C.1-25. Force Time-Histories for Bridge Configuration BSXX095

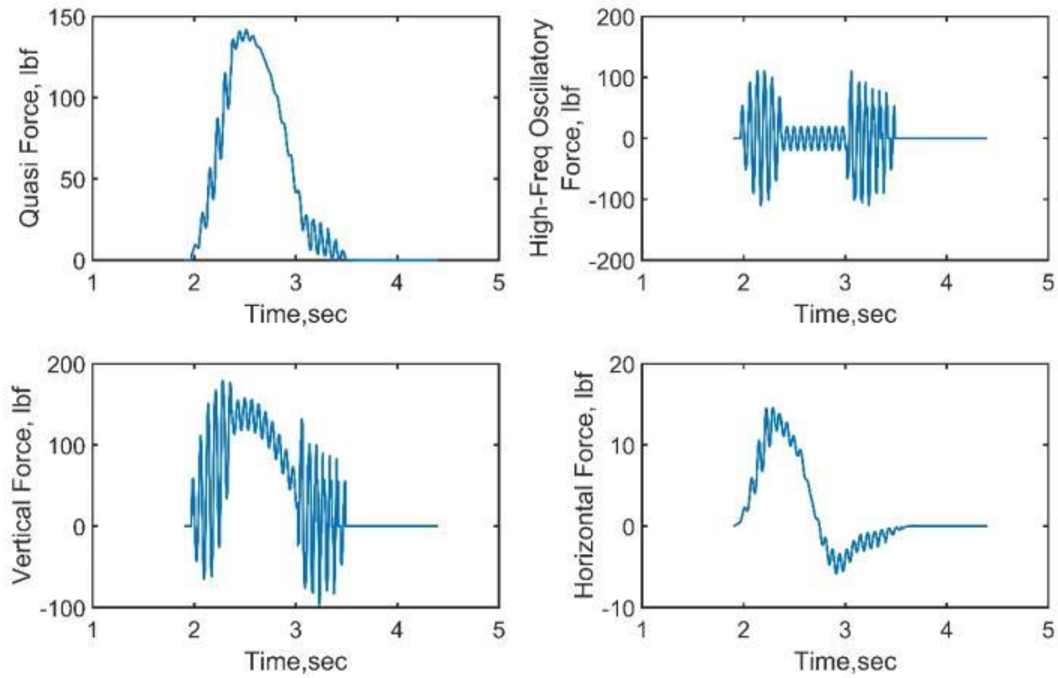

Figure C.1-26. Force Time-Histories for Bridge Configuration BSXX096

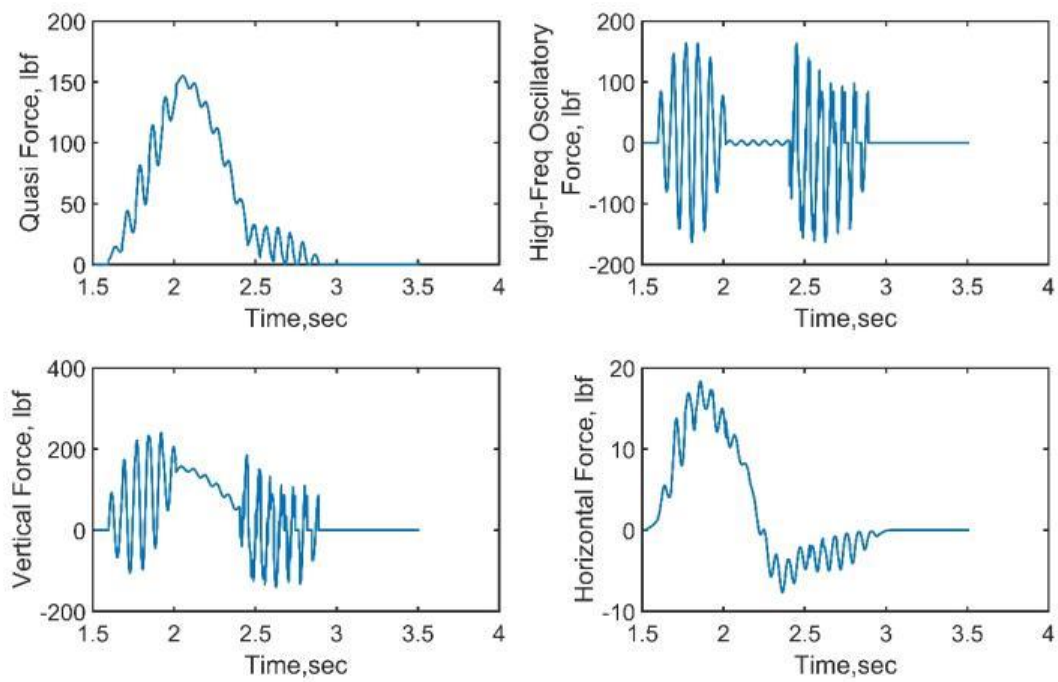

Figure C.1-27. Force Time-Histories for Bridge Configuration BSXX097

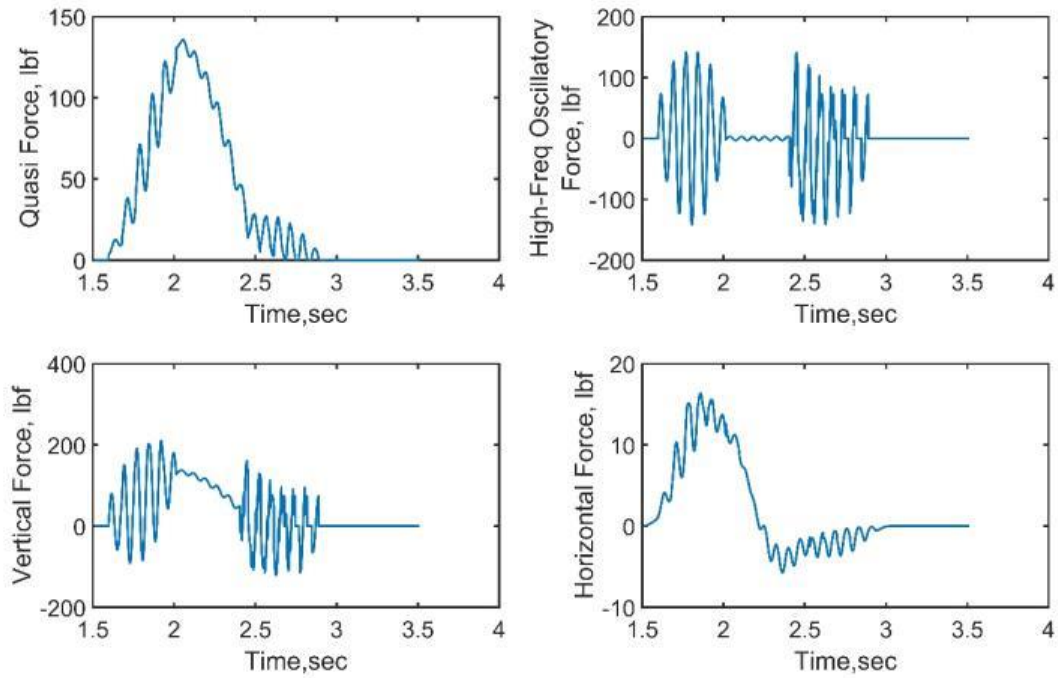

Figure C.1-28. Force Time-Histories for Bridge Configuration BSXX098

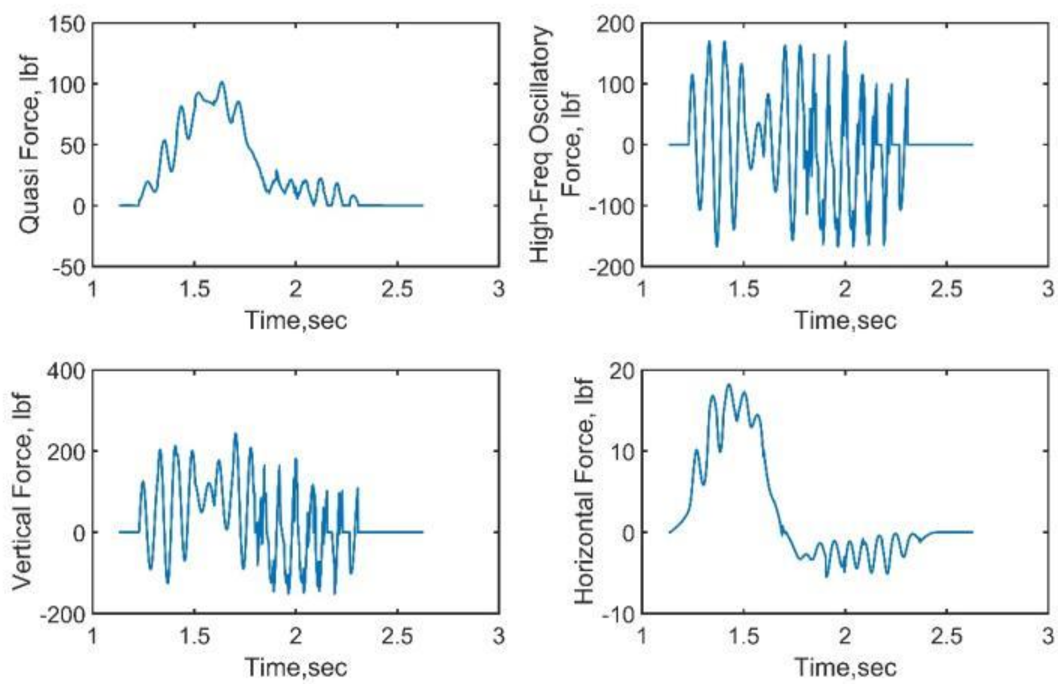

Figure C.1-29. Force Time-Histories for Bridge Configuration BSXX099

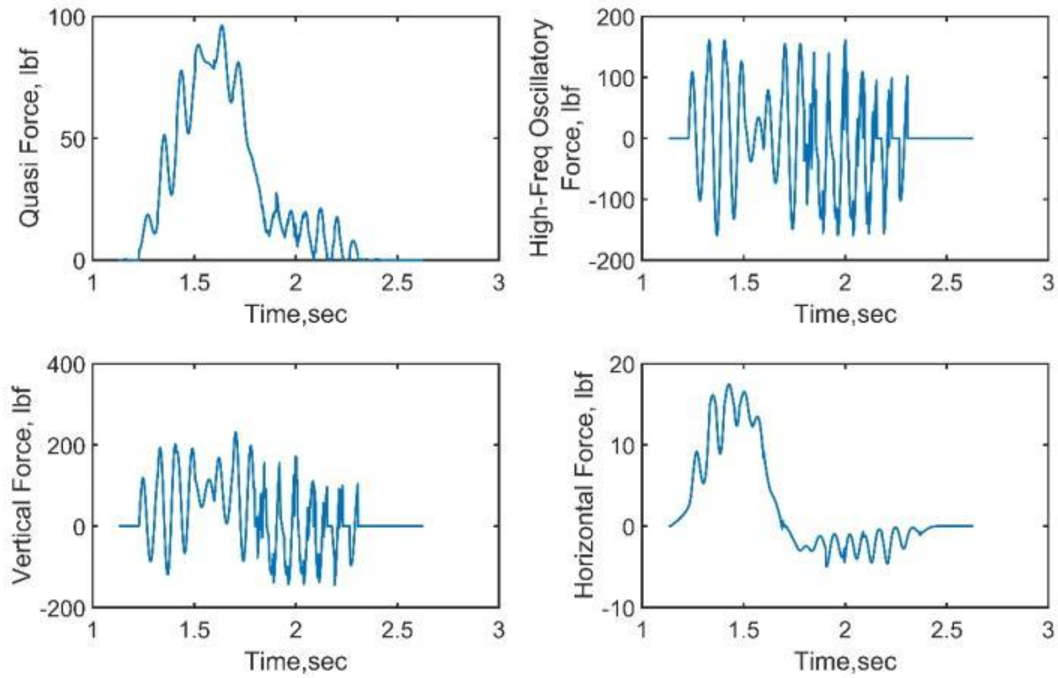

Figure C.1-30. Force Time-Histories for Bridge Configuration BSXX100

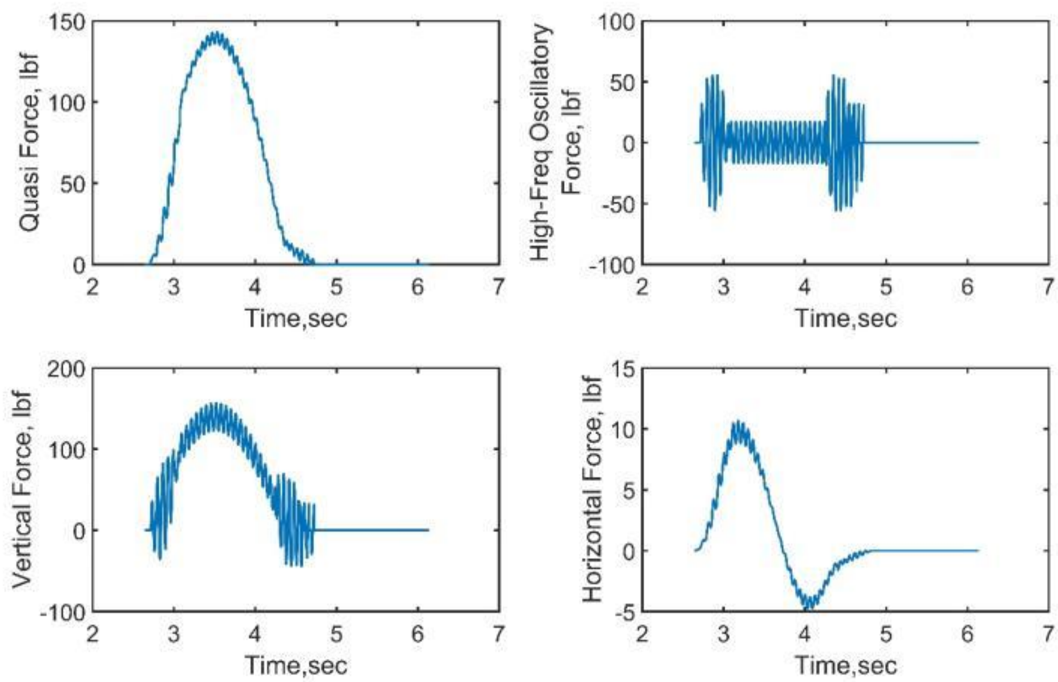

Figure C.1-31. Force Time-Histories for Bridge Configuration BSXX131

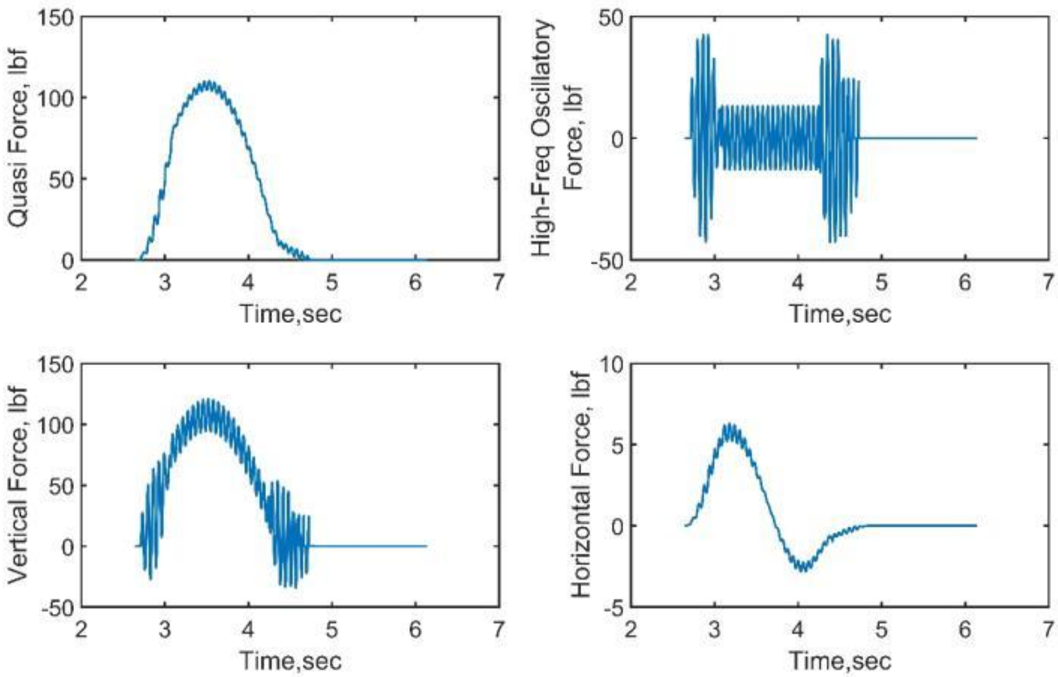

Figure C.1-32. Force Time-Histories for Bridge Configuration BSXX132

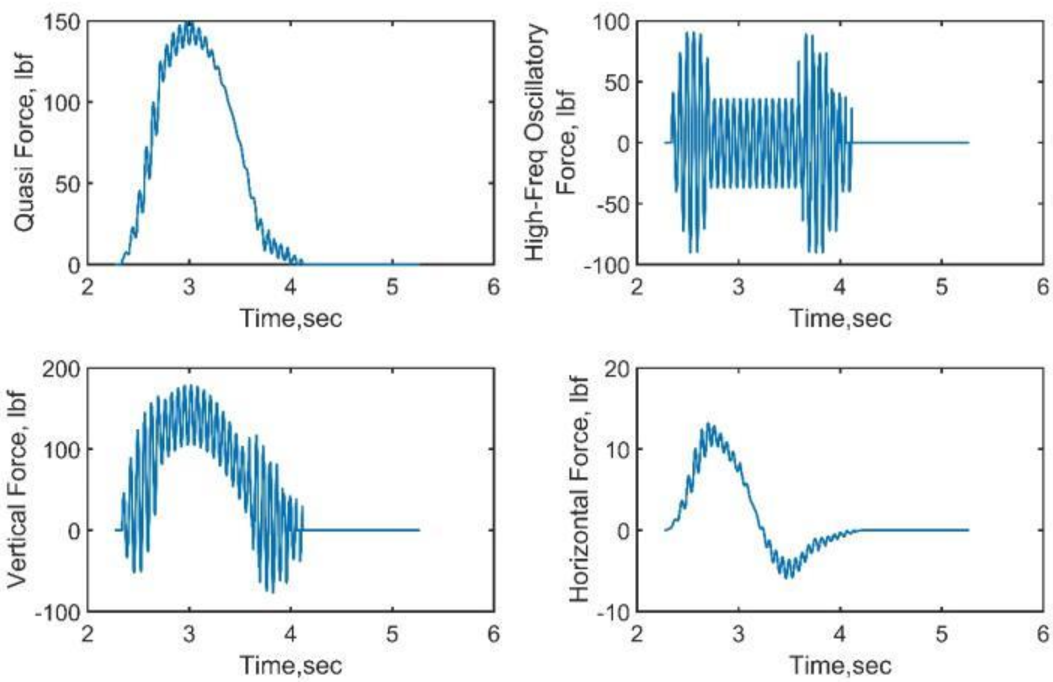

Figure C.1-33. Force Time-Histories for Bridge Configuration BSXX133

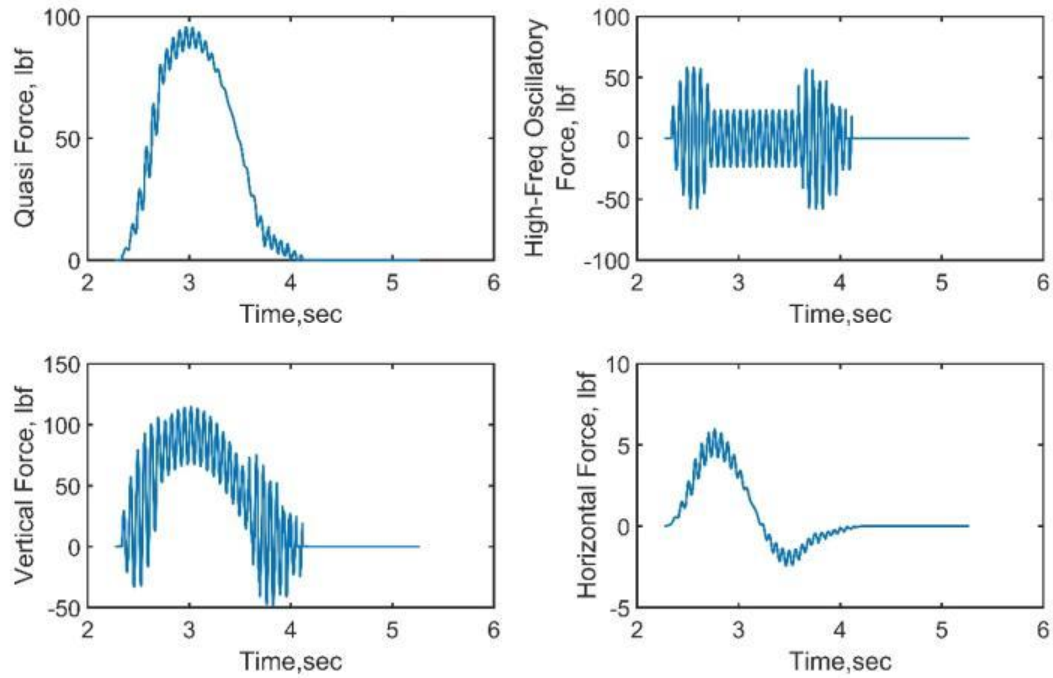

Figure C.1-34. Force Time-Histories for Bridge Configuration BSXX134

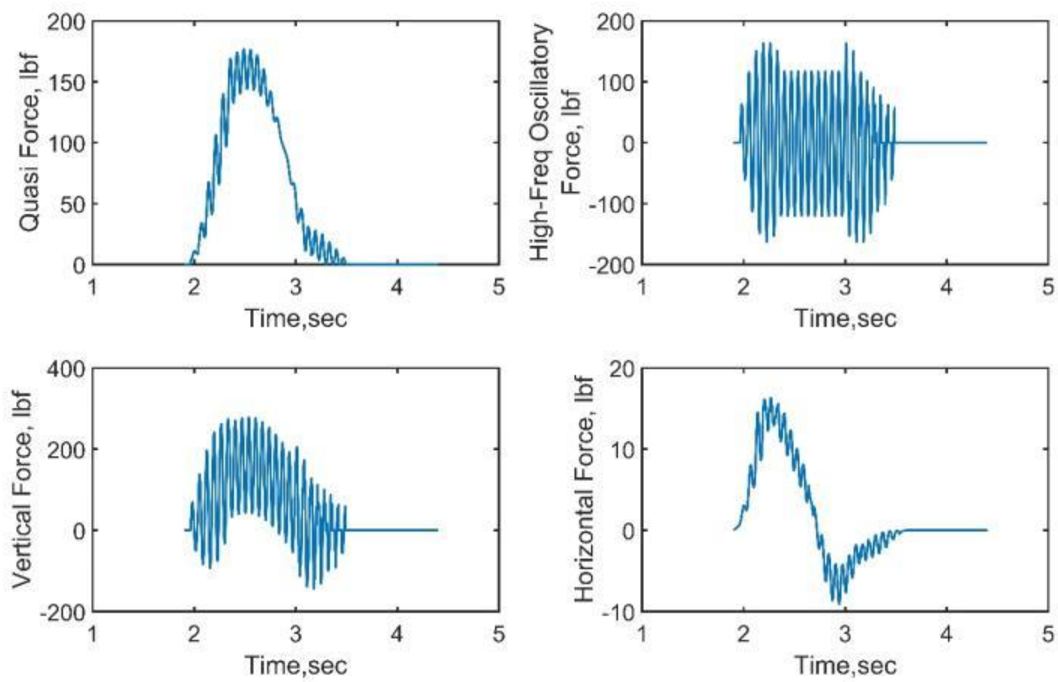

Figure C.1-35. Force Time-Histories for Bridge Configuration BSXX135

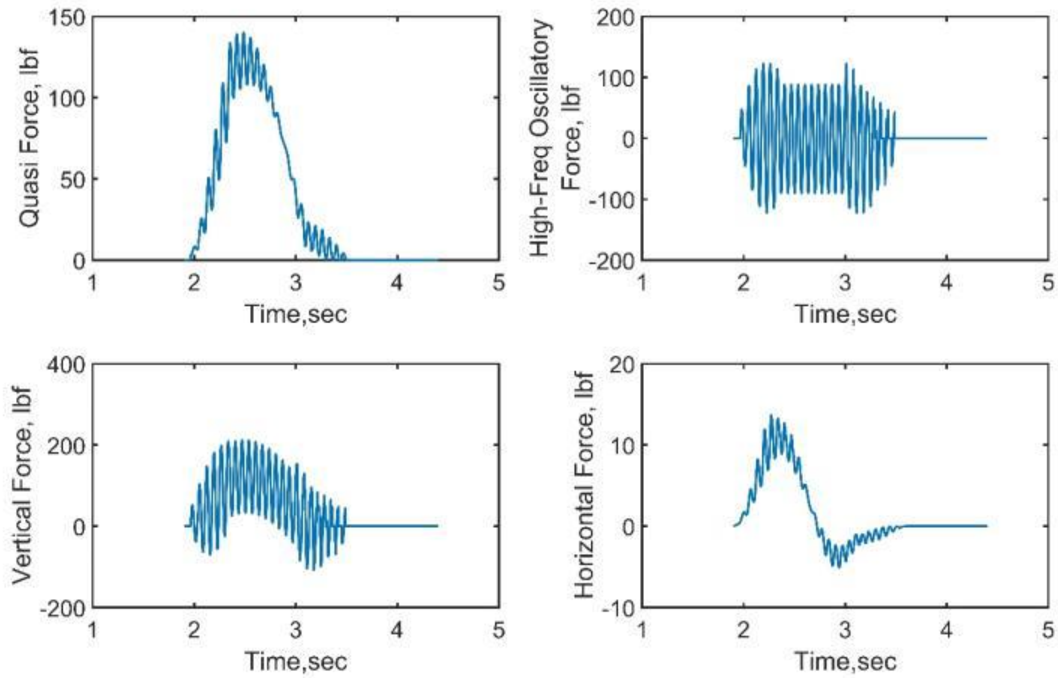

Figure C.1-36. Force Time-Histories for Bridge Configuration BSXX136

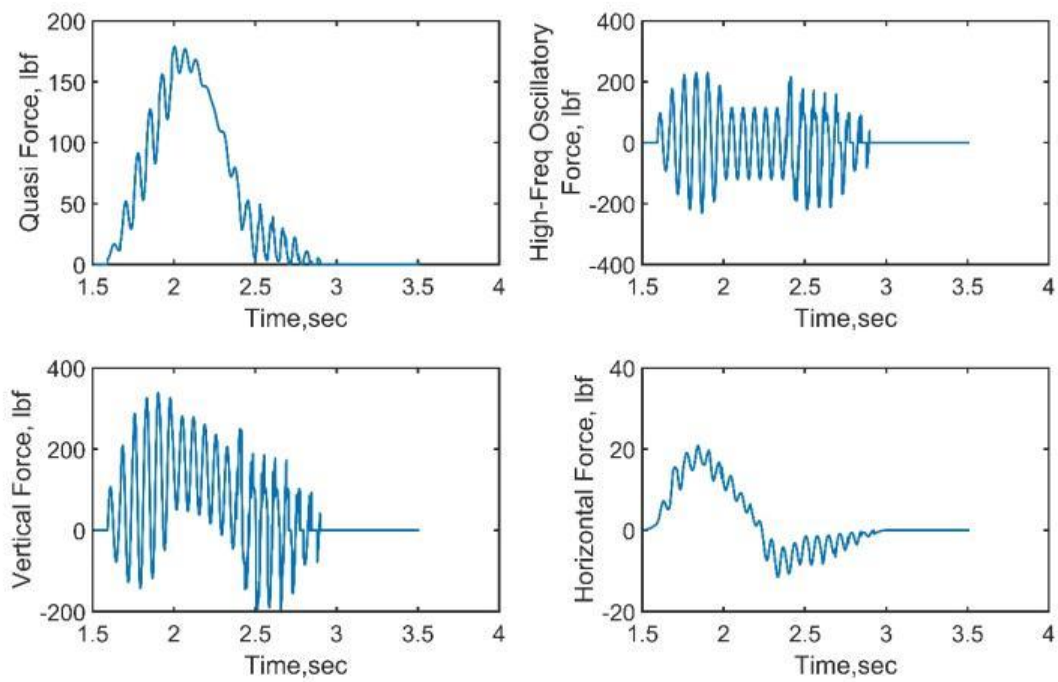

Figure C.1-37. Force Time-Histories for Bridge Configuration BSXX137

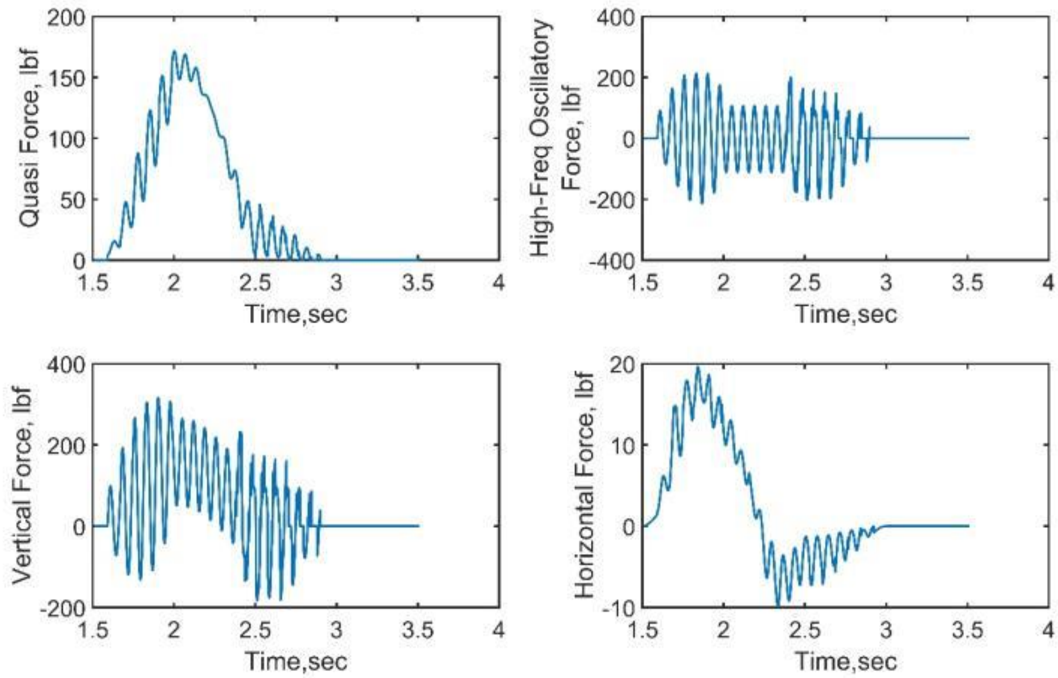

Figure C.1-38. Force Time-Histories for Bridge Configuration BSXX138

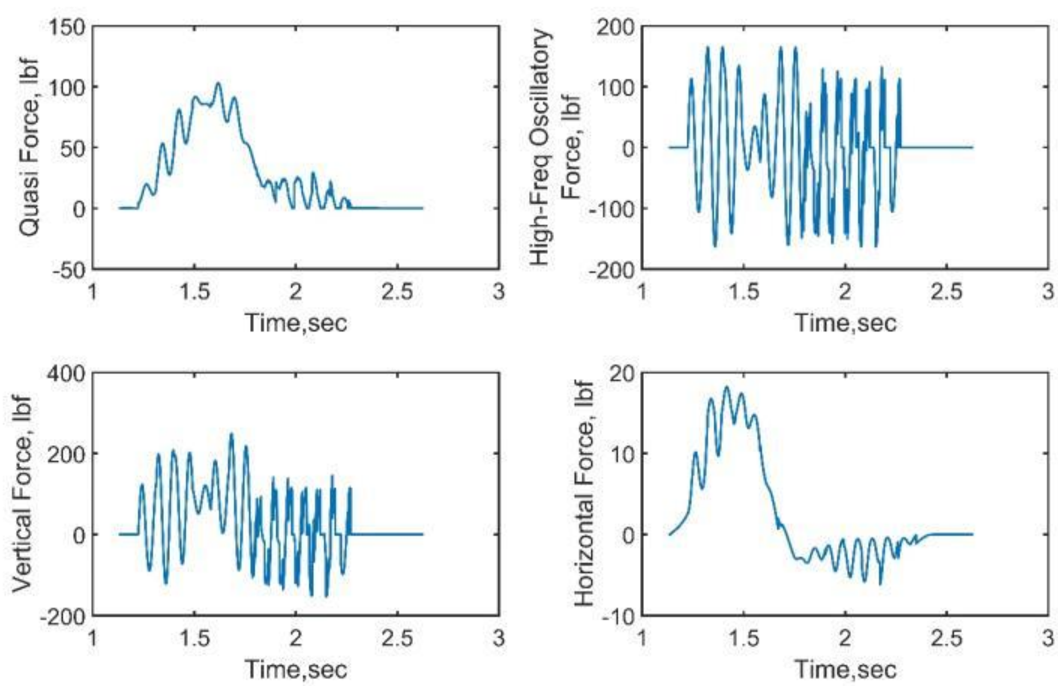

Figure C.1-39. Force Time-Histories for Bridge Configuration BSXX139

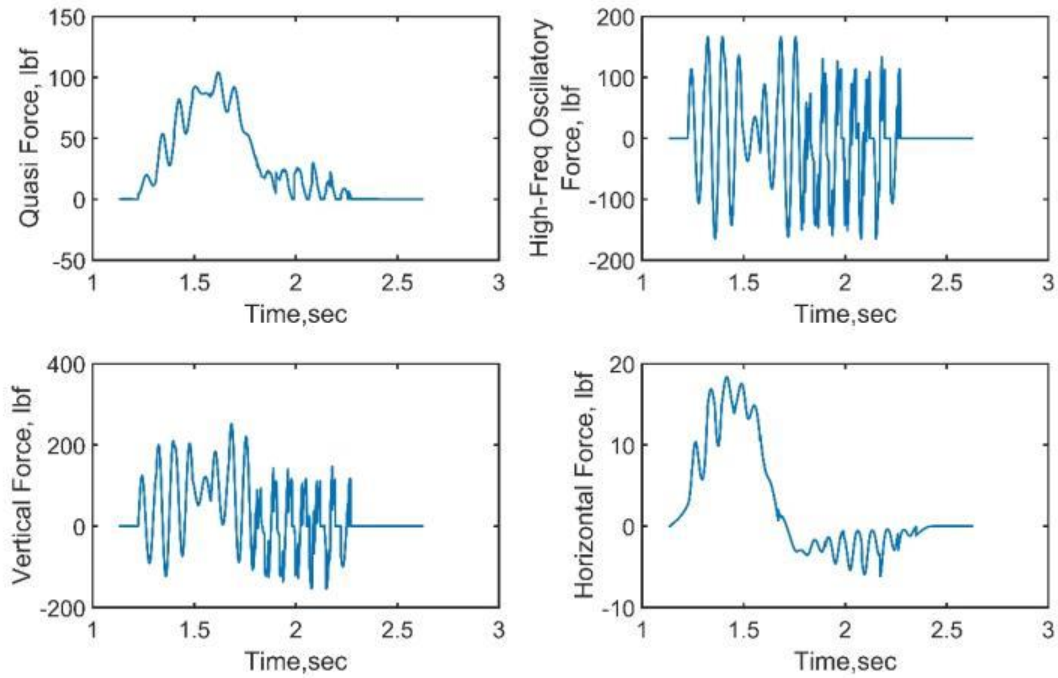

Figure C.1-40. Force Time-Histories for Bridge Configuration BSXX140

C. 2. NO TRAPPED AIR (FULL VENTED DECK)

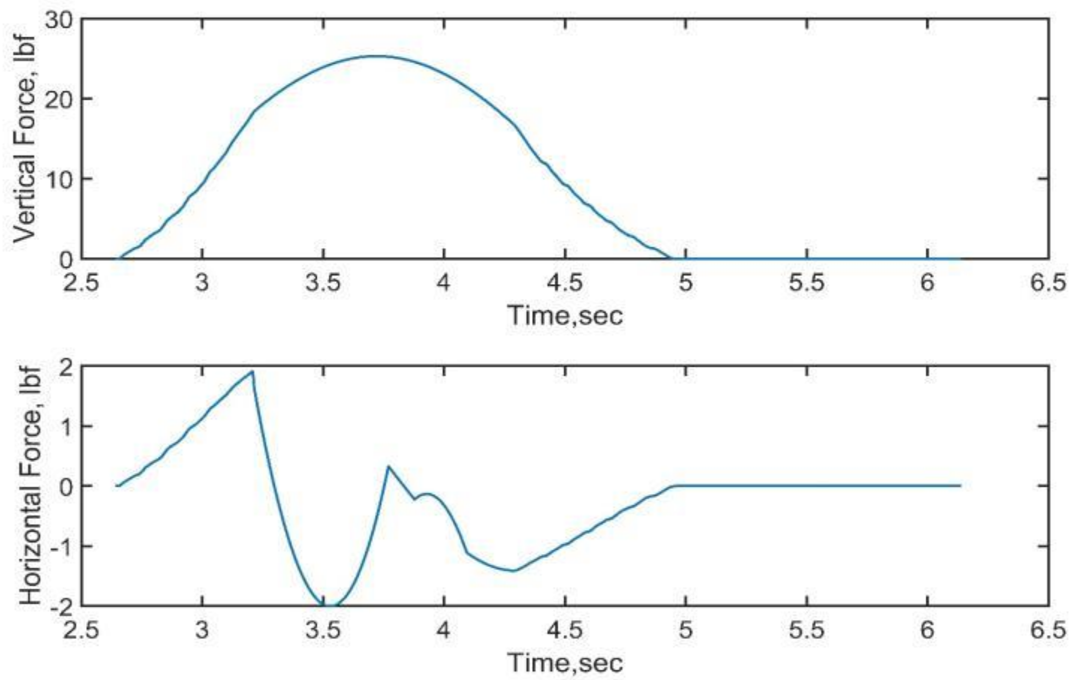

Figure C.2-1. Force Time-Histories for Bridge Configuration BSXX011

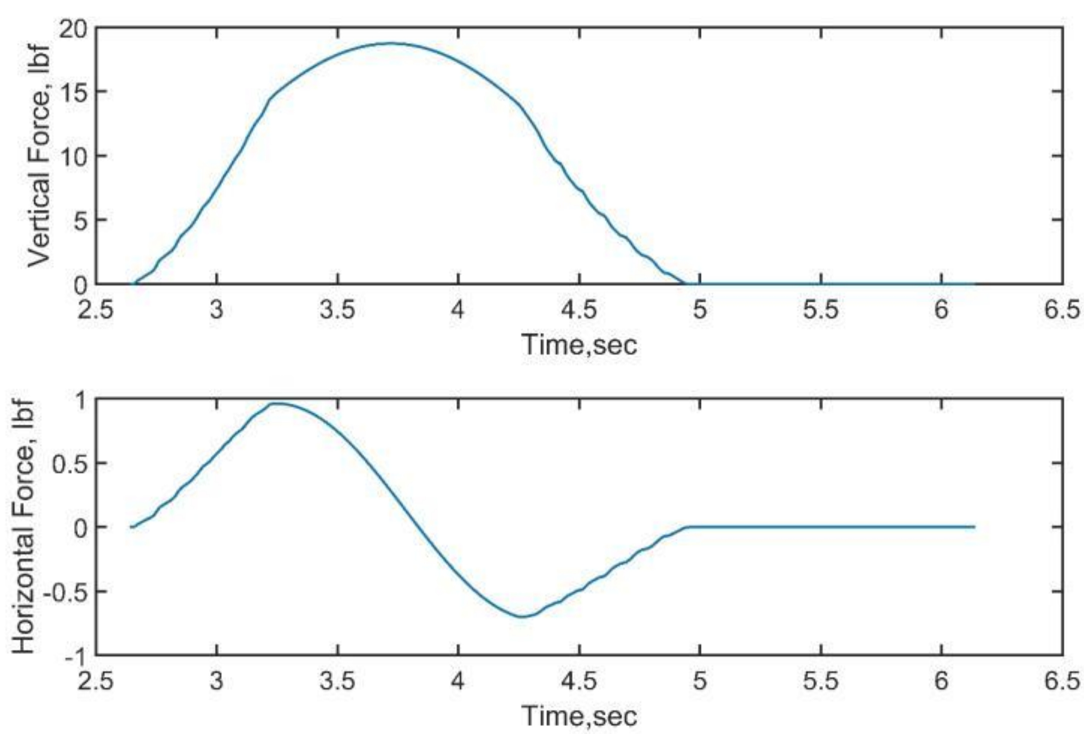

Figure C.2-2. Force Time-Histories for Bridge Configuration BSXX012

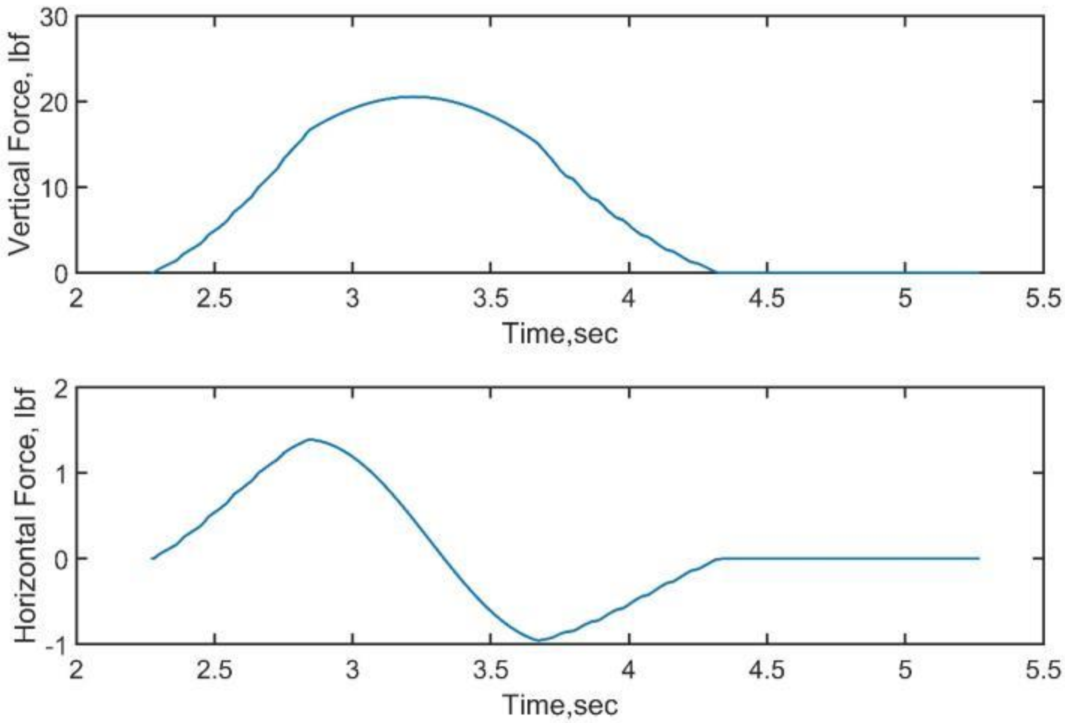

Figure C.2-3. Force Time-Histories for Bridge Configuration BSXX013

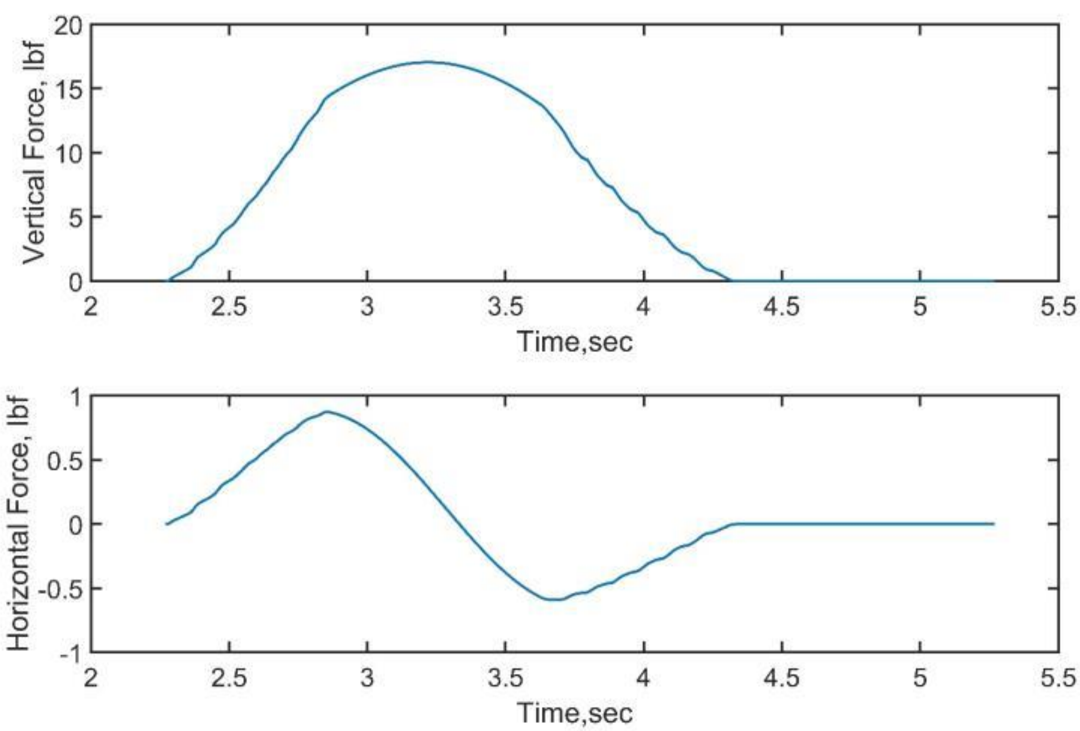

Figure C.2-4. Force Time-Histories for Bridge Configuration BSXX014

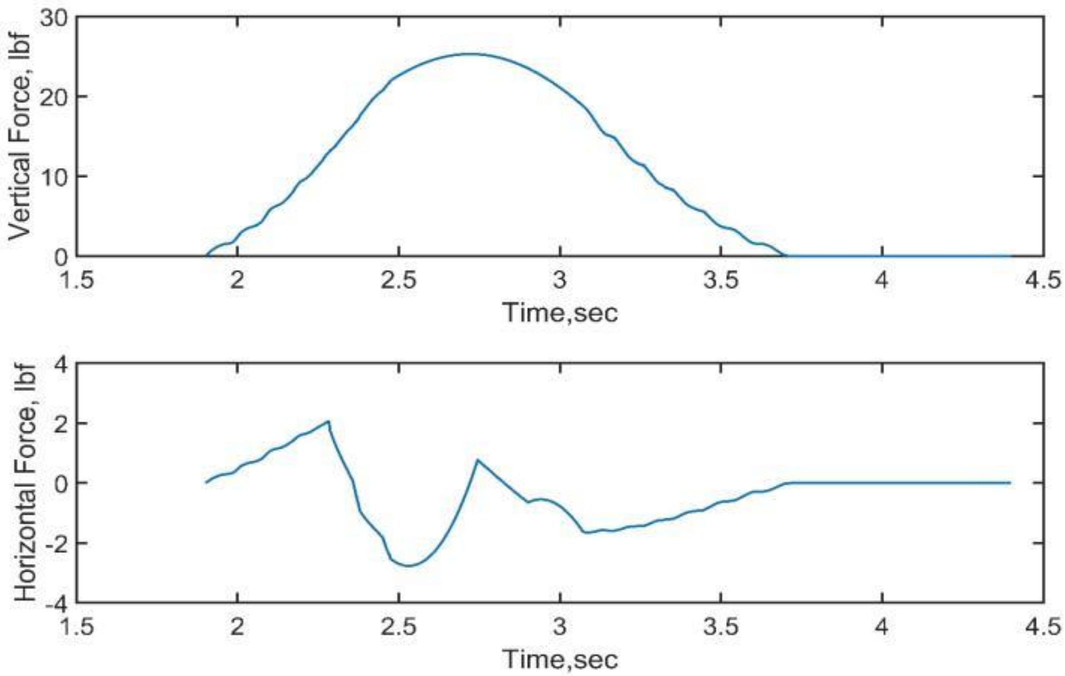

Figure C.2-5. Force Time-Histories for Bridge Configuration BSXX015

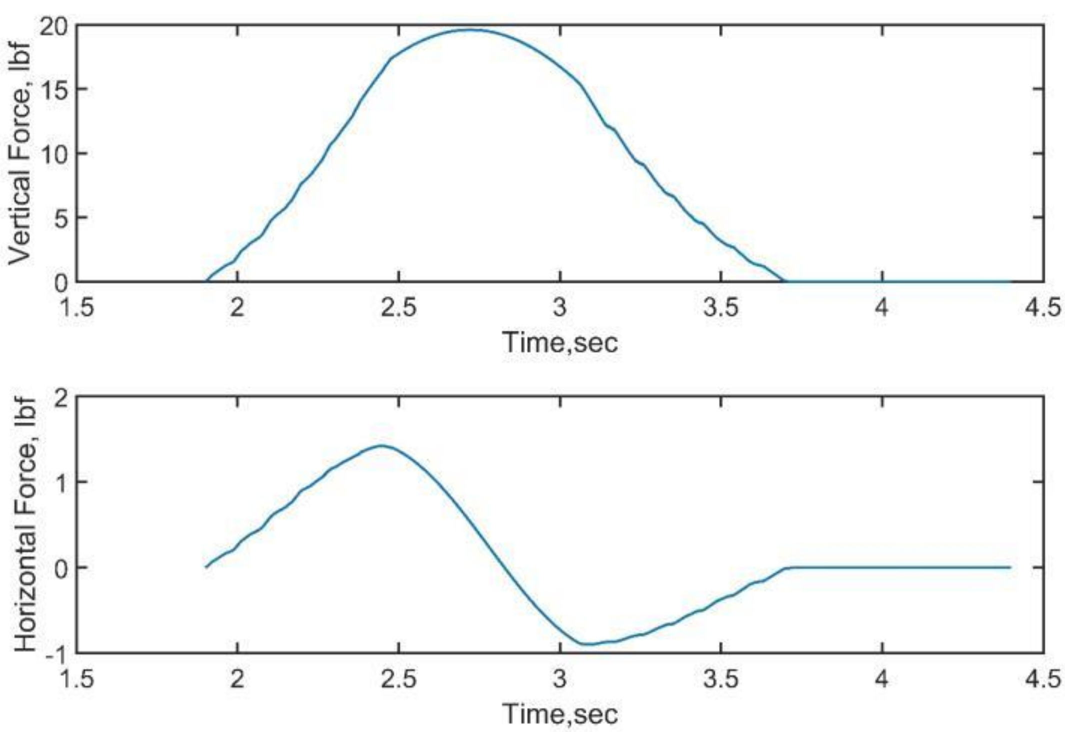

Figure C.2-6. Force Time-Histories for Bridge Configuration BSXX016

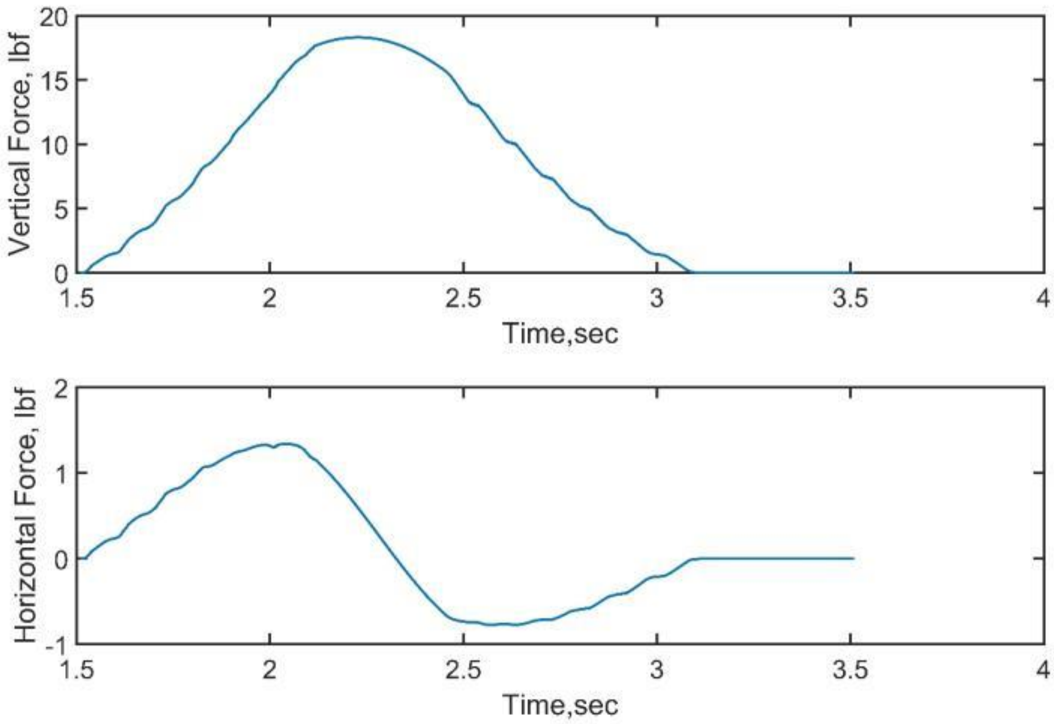

Figure C.2-7. Force Time-Histories for Bridge Configuration BSXX017

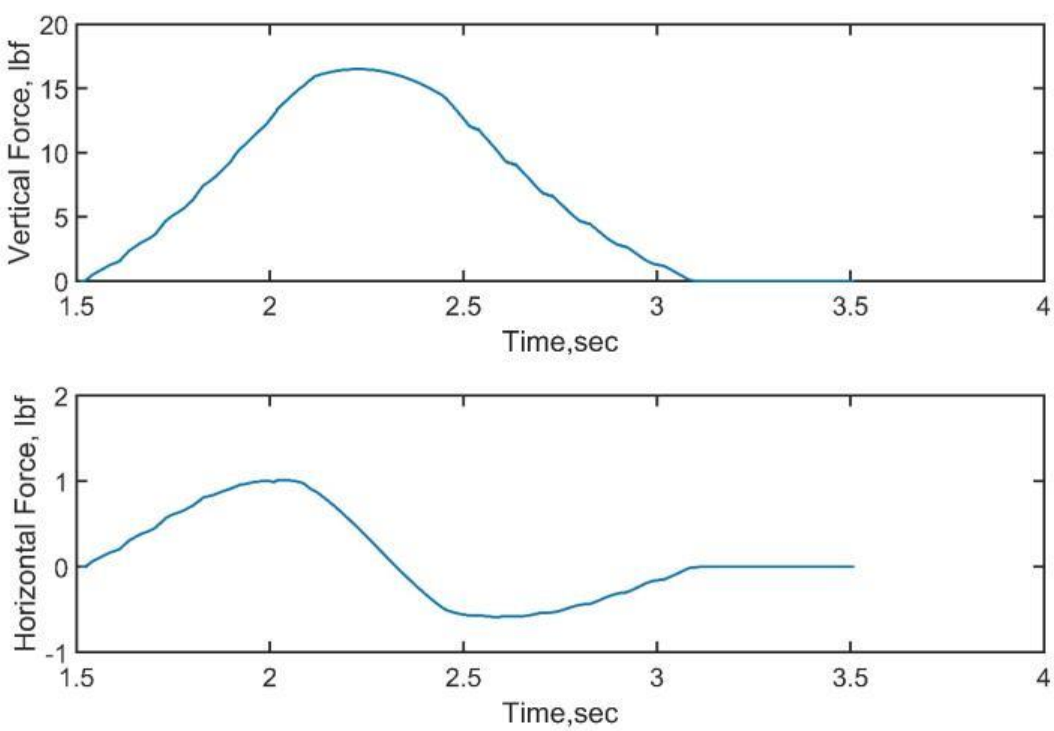

Figure C.2-8. Force Time-Histories for Bridge Configuration BSXX018

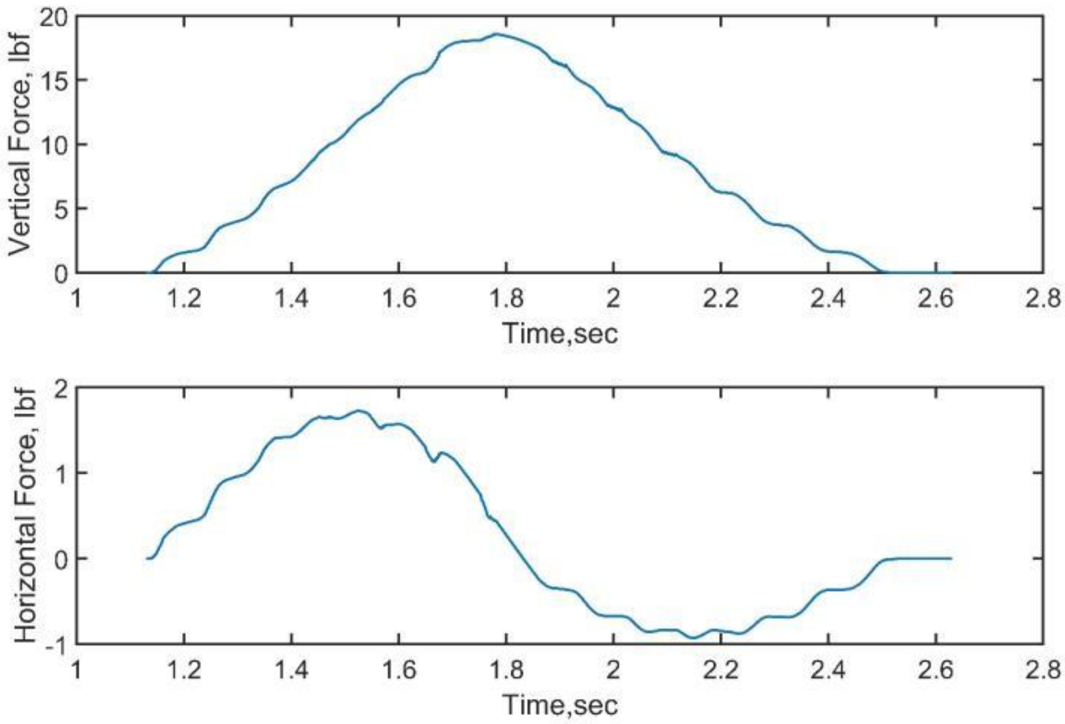

Figure C.2-9. Force Time-Histories for Bridge Configuration BSXX019

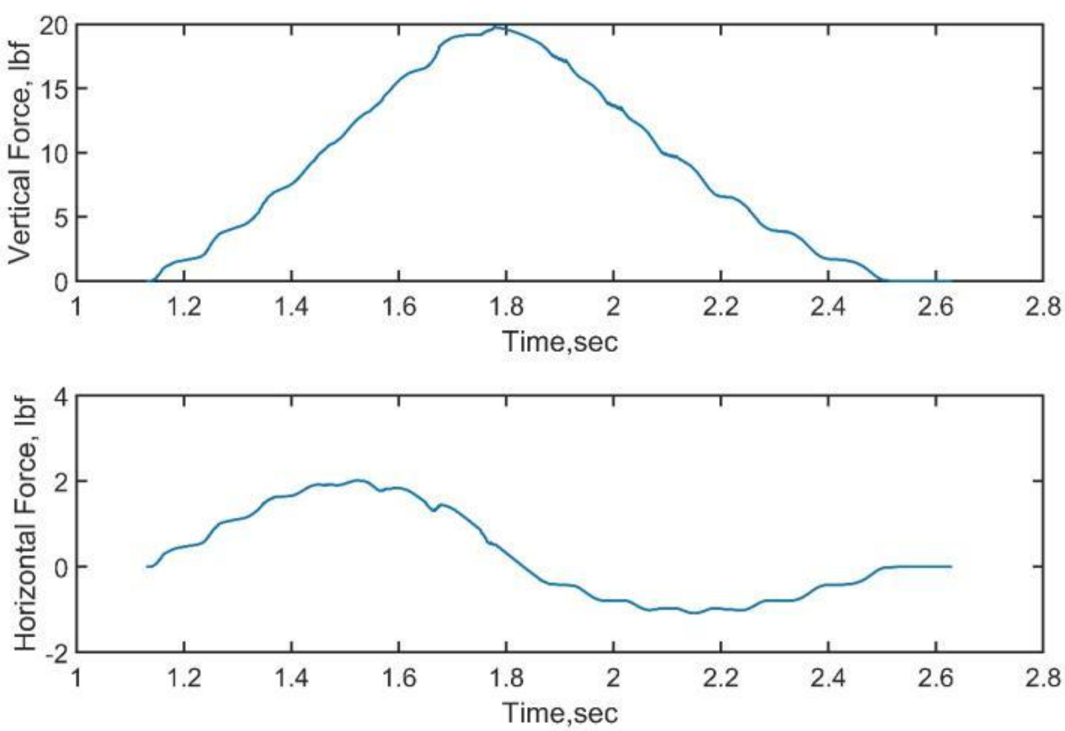

Figure C.2-10. Force Time-Histories for Bridge Configuration BSXX020

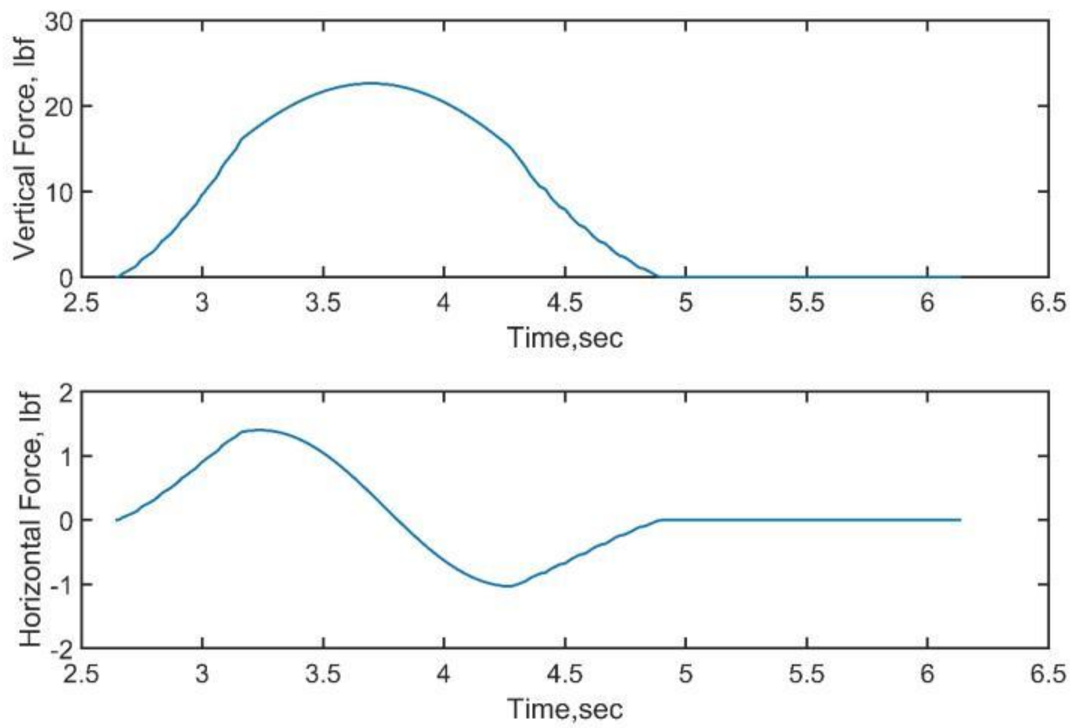

Figure C.2-11. Force Time-Histories for Bridge Configuration BSXX051

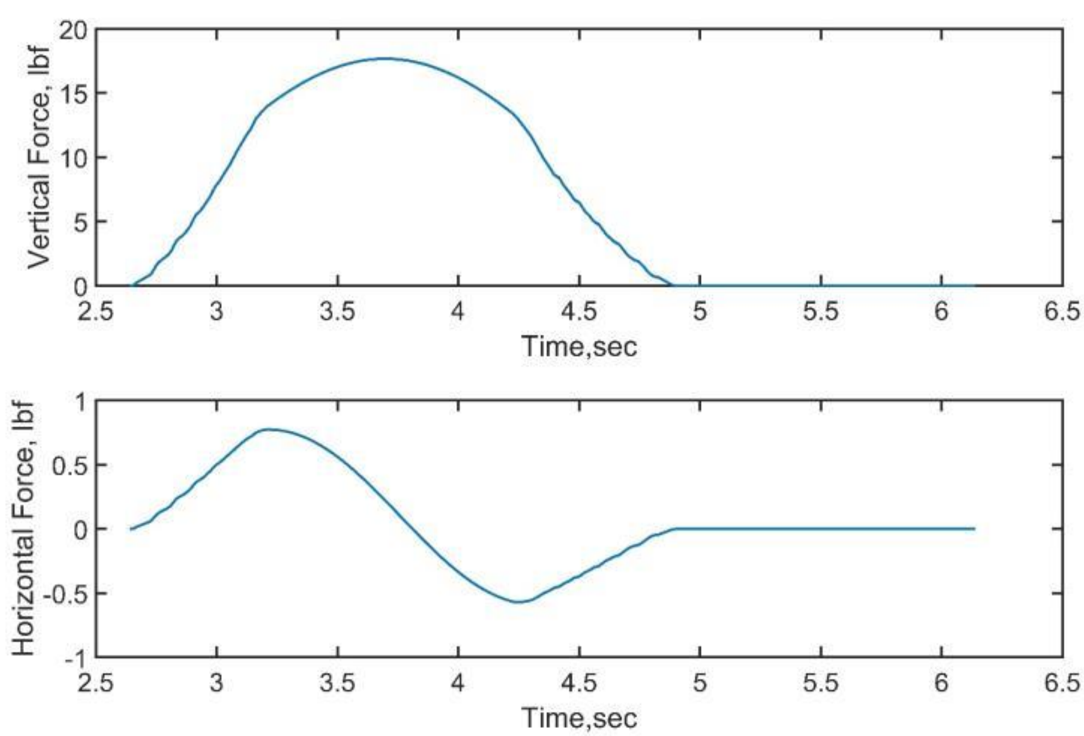

Figure C.2-12. Force Time-Histories for Bridge Configuration BSXX052

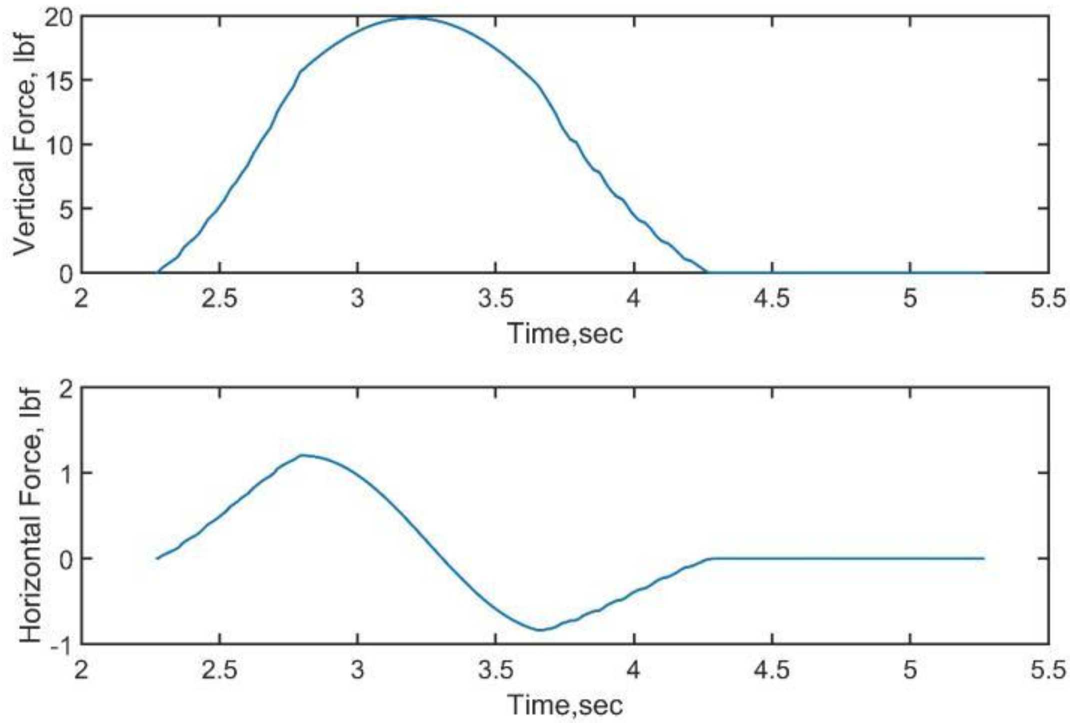

Figure C.2-13. Force Time-Histories for Bridge Configuration BSXX053

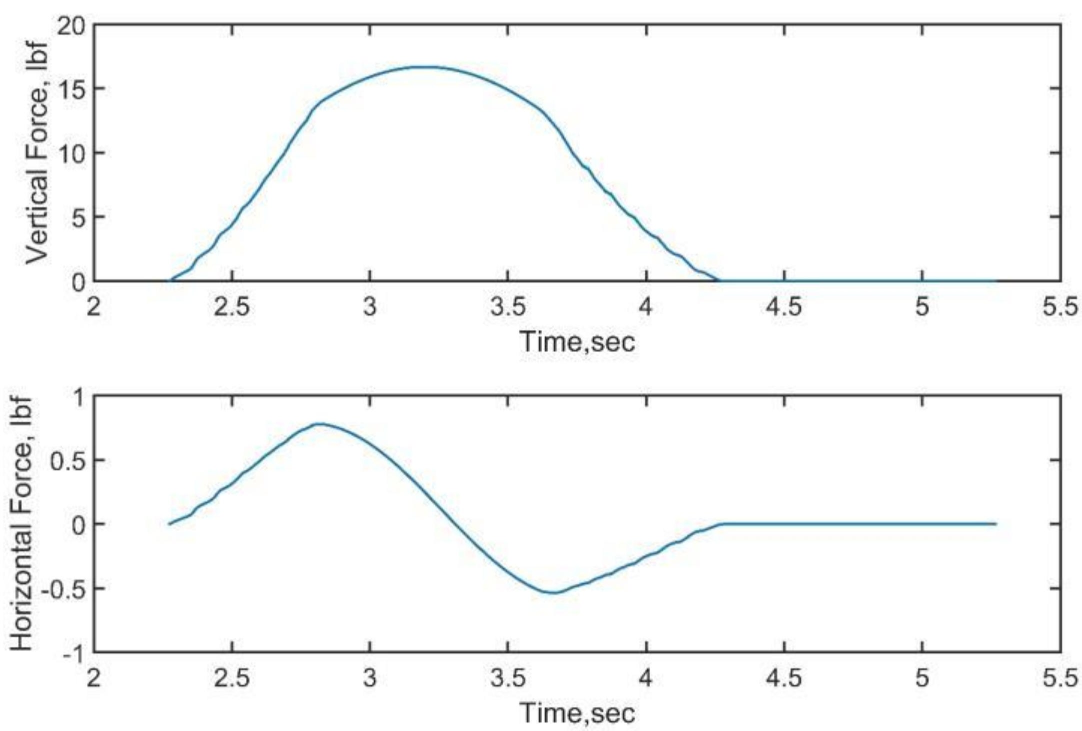

Figure C.2-14. Force Time-Histories for Bridge Configuration BSXX054

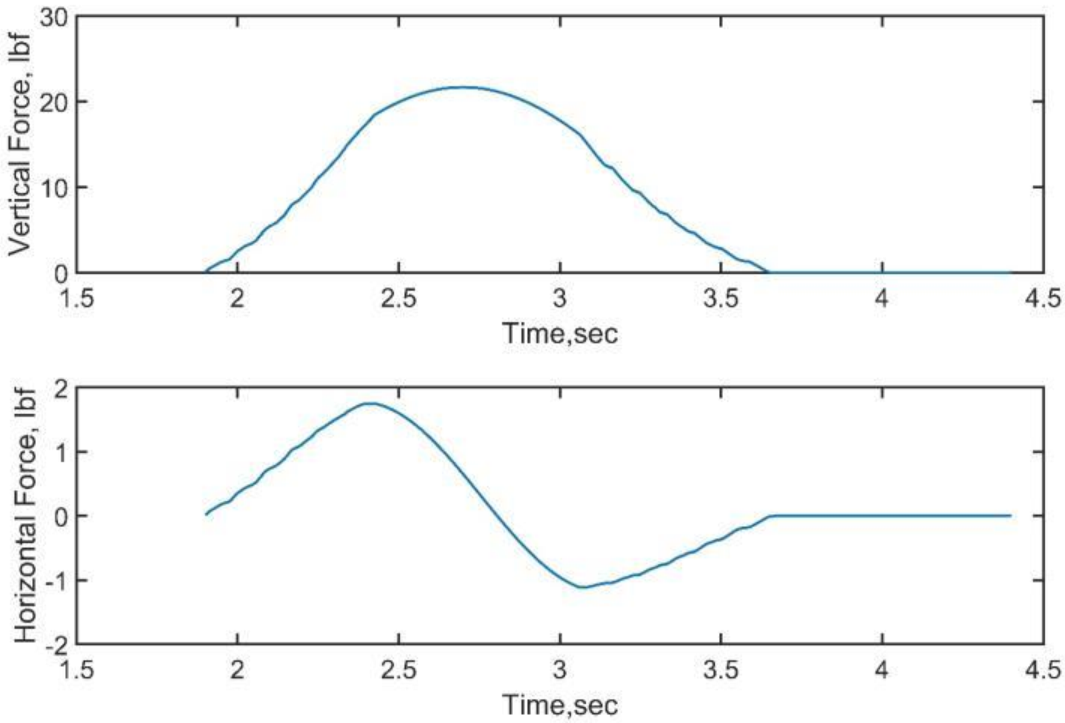

Figure C.2-15. Force Time-Histories for Bridge Configuration BSXX055

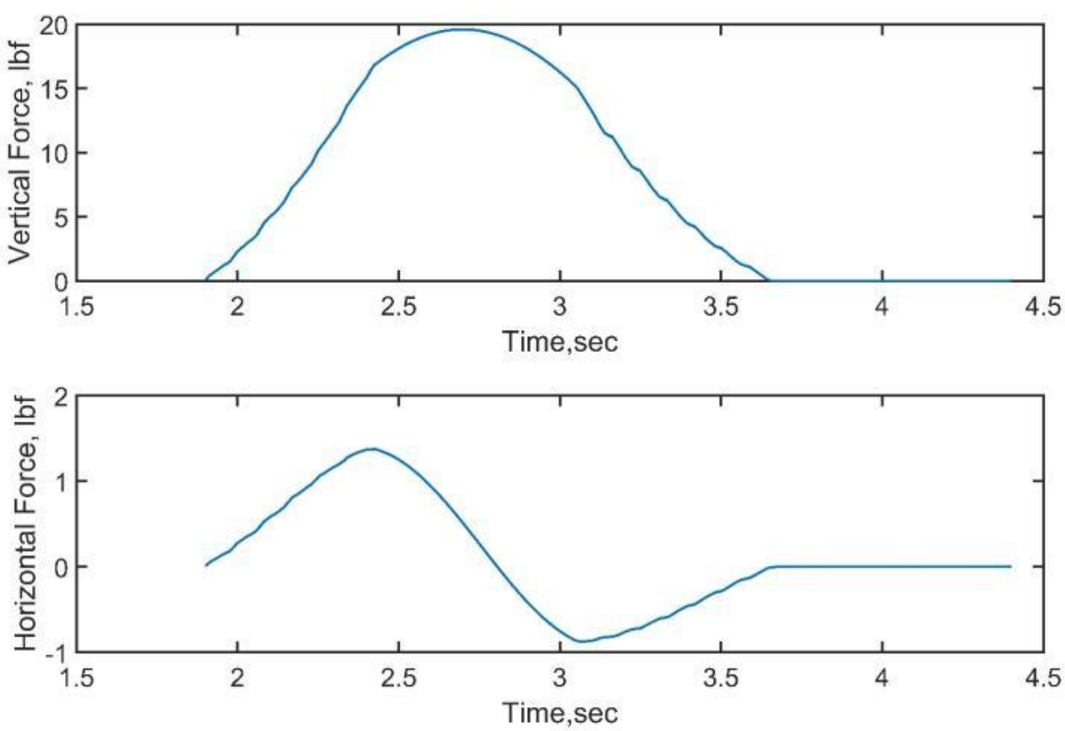

Figure C.2-16. Force Time-Histories for Bridge Configuration BSXX056

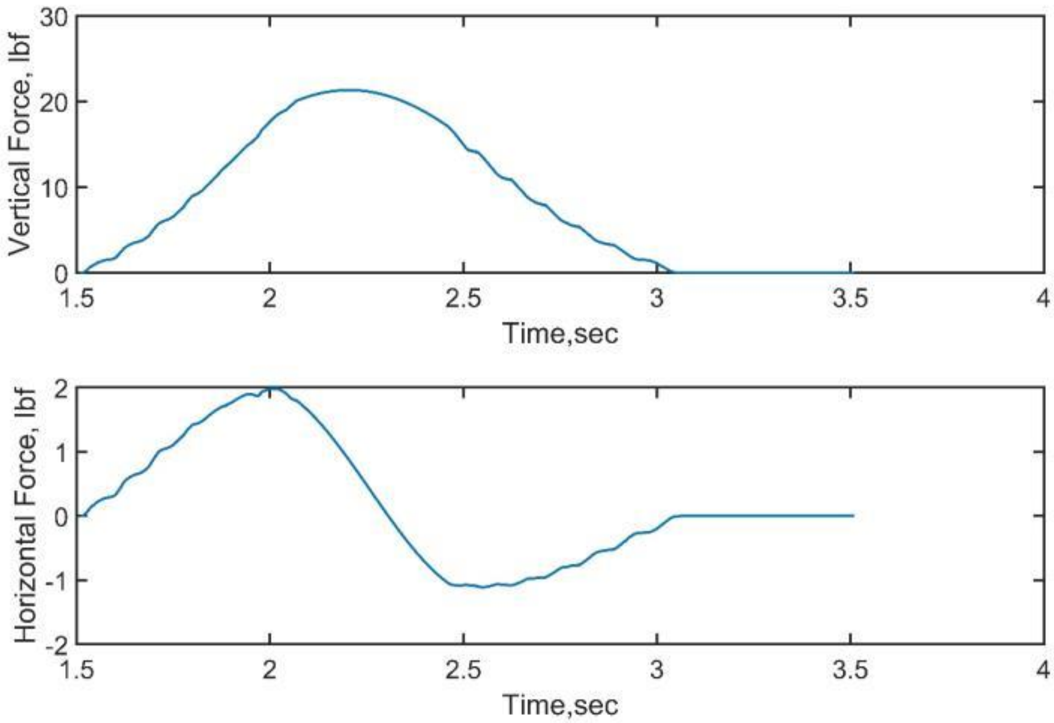

Figure C.2-17. Force Time-Histories for Bridge Configuration BSXX057

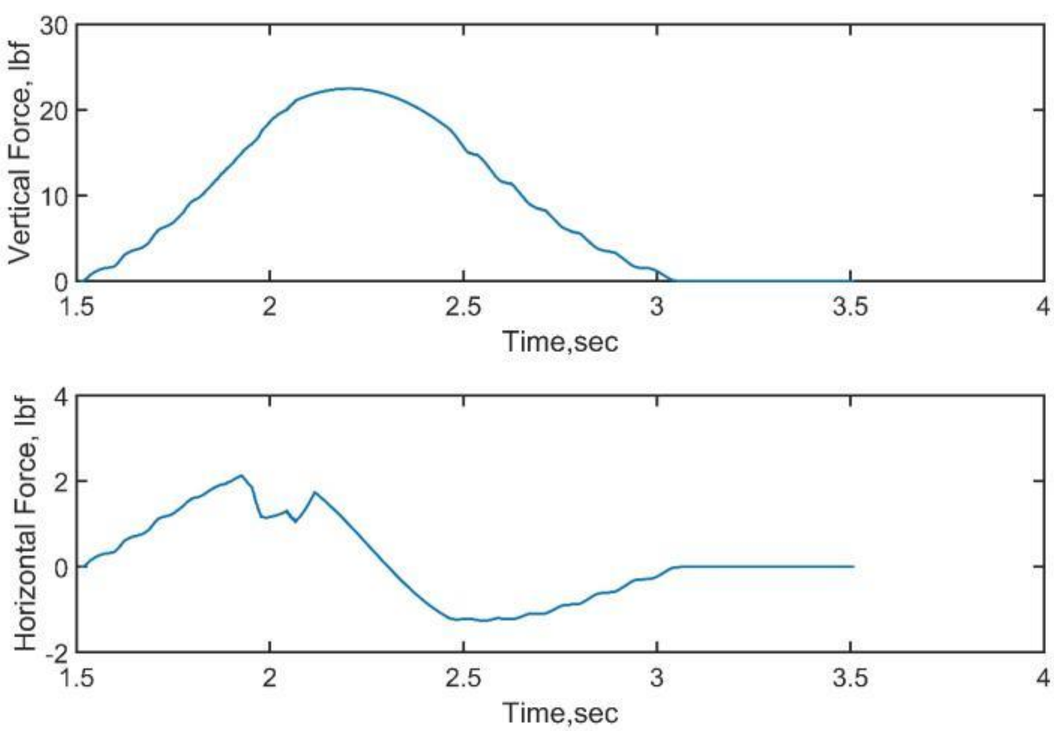

Figure C.2-18. Force Time-Histories for Bridge Configuration BSXX058

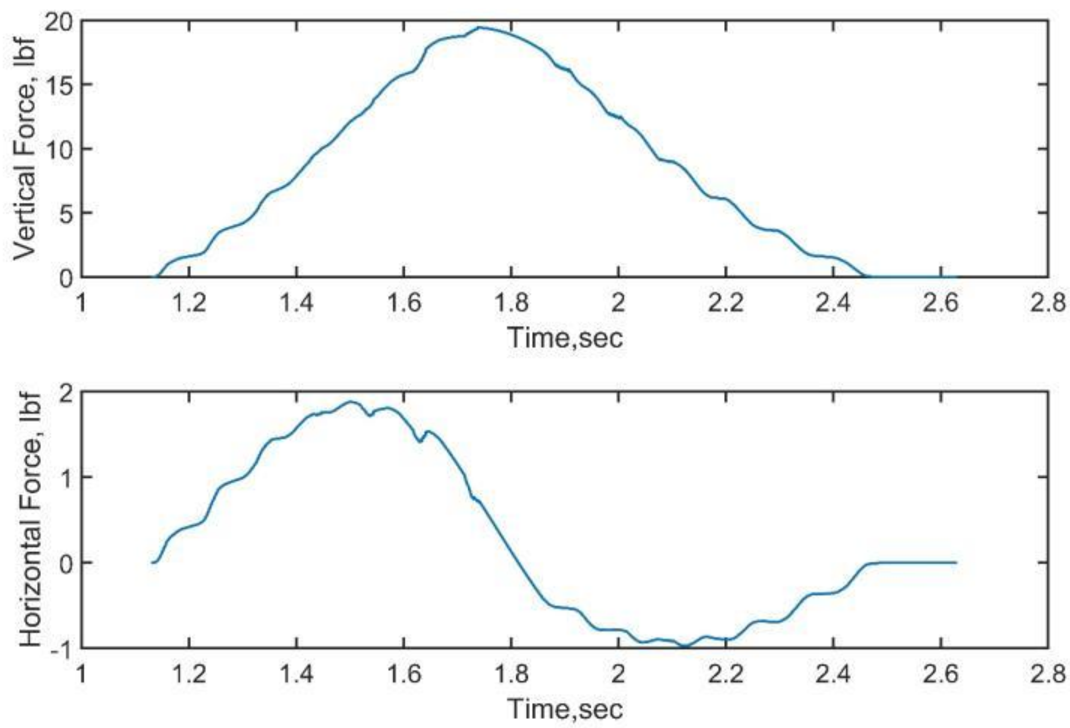

Figure C.2-19. Force Time-Histories for Bridge Configuration BSXX059

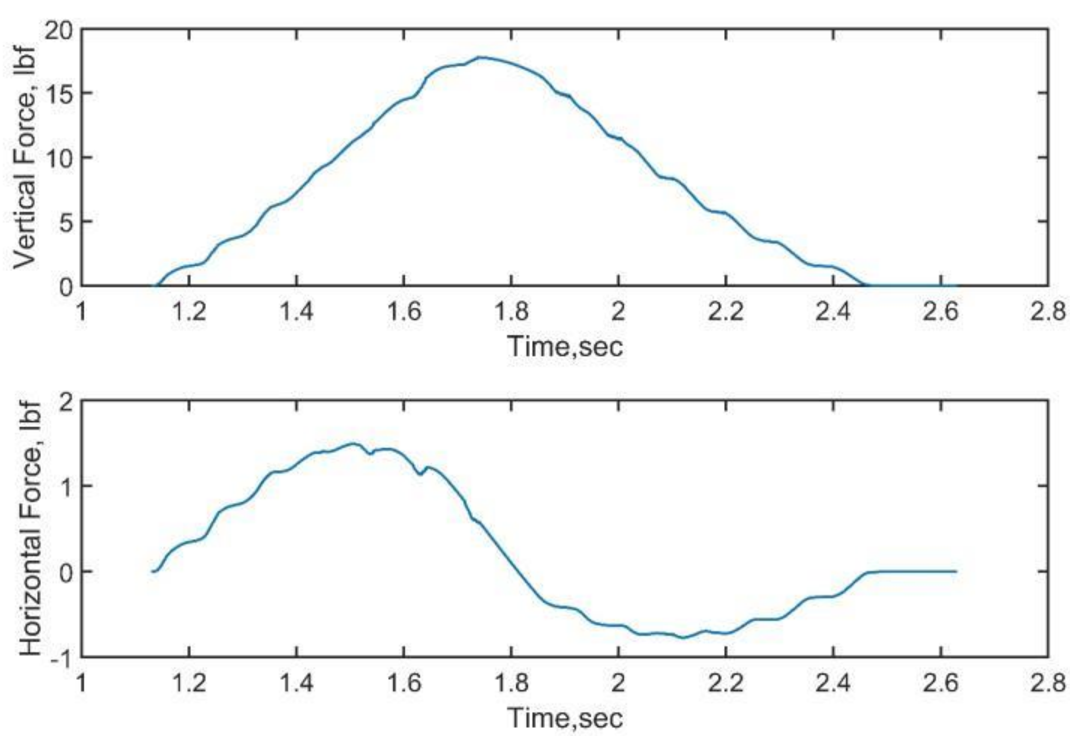

Figure C.2-20. Force Time-Histories for Bridge Configuration BSXX060

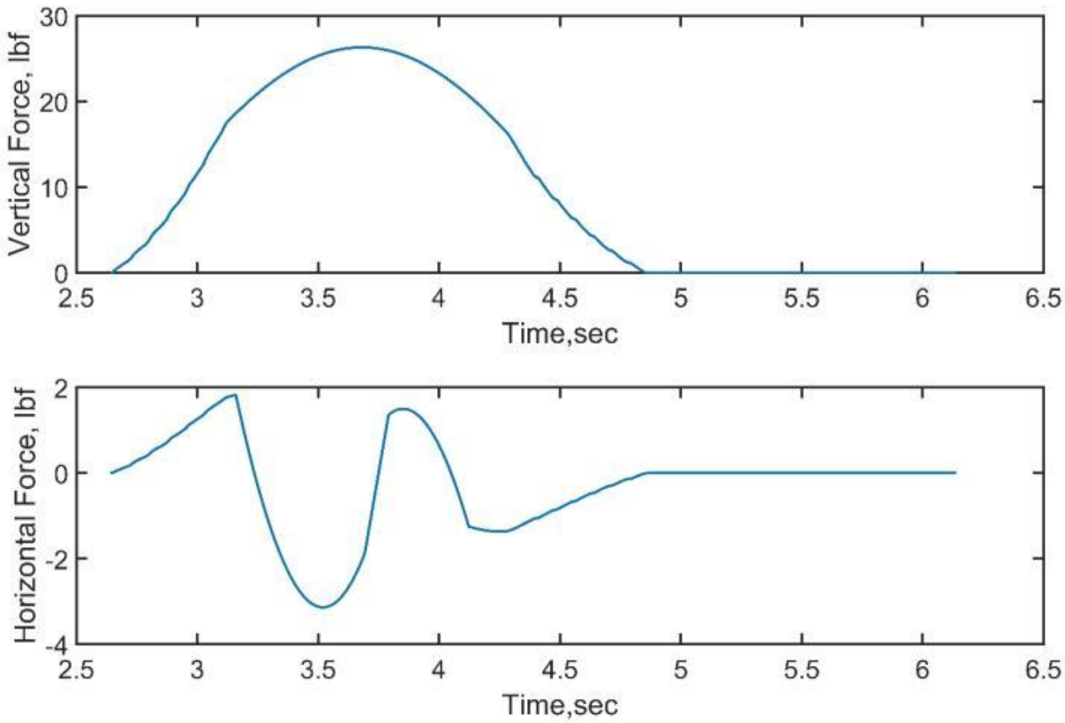

Figure C.2-21. Force Time-Histories for Bridge Configuration BSXX091

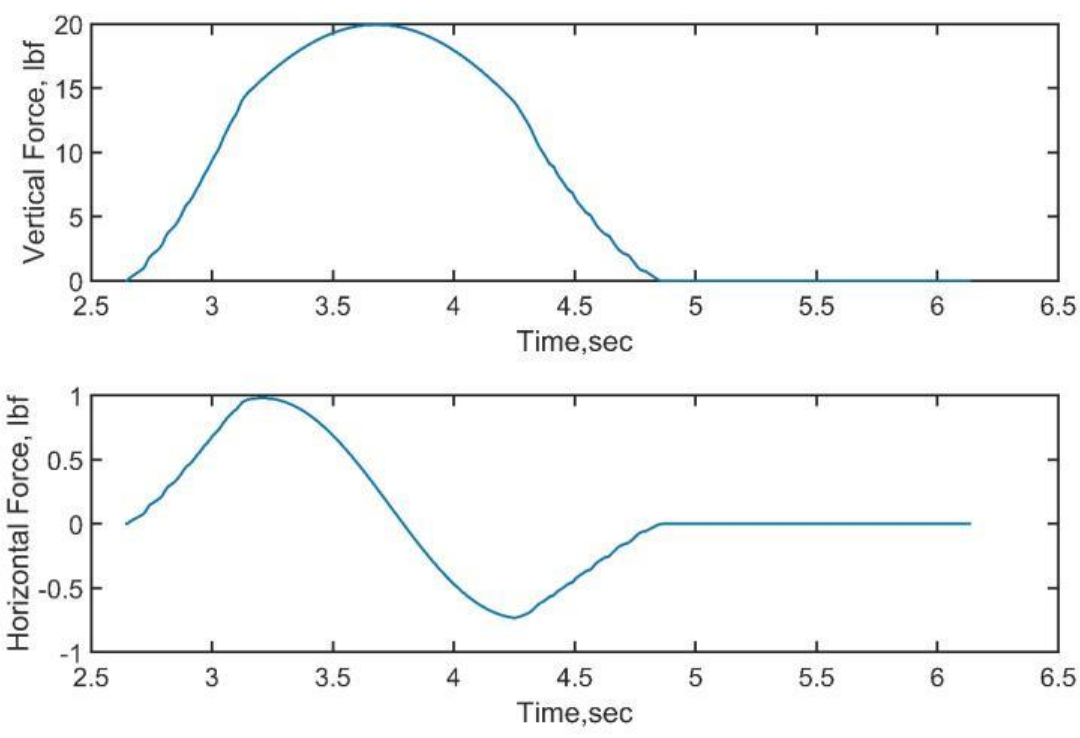

Figure C.2-22. Force Time-Histories for Bridge Configuration BSXX092

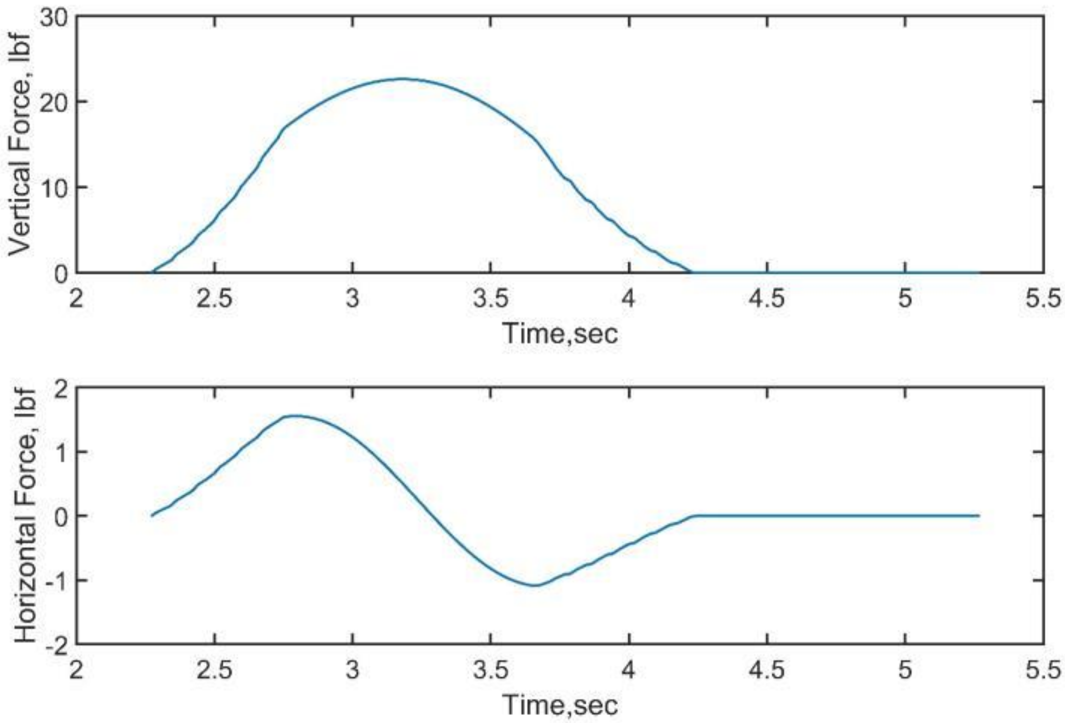

Figure C.2-23. Force Time-Histories for Bridge Configuration BSXX093

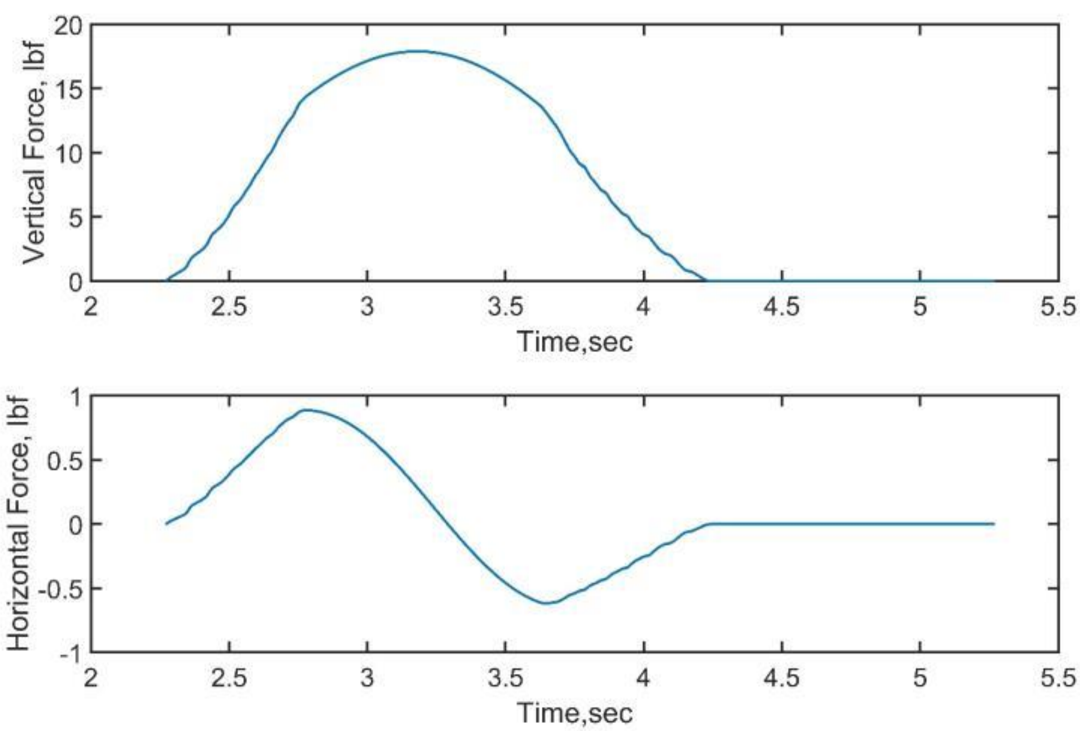

Figure C.2-24. Force Time-Histories for Bridge Configuration BSXX094

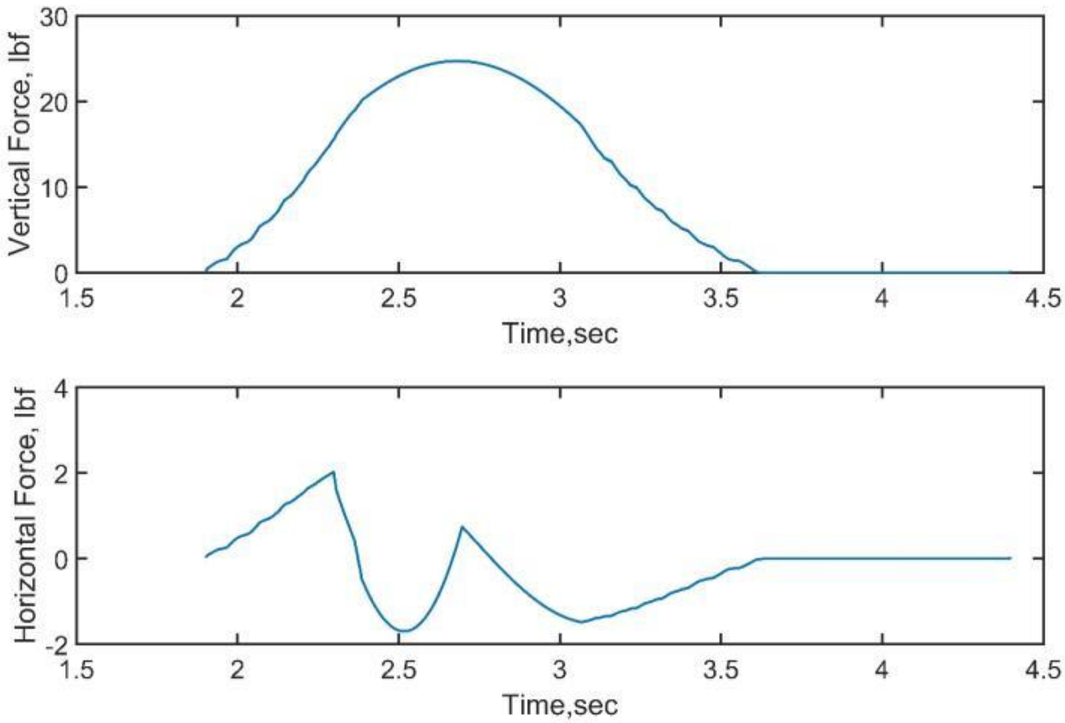

Figure C.2-25. Force Time-Histories for Bridge Configuration BSXX095

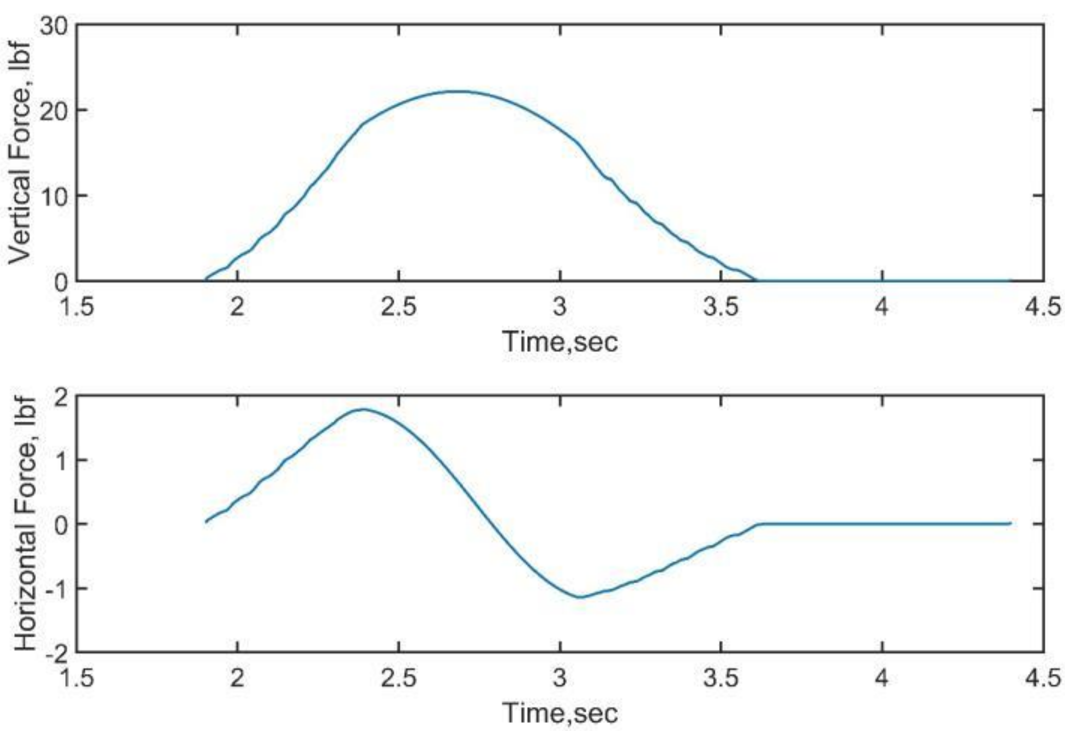

Figure C.2- 26. Force Time-Histories for Bridge Configuration BSXX096

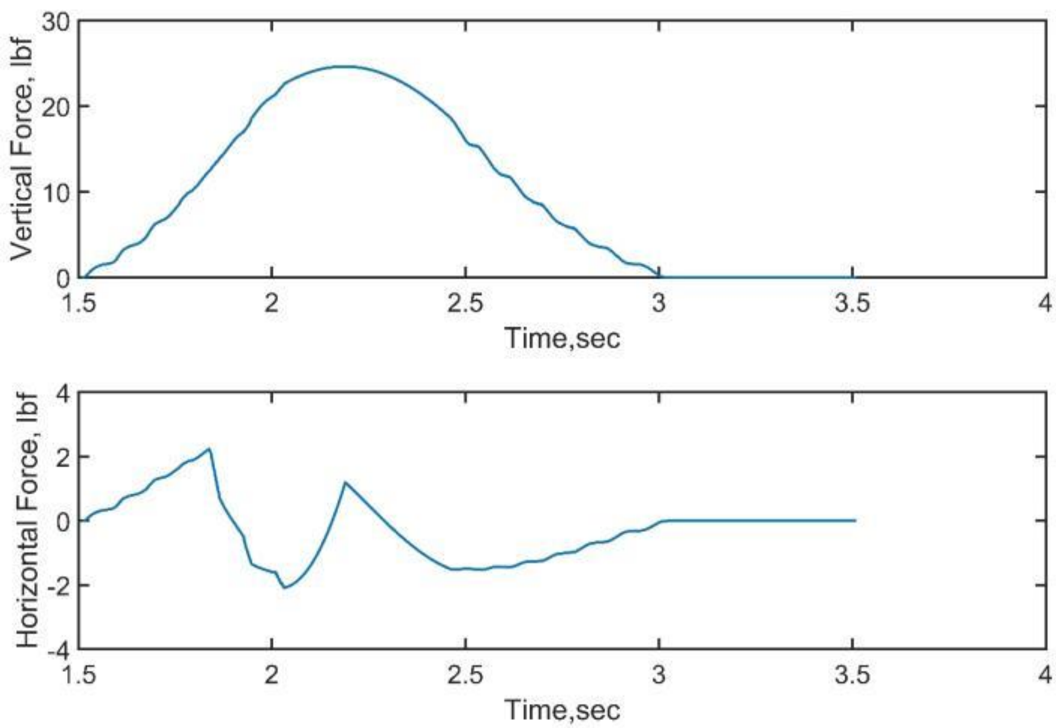

Figure C.2-27. Force Time-Histories for Bridge Configuration BSXX097

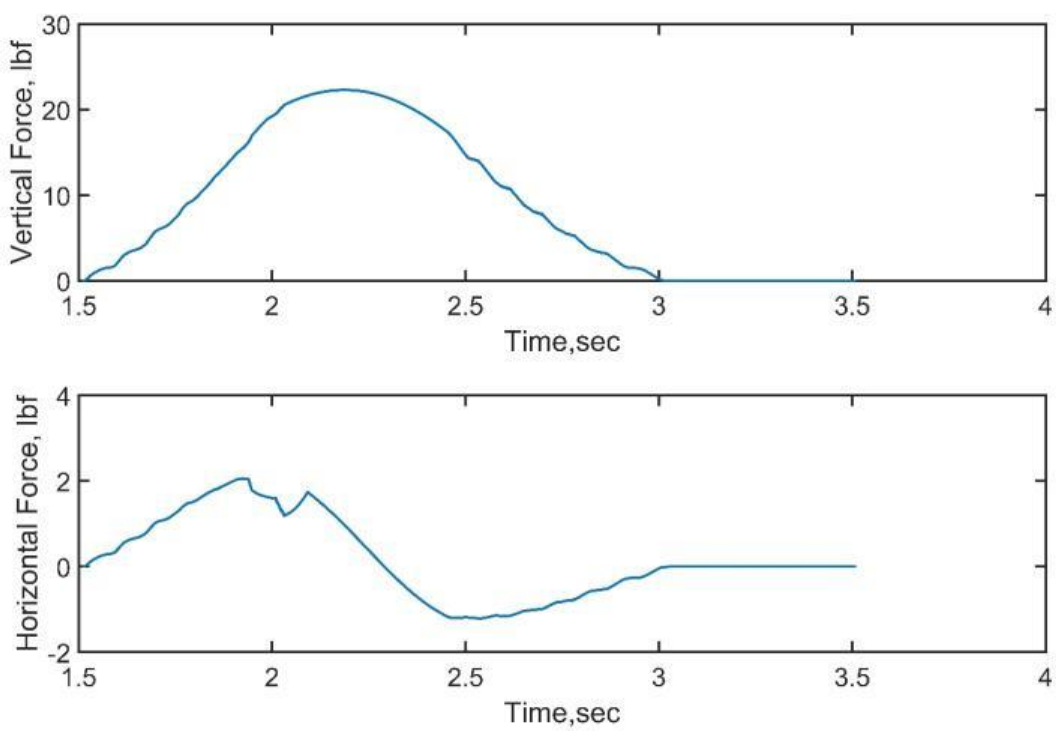

Figure C.2-28. Force Time-Histories for Bridge Configuration BSXX098

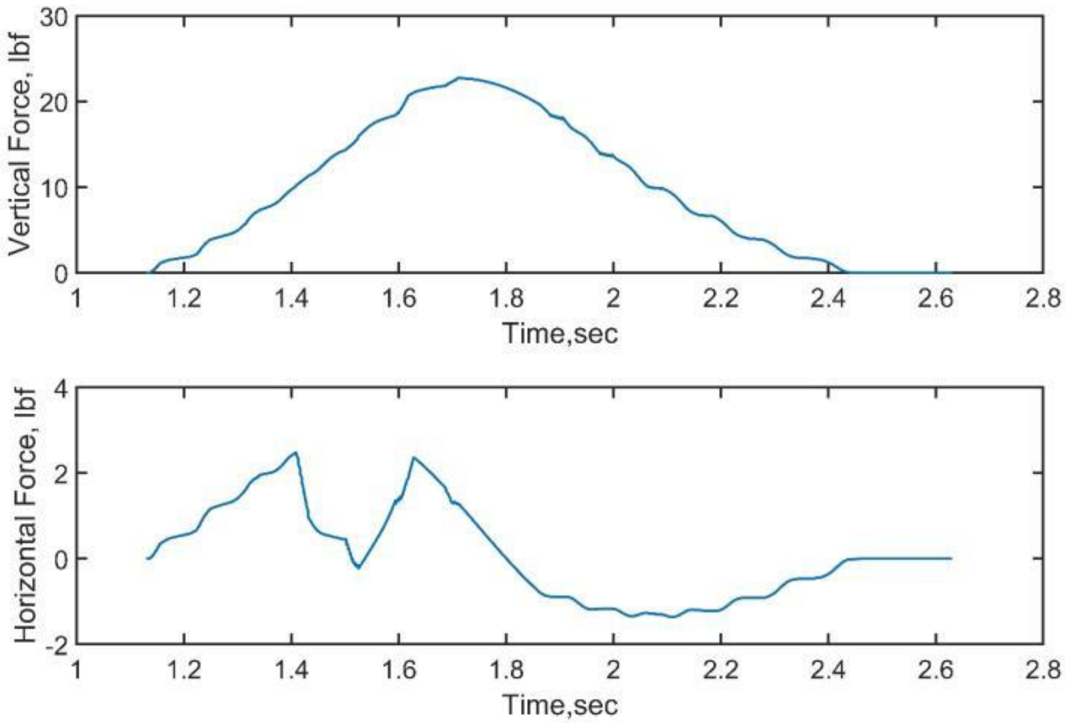

Figure C.2-29. Force Time-Histories for Bridge Configuration BSXX099

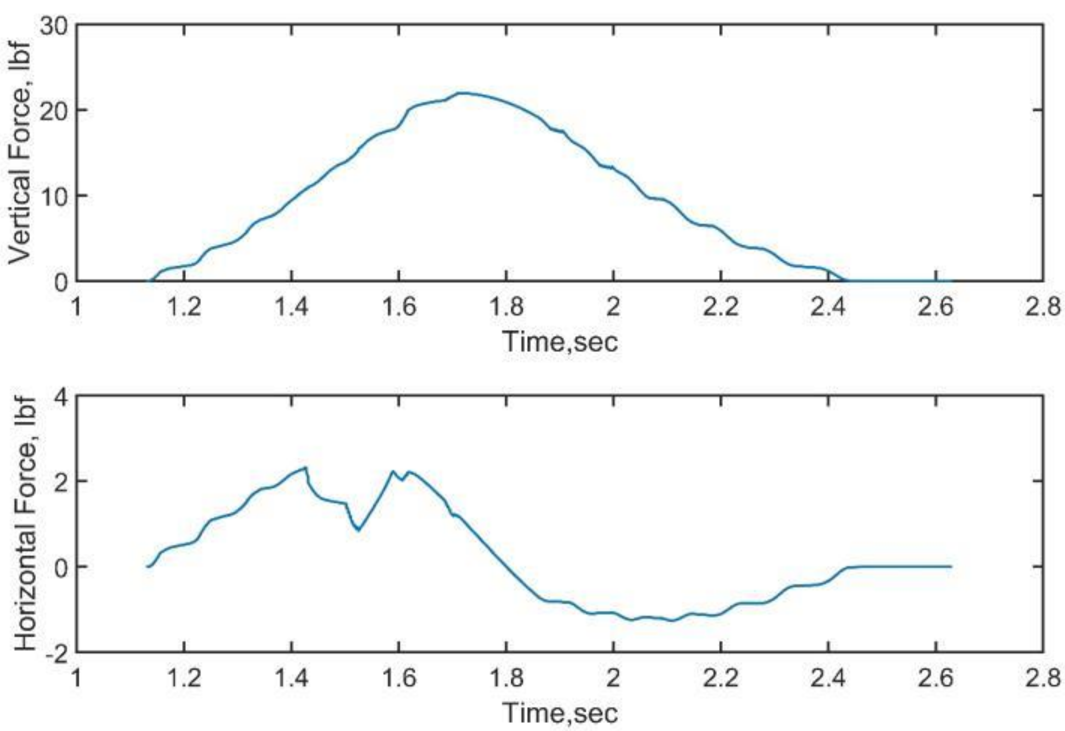

Figure C.2-30. Force Time-Histories for Bridge Configuration BSXX100

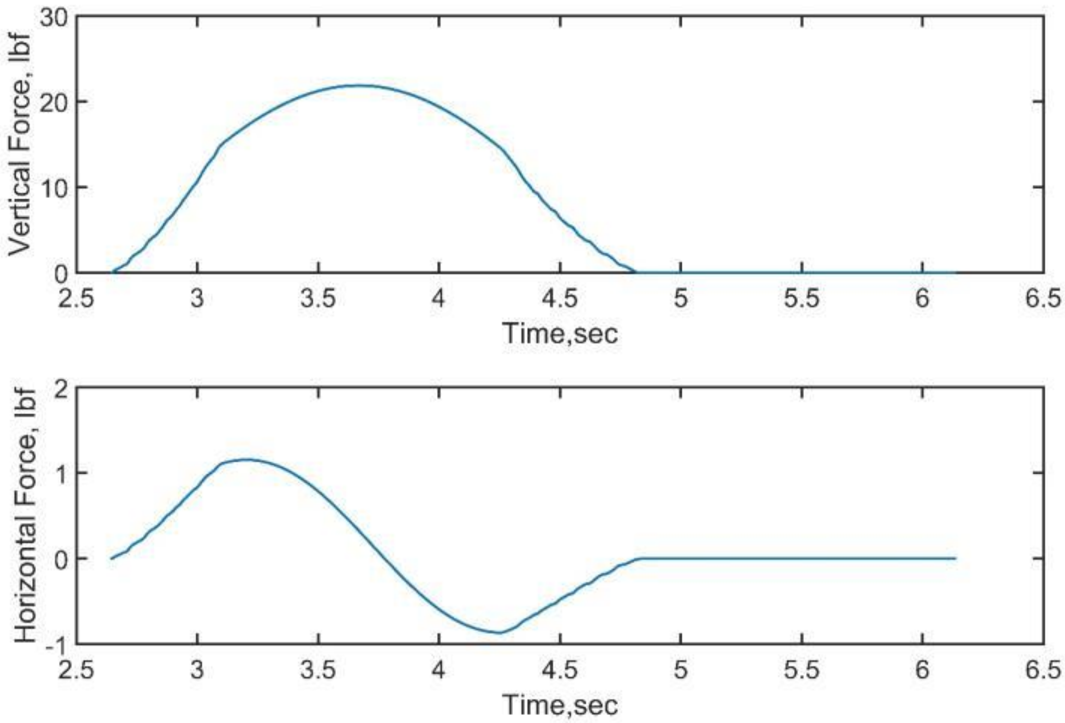

Figure C.2-31. Force Time-Histories for Bridge Configuration BSXX131

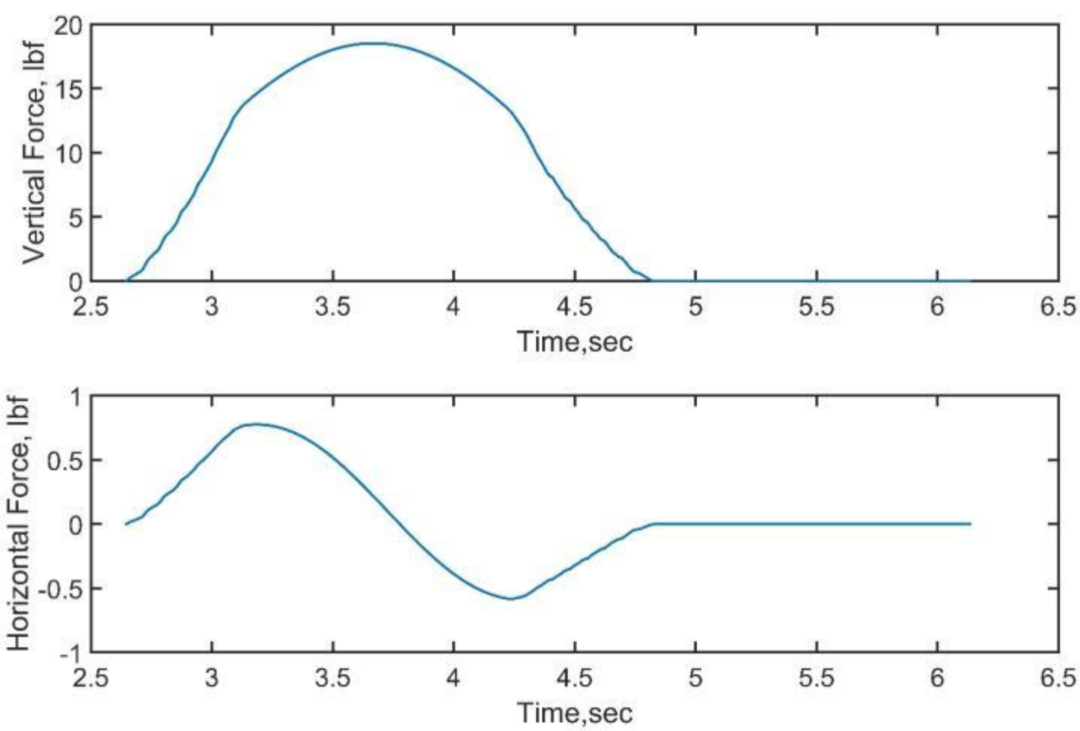

Figure C.2-32. Force Time-Histories for Bridge Configuration BSXX132

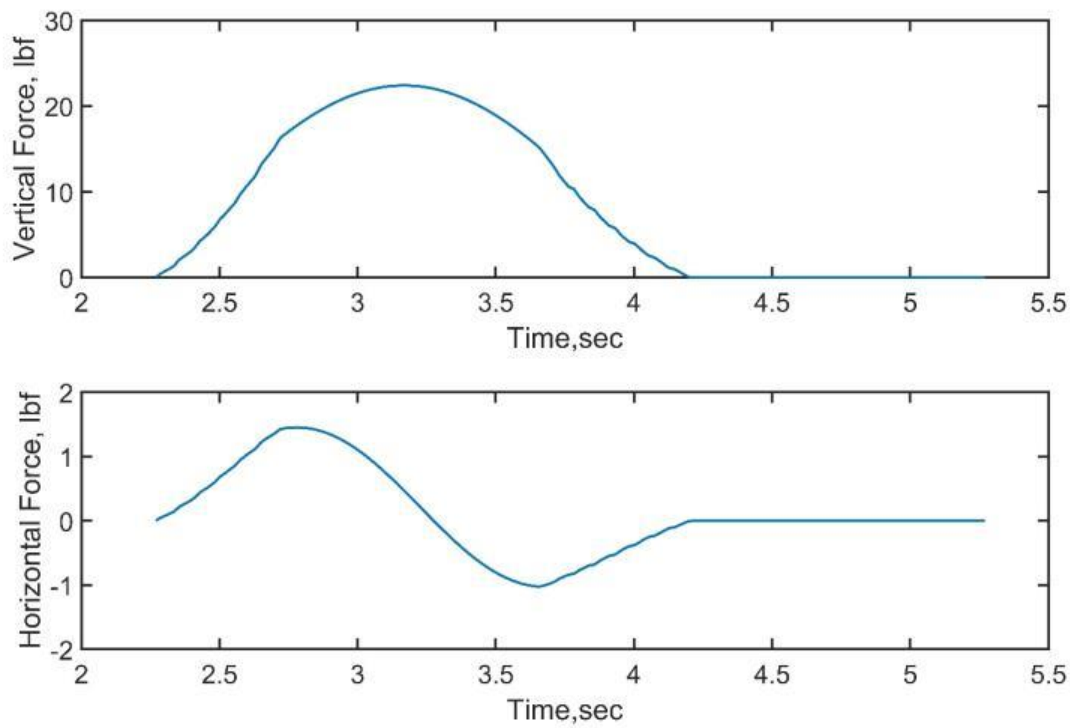

Figure C.2-33. Force Time-Histories for Bridge Configuration BSXX132

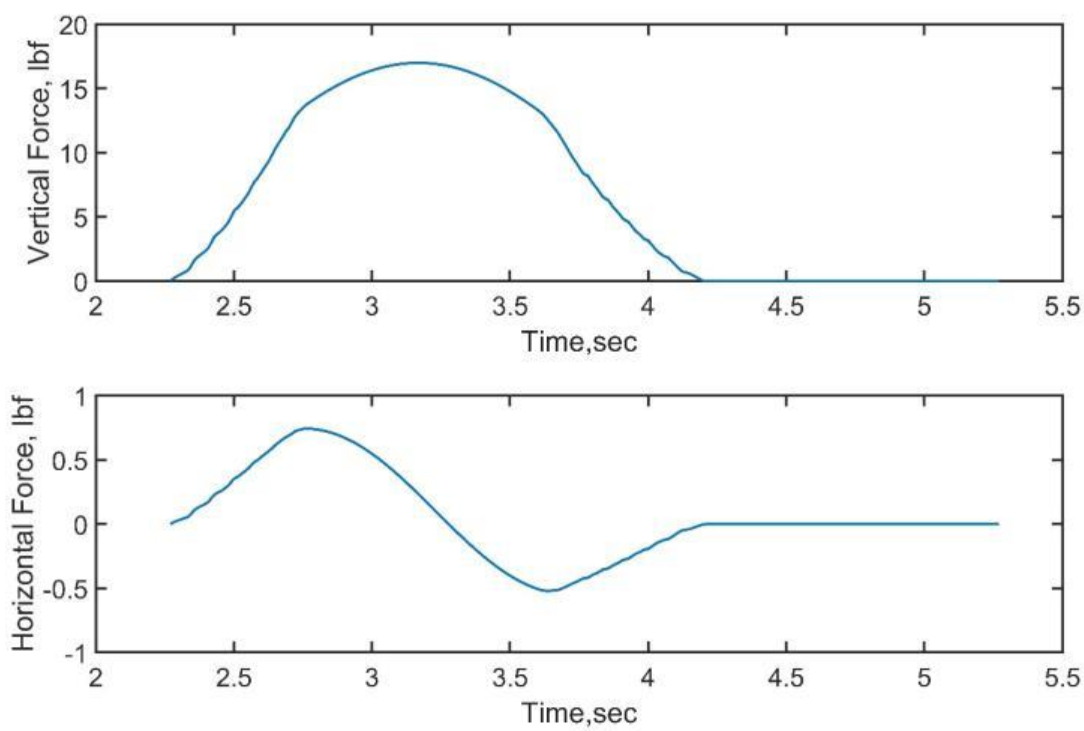

Figure C.2-34. Force Time-Histories for Bridge Configuration BSXX134

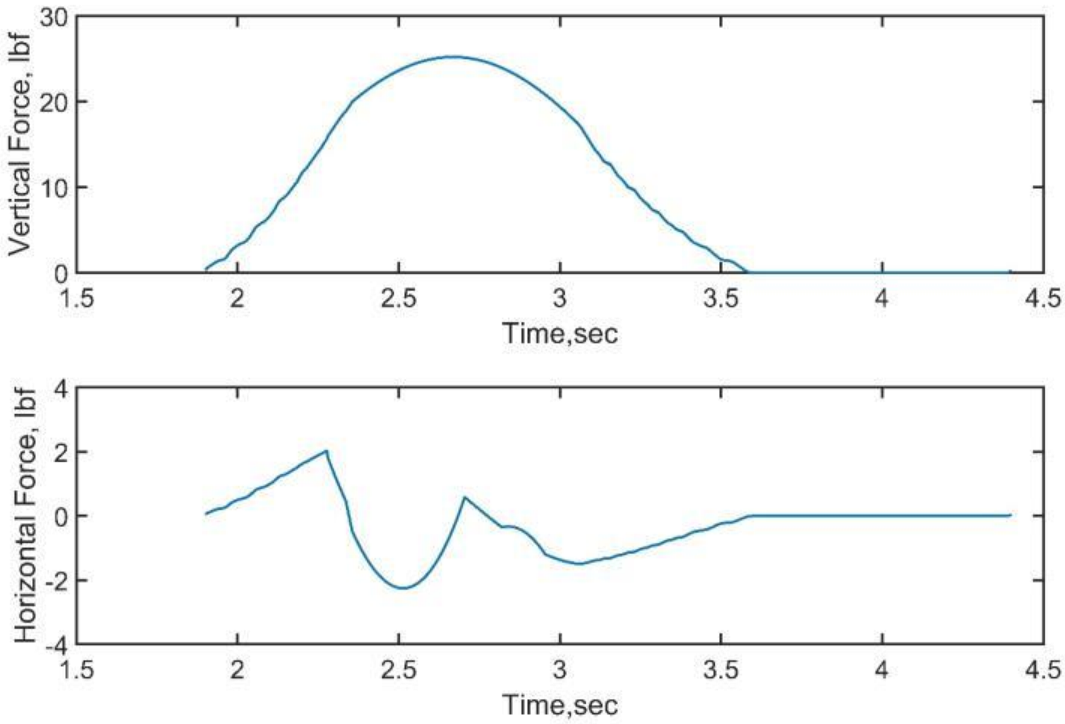

Figure C.2-35. Force Time-Histories for Bridge Configuration BSXX135

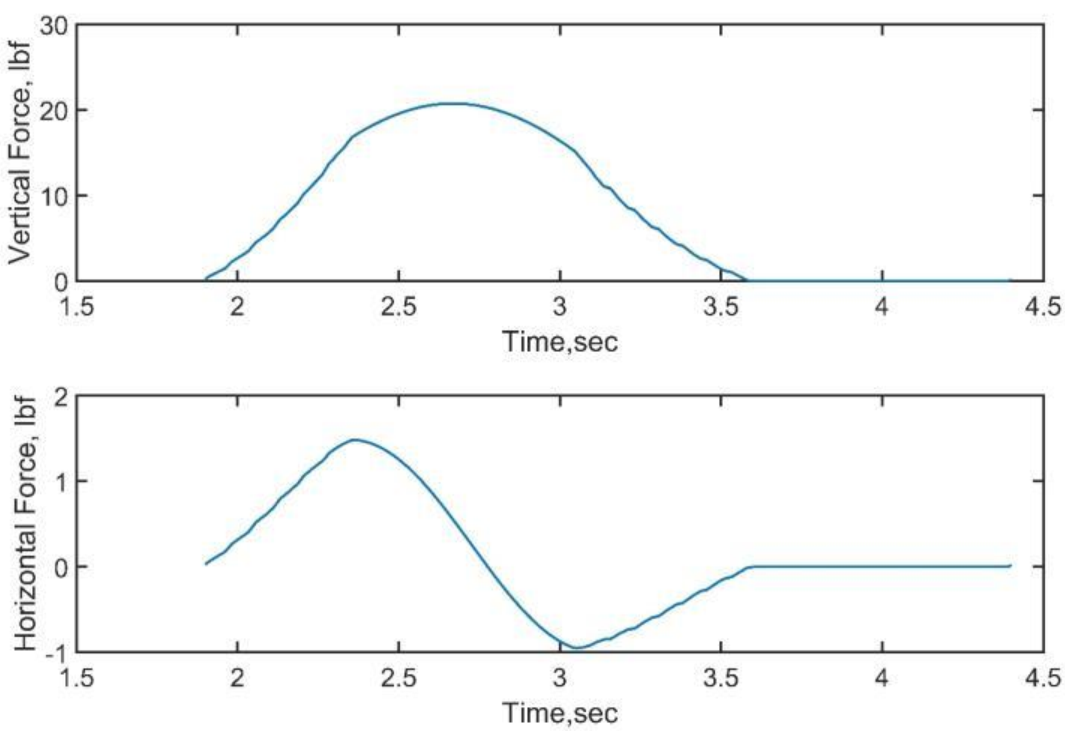

Figure C.2-36. Force Time-Histories for Bridge Configuration BSXX136

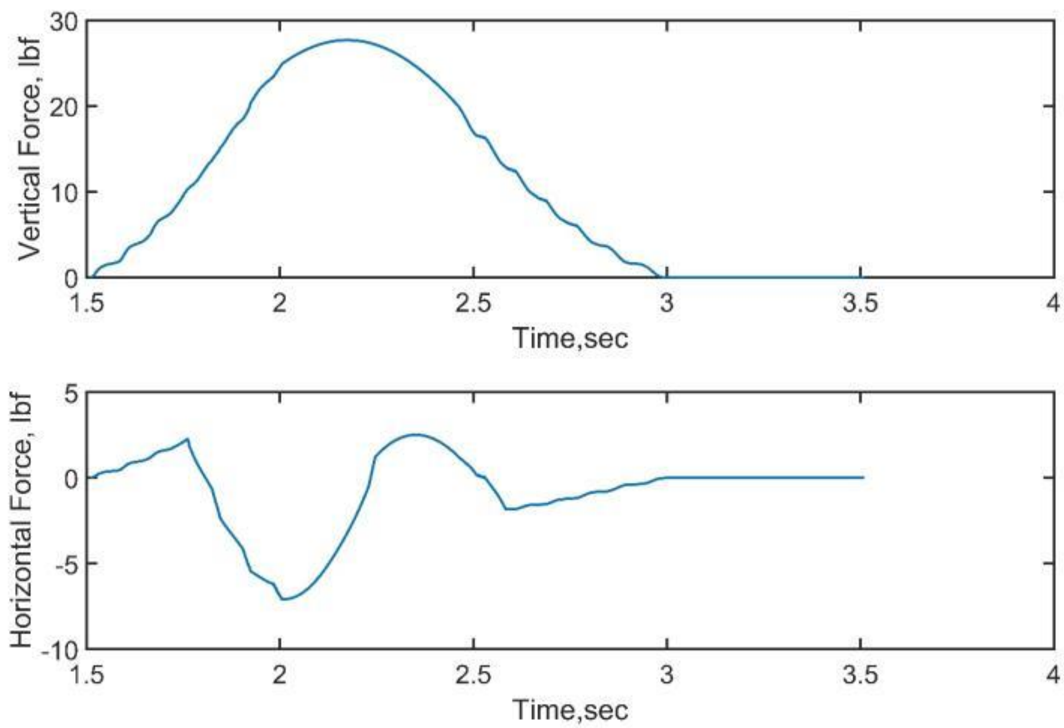

Figure C.2-37. Force Time-Histories for Bridge Configuration BSXX137

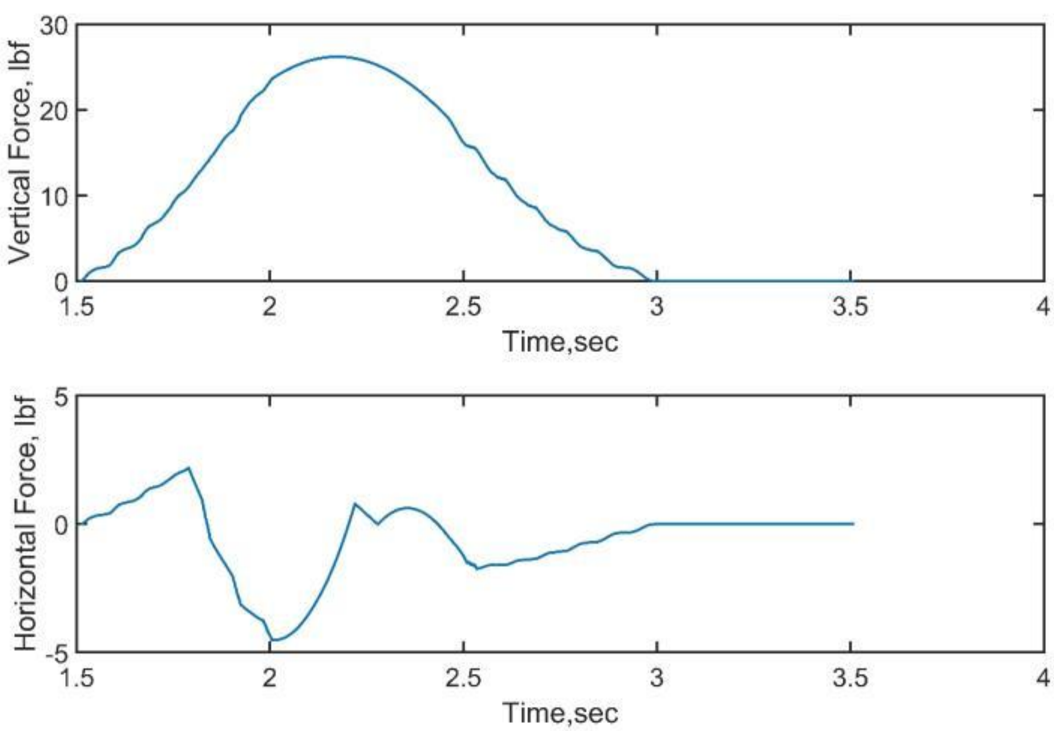

Figure C.2-38. Force Time-Histories for Bridge Configuration BSXX138

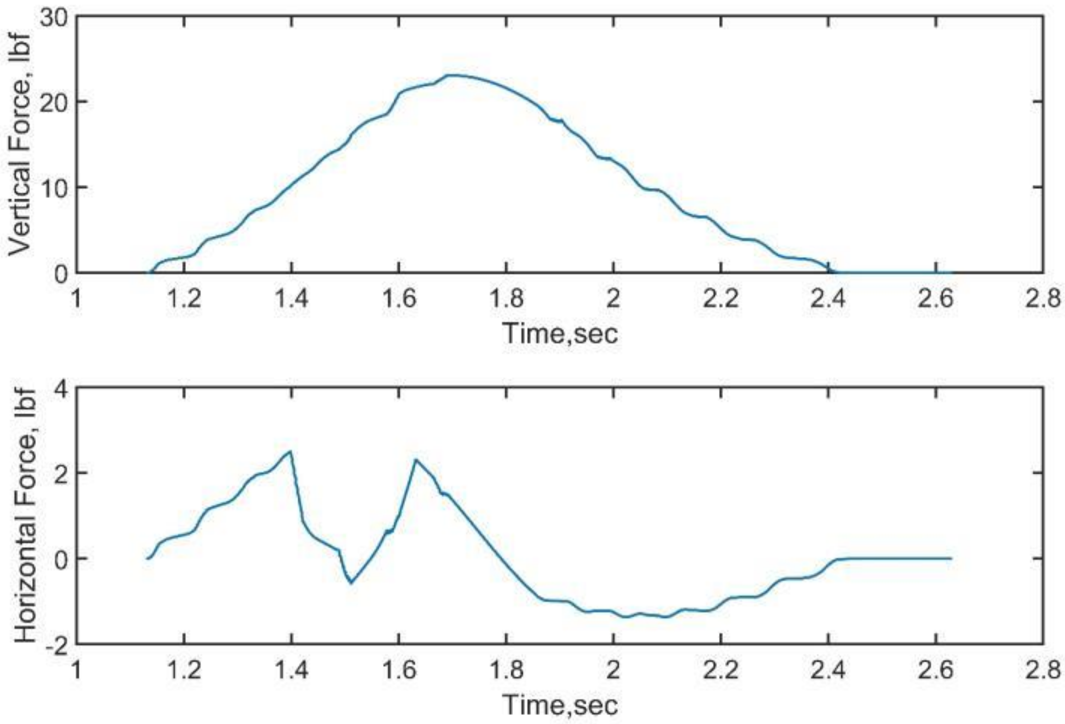

Figure C.2-39. Force Time-Histories for Bridge Configuration BSXX139

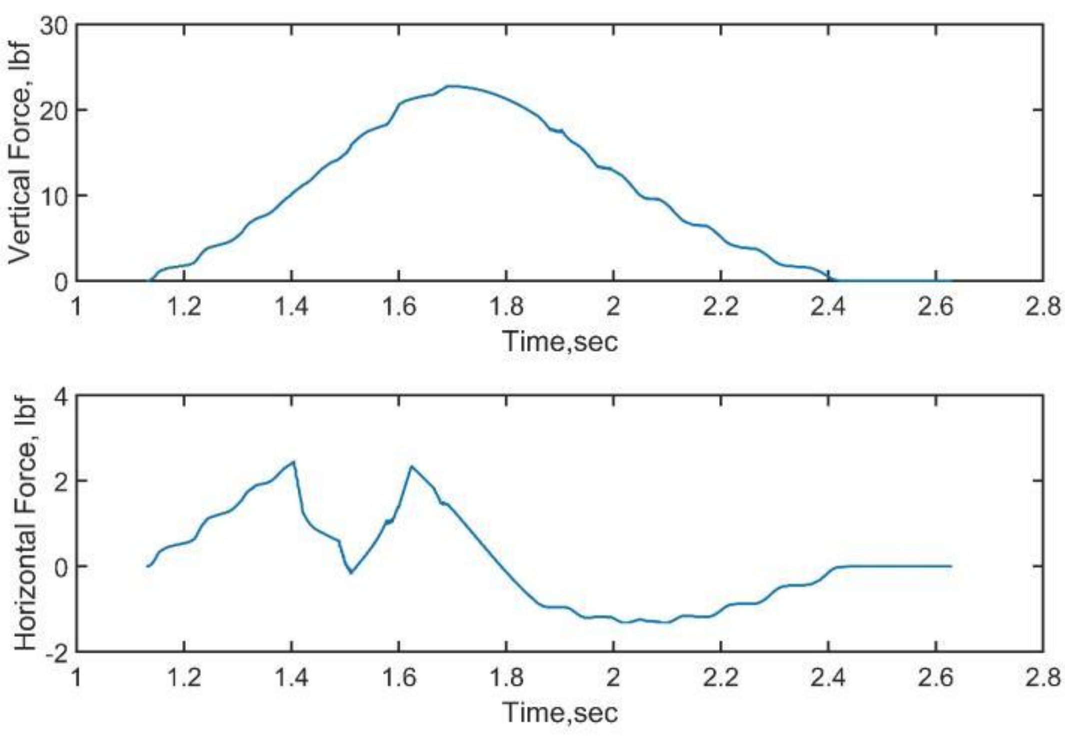

Figure C.2-40. Force Time-Histories for Bridge Configuration BSXX140

LIST OF REFERENCES

AASHTO, 2008. Guide specifications for bridges vulnerable to coastal storms. American Association of State Highway and Transportation Officials, Washington, DC.

Abrahamsen, B.C. and Faltinsen, O.M., 2011. The effect of air leakage and heat exchange on the decay of entrapped air pocket slamming oscillations. Physics of fluids, 23(10): 102107.

Araki, S. and Deguchi, I., 2015. Wave force acting on bridge with cross-section of concave shape. Frm Sea to Shore-Meeting the Challenges of the Sea: 1380-1389.

Azadbakht, M., 2013. Tsunami and hurricane wave loads on bridge superstructures. Ph.D. Thesis, Oregon State University.

Azadbakht, M. and Yim, S.C., 2015. Simulation and estimation of tsunami loads on bridge superstructures. Journal of Waterway, Port, Coastal, and Ocean Engineering, 141: 04014031.

Azadbakht, M. and Yim, S.C., 2016. Effect of trapped air on wave forces on coastal bridge superstructures. Journal of Ocean Engineering and Marine Energy, 2(2): 139-158.

Bagnold, R., 1939. Interim report on wave-pressure research.(includes plates and photographs). Journal of the Institution of Civil Engineers, 12(7): 202-226.

Bozorgnia, M., 2012. Computational fluid dynamic analysis of highway bridge superstructures exposed to hurricane waves. Ph.D. Thesis, University of Southern California.

Bozorgnia, M. and Lee, J.-J., 2012. Computational fluid dynamic analysis of highway bridges exposed to hurricane waves. Coastal Engineering Proceedings, p.^pp. 70.

Bozorgnia, M., Lee, J.-J. and Raichlen, F., 2010. Wave structure interaction: Role of entrapped air on wave impact and uplift forces. Coastal Engineering, 1: 1-12.

Bradner, C., 2009. Large-scale laboratory observations of wave forces on a highway bridge

superstructure. Master Thesis, Oregon State University.

Bradner, C., Schumacher, T., Cox, D. and Higgins, C., 2011. Large–scale laboratory observations of wave forces on a highway bridge superstructure, Oregon Transportation Research and Education Consortium (OTREC), Portland, OR.

Canale, R.P. and Chapra, S.C., 1991. Numerical methods for engineers. Mathematics and Computers in Simulation, 33: 260.

CD-adapco, 2017. User guide star-ccm+ version 12.02. CD-adapco, Melville, NY.

Crowley, R., Robeck, C. and Dompe, P., 2018. A three-dimensional computational analysis of bridges subjected to monochromatic wave attack. Journal of Fluids and Structures, 79: 76-93.

Cuomo, G., Shimosako, K.i. and Takahashi, S., 2009. Wave-in-deck loads on coastal bridges and the role of air. Coastal Engineering, 56: 793-809.

Dean, R.G. and Dalrymple, R.A., 1999. Water wave mechanics for engineers and scientists. Engineering Structures, 7: 511.

Douglass, S.L., Chen, Q., Olsen, J.M., Edge, B.L. and Brown, D., 2006. Wave forces on bridge decks, U.S. Department of Transportation, Washington, DC.

Douglass, S.L., Webb, B.M. and Kilgore, R., 2014. Hydraulic engineering circular no. 25 (volume 2) highways in the coastal environment: Assessing extreme events. In: F.H.A. Office of Bridge Technology (Editor), Washington, DC.

Esteban, M.D. et al., 2015. Offshore wind foundation design: Some key issues. Journal of Energy Resources Technology, 137(5): 051211.

Fluent, A., 2009. 12.0 user's guide. Ansys Inc.

Greenshields, C.J., 2015. Openfoam user guide. OpenFOAM Foundation Ltd, version, 3(1).

Jin, J. and Meng, B., 2011. Computation of wave loads on the superstructures of coastal highway bridges. Ocean Engineering, 38: 2185-2200.

Kaplan, P., 1992. Wave impact forces on offshore structures: Re-examination and new interpretations. Offshore Technology Conference, p.^pp.

Kaplan, P., Murray, J. and Yu, W., 1995. Theoretical analysis of wave impact forces on platform deck structures, American Society of Mechanical Engineers, New York, NY (United States).

Marin, J. and Sheppard, D.M., 2009. Storm surge and wave loading on bridge superstructures. Structures Congress 2009: Don't Mess with Structural Engineers: Expanding Our Role, p.^pp. 557-566.

Marin, J.M., 2010. Wave loading on bridge superstructures. Ph.D. Thesis, University of Florida, Florida.

McConnell, K., Allsop, W. and Cruickshank, I., 2004. Piers, jetties and related structures exposed to waves: Guidelines for hydraulic loadings. Thomas Telford.

Meng, B., 2008. Calculation of extreme wave loads on coastal highway bridges. Ph.D. Thesis, Texas A&M University, Texas.

Mitsuyasu, H., 1966. Shock pressure of breaking waves. Coastal Engineering, 10: 268-283.

Morison, J., Johnson, J. and Schaaf, S., 1950. The force exerted by surface waves on piles. Journal of Petroleum Technology, 2(05): 149-154.

Padgett, J. et al., 2008. Bridge damage and repair costs from hurricane katrina. Journal of Bridge Engineering, 13(1): 6-14.

Panchang, V., Cushman-Roisin, B. and Pearce, B., 1988. Combined refraction-diffraction of short-waves in large coastal regions. Coastal Engineering, 12(2): 133-156.

Sawaragi, T., 1995. Coastal engineering- waves, beaches, wave-structure interactions. 143-144.

Seiffert, B.R., Cengiz Ertekin, R. and Robertson, I.N., 2016. Effect of entrapped air on solitary wave forces on a coastal bridge deck with girders. Journal of Bridge Engineering, 21(2): 04015036.

Seiffert, B.R., Ertekin, R.C. and Robertson, I.N., 2015. Wave loads on a coastal bridge deck and the role of entrapped air. Applied Ocean Research, 53: 91-106.

Sirovich, A.J.E.M.L., Holmes, H.P., Keller, J.K.J., Mielke, B.J.M.A. and Sreenivasan, C.S.P.K.R.S., 1996. Prandtl's essentials of fluid mechanics. Applied Mathematical Sciences, 115: 80.

Takahashi, S., Tanimoto, K. and Miyanaga, S., 1985. Uplift wave forces due to compression of enclosed air layer and their similtude law. Coastal Engineering, 28.

Talbot, J., 2005. Repairing Florida's escambia bay bridge. Associated Construction Publications available online at/http://www. acppubs. com/article/CA511040. html S.

Xu, G. and Cai, C., 2014. Wave forces on biloxi bay bridge decks with inclinations under solitary waves. Journal of Performance of Constructed Facilities, 29(6): 04014150.